UC Santa Barbara

UC Santa Barbara Electronic Theses and Dissertations

Title

Convection Affects Magnetic Turbulence in White Dwarf Accretion Disks

Permalink

https://escholarship.org/uc/item/5fk2m1jv

Author

Coleman, Matthew Singh Bawa

Publication Date

2017

Peer reviewed|Thesis/dissertation

eScholarship.org Powered by the California Digital Library
University of California

UNIVERSITY of CALIFORNIA
Santa Barbara

Convection Affects Magnetic Turbulence in White Dwarf Accretion Disks

A dissertation submitted in partial satisfaction of the
requirements for the degree of

Doctor of Philosophy

in

Physics

by

Matthew S. B. Coleman

Committee in charge:

Professor Omer Blaes, Chair

Professor Benjamin Mazin

Professor Lars Bildsten

June 2017

The dissertation of Matthew S. B. Coleman is approved:

Professor Lars Bildsten

Professor Benjamin Mazin

Professor Omer Blaes, Chair

June 2017

Copyright © 2017
by Matthew S. B. Coleman

This dissertation is dedicated to

my wife who willingly married a physics Ph.D. student and was nevertheless, loving, supportive and caring without hesitation,

and

to my mother who supported my desire to be an astrophysicist since I was nine years old.

Acknowledgements

First and foremost I must acknowledge the critical role of my advisor, Professor Omer Blaes, for guiding me through this research. Second, I must thank Shigenobu Hirose who ran most of the simulations discussed in this dissertation (the runs listed in Table 3.1), and who shared his knowledge and code with me, enabling me to run my own simulations. Additionally, I must acknowledge all of my other collaborators who contributed to the work presented in this dissertation: Yan-Fei Jiang, Iwona Kotko, Julian Krolik, Jean-Pierre Lasota, Greg Salvesen, Takayoshi Sano, and Evan Yerger.

This research was supported by the United States National Science Foundation under grant AST-1412417 and also in part by PHY11-25915. We also acknowledge support from the UCSB Academic Senate, and the Center for Scientific Computing from the CNSI, MRL: an NSF MRSEC (DMR-1121053) and NSF CNS-0960316. Numerical calculation was partly carried out on the Cray XC30 at CfCA, National Astronomical Observatory of Japan, and on SR16000 at YITP in Kyoto University, and the Janus supercomputer, which is supported by the National Science Foundation (award number CNS-0821794) and the University of Colorado Boulder. The Janus supercomputer is a joint effort of the University of Colorado Boulder, the University of Colorado Denver, and the National Center for Atmospheric Research.

Curriculum Vitæ

Matthew S. B. Coleman

Education

2017	Ph.D., Physics, University of California, Santa Barbara
2014	M.A., Physics, University of California, Santa Barbara
2011	B.S., Physics (Astrophysics), University of California, Santa Cruz

Professional Experience

2011-2017	Graduate Student Researcher, Department of Physics, University of California, Santa Barbara
2011-2014	Teaching Assistant, Department of Physics, University of California, Santa Barbara
2009-2011	Undergraduate Researcher, Department of Astronomy and Astrophysics, University of California, Santa Cruz
2009	Physics Tutor, Learning Support Services, University of California, Santa Cruz

First author publications

"Convective Quenching of Field Reversals in Accretion Disc Dynamos", Coleman, M. S. B., Yerger, E., Blaes, O., Salvesen, G. & Hirose, S., *MNRAS*, 467, 2625, 2017

"Dwarf Nova Outbursts with Magnetorotational Turbulence", Coleman, M. S. B., Kotko, I., Blaes, O., Lasota, J.-P., & Hirose, S., *MNRAS*, 462, 3710, 2016

Other publications

"Convection Causes Enhanced Magnetic Turbulence in Accretion Disks in Outburst", Hirose, S., Blaes, O., Krolik, J. H., Coleman, M. S. B., & Sano, T., *ApJ*, 787, 1, 2014

Note for the reader

While it may seem weird for a single author to refer to oneself in the plural, I will do so from now on as a way to signify that I did not do this alone.

Abstract

Convection Affects Magnetic Turbulence in White Dwarf Accretion Disks

by

Matthew S. B. Coleman

In this dissertation we focus on the accretion disks which surround accreting white dwarfs as they are some of the most abundant and well observed accretion disk systems. In many of these systems (e.g. dwarf novae), the accretion disk switches between a low luminosity state (quiescence) and a high luminosity state (outburst). These outbursts enable observers to place numeric constraints on the strength of turbulence (i.e. the α parameter) in these accretion disks. This dissertation focuses on results of local (stratified shearing-box) computer simulations of white dwarf accretion disks, and uses these results to gain a better theoretical understanding of these disks. As expected we find that the magnetorotational instability (MRI) is the predominant source of turbulence in these systems. However, we also find that hydrodynamic convection plays a key role as well. During the high luminosity state the disk becomes convectively unstable and the resulting convection enhances the MRI by seeding it with vertical magnetic field. This provides the first robust theoretical mechanism for enhancing turbulence *only* in outburst; a result required by observations. This convection also prevents the magnetic dynamo in our simulations from exhibiting the typical behavior of magnetic field reversals propagating vertically through-

out the simulation. We also examine how the convection in our simulation changes the prior theoretical understanding of these disks. Specifically, we examine how these disks change luminosity over time by generating synthetic lightcurves using a modified disk instability model. These models can successfully reproduce observed outburst and quiescence durations, as well as outburst amplitudes. However, these lightcurves exhibit reflares in the decay from outburst, which are not generally observed in dwarf novae. Although, we highlight the problematic aspects of the quiescence physics in the disk instability model and MRI simulations that are responsible for this behavior.

Contents

Chapter 1

Introduction

With the exception of the cosmic microwave background, virtually every observable astrophysical object was created through the process of accretion: the accumulation of material, typically through gravitational attraction. This includes every star in the universe and all of the planets that orbit them. As the clouds and collections of gas which form these objects contract under the influence of gravity, they typically reach a point where net rotation dominates the dynamics, restricting further collapse. This scenario naturally leads to a disk structure, explaining why accretion disks are so prevalent and fundamental in astrophysics.

Without some sort "viscous" dissipation, the material in these disk would continually rotate in circular orbits and never be accreted inwards. For sufficiently ionized accretion disks, the magnetic turbulence produced by the magnetorotational instability (MRI) provides this dissipation (Balbus & Hawley, 1991; Hawley & Balbus, 1991). The

strength of this turbulence is typically parameterized by the Shakura & Sunyaev (1973) α parameter[1].

Since the pivotal role that the MRI plays in accretion was discovered (Balbus & Hawley, 1991), there have been many works simulating the magnetic turbulence generated by the MRI (e.g. Hirose et al. 2006; Davis et al. 2010; Shi et al. 2010; Guan & Gammie 2011; Simon et al. 2012; Sorathia et al. 2012; this work). When the disk is assumed to be perfectly conducting without net vertical magnetic flux, the MRI tends to produce α values of a few percent ($\alpha \sim 0.01$). However, there are observations of accretion disks which are inconsistent with this value of α.

Constraints on α in naturally occurring accretion disks primarily come from observations of episodic outbursts in accretion disks around white dwarf stars (Lasota, 2001; Kotko & Lasota, 2012), and from recent Atacama Large Millimeter/submillimeter Array (ALMA) observations of protoplanetary disks (e.g. Flaherty et al., 2015). The trouble with protoplanetary disks is that they are largely neutral (i.e. low conductivity) meaning that the MRI will be much weaker or even nonexistent (Lesur et al., 2014; Simon et al., 2015). Observations of these disks result in low inferred values of $\alpha \lesssim 10^{-3}$ (Flaherty et al., 2015). We therefore focus our efforts on accreting white dwarfs.

[1] The MRI and α will be expanded upon in Chapter 2.

1.1 Accreting White Dwarfs

The variability of cataclysmic variables (CVs) and accreting white dwarfs as a whole[2] provides a means for observationally constraining the value of α in very conductive disks[3]. Accreting white dwarfs are the most understood class of accretion disks, because white dwarfs are the most abundant stellar remnant/compact object and their accretion is bright in visible light. However, there is still more we can learn from their accretion.

In accreting white dwarf systems the primary star is a white dwarf, and is mutually gravitationally bound to a second less massive star, the secondary. Accretion in these systems is typically done through Roche lobe overflow and accretion is often mediated through a disk as a result of the angular momentum of the binary. These systems have orbital periods $P_{\rm orb} \lesssim 10$ h, with a gap in the population distribution around $P_{\rm orb} \sim 2.5$ h, and for hydrogen rich systems there is an observed period minimum of $P_{\rm orb} \approx 75$ min (Warner, 1995). For hydrogen-deficient systems the minimum orbital period is $P_{\rm orb} \approx 10$ min Kotko et al. (2012)[4].

The gap in the observed population of CVs from orbital periods $2\text{ h} \lesssim P_{\rm orb} \lesssim 3$ h, the *period gap*, is associated with physical evolution of the binary. The secondary can first fill its Roche lobe at a variety of orbital periods up to the period maximum $P_{\rm orb} \lesssim 10$ h, which

[2]There does not seem to be consensus amongst the community on whether CVs is synonymous with accreting white dwarfs or a subset thereof. We therefore use the term accreting white dwarf to be explicitly more inclusive. We use CV to describe an accreting white dwarf whose secondary is a hydrogen dominated star that has not evolved past the main sequence.

[3]With the possible exception of dwarf novae in quiescence, whose low ionization fraction may be important. See Section 7.3 for more details.

[4]This significant difference in obital period minimums is one of the reasons hydrogen-deficient accreting white dwarf systems are not true CVs.

is roughly where the largest secondaries first come into contact with the Roche lobe. For systems with orbital periods above the period gap, magnetic braking is the predominant sink of angular momentum, driving these systems to smaller separations. At $P_{\rm orb} \approx 3$ h the mass accretion timescale becomes shorter than the thermal time eventually causing the secondary to become fully convective, which halts magnetic breaking (King & Kolb, 1995). At this point the secondary contracts to regain thermal equilibrium, causing it to separate from its Roche lobe. This terminates accretion until emission of gravitational waves brings the brings the secondary back into contact when $P_{\rm orb} \approx 2$. Eventually at the period minimum ($P_{\rm orb} \approx 75$ min), the secondary has lost too much mass to continue fusing hydrogen and becomes a brown dwarf supported by degeneracy pressure. This inverts the mass radius relation; thus, as the secondary losses mass it grows in size and the orbit expands keeping the secondary in contact with the Roche lobe.

1.1.1 Dwarf Novae

Dwarf novae (DNe) are transient optical outbursts observed from close binary systems containing an accreting white dwarf and are a subclass of CVs. These outbursts have amplitudes up to ~ 8 mag and last 2-20 days, with recurrence times ranging from ~ 4 days to years (Lasota, 2001). SS Cygni is perhaps the most well studied DN, and is often considered the prototype for the class.

SS Cygni was discovered in late 1896 by Louisa D. Wells (Pickering, 1896; Hazen, 1997), and is the second discovered DN. Remarkably, every outburst since its discovery

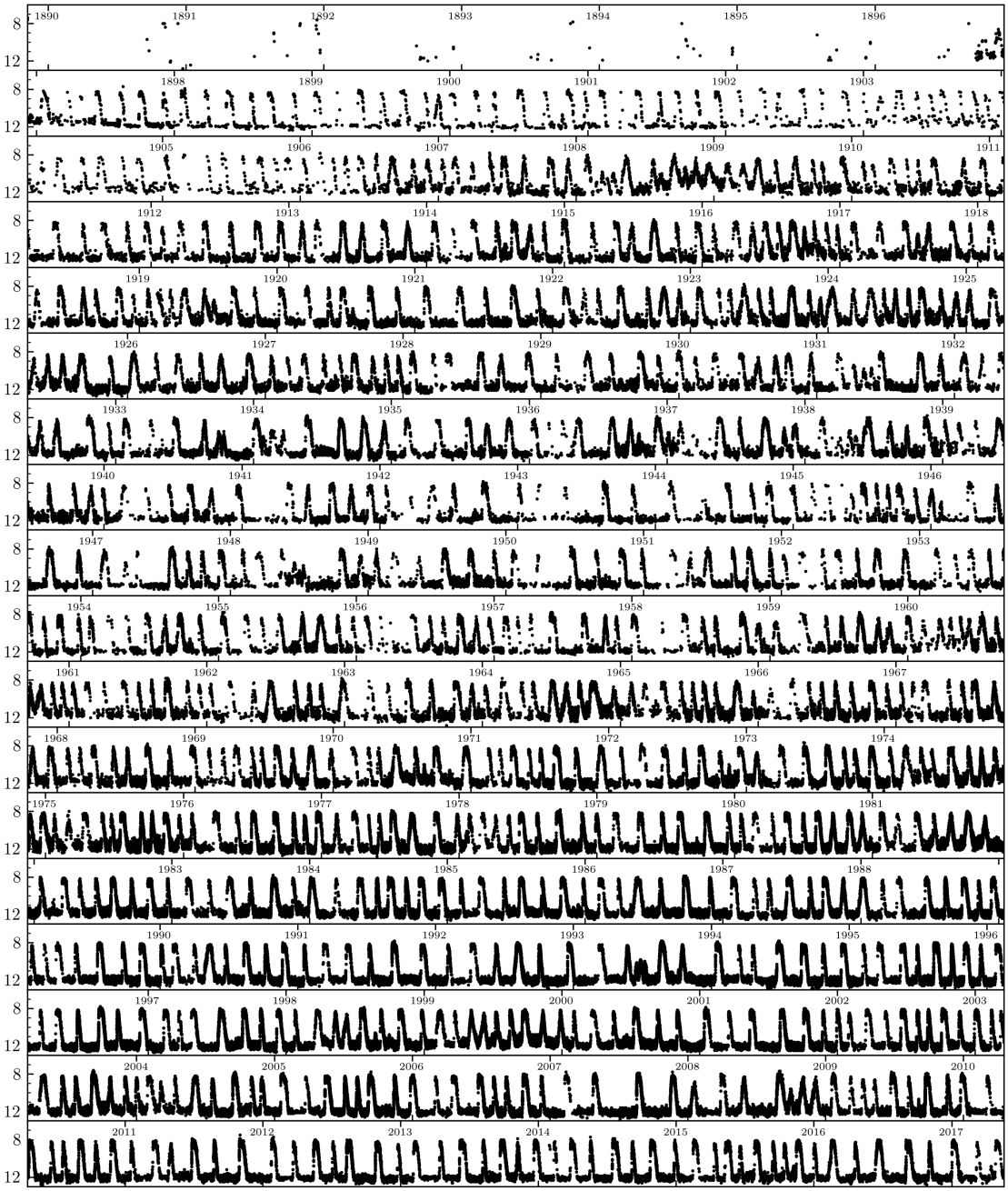

Figure 1.1 The full historic visual lightcurve of dwarf nova SS Cygni, including data from archival plates that predate its discovery towards the end of 1896. The vertical axis shows the apparent magnitude and the beginning of each year it marked. Most of the these data are observations from the AAVSO international database (Kafka, 2016, `https://www.aavso.org`), some of the data from late 1896 to 1907 was missing from the publicly available data, so it is taken from Fig. 1 of Cannizzo & Mattei (1992).

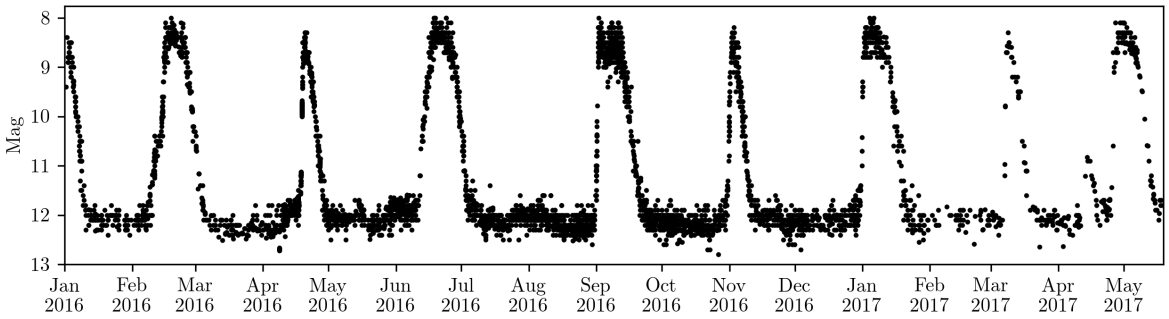

Figure 1.2 Recent visual lightcurve of dwarf nova SS Cygni. The vertical axis shows the apparent magnitude and the beginning of each calendar month (in UTC) is marked on the horizontal axis. These data are observations from the AAVSO international database (Kafka, 2016, `https://www.aavso.org`).

has been observed and recorded, as demonstrated by Fig 1.1. We also show only the more recent data in Fig. 1.2 so that the details of individual outbursts can be seen. This amazing data would not have been possible without amateur astronomers and the American Association of Variable Star Observers (AAVSO; Kafka, 2016), indicating the important role amateur astronomers play in scientific discovery.

Many theorists in the CV community are also fond of SS Cygni, because it is one of the few systems where theory won a conflict with observations, with the victor of this dispute being the disk instability model (DIM; see Section 2.2 for more details on the model itself). The DIM is what created our current physical understanding of how DN outbursts[5] work, which we recount before returning to the conflict described above. DNe spend most of their time in the low luminosity, "quiescent" phase. During quiescence the entire accretion disk is cold and the vast majority of hydrogen is neutral. During this

[5]DNe have exhibited several types of outbursts, such as super outbursts and standstills (see Warner, 1995, for more details.). In this work we limit our consideration only to "normal" or "standard" outbursts.

stage the secondary is transferring mass onto the accretion disk faster than the disk is able to process it. This causes the disk to accumulate matter, increasing its temperature and surface mass density. Eventually an annulus, at some radius in the disk, warms to the point where the ionization of hydrogen starts to become substantial. This causes a significant increase in the opacity making cooling mechanisms inefficient, resulting in the loss of thermal equilibrium.

This annulus then undergoes rapid heating until its hydrogen is mostly ionized and the opacity begins to decrease. The transition of this annulus to the hot outburst state triggers a heating front, which propagates throughout the disk, bringing the whole disk into the hot, ionized outburst state. The effect of this hydrogen ionization instability is to significantly and rapidly increases both the disk temperature and the accretion rate onto the surface of the white dwarf. These two effects directly correlate to a large increase in luminosity, which is observed as an outburst, and the increase in accretion rate causes the disk to transport more mass onto the primary than it receives from the secondary. This then causes the disk to cool and lose mass. Eventually, an annulus undergoes catastrophic cooling, generating a cooling front which propagates throughout the disk bringing the DN back into the cold, neutral quiescent state, finishing the outburst cycle.

However this outburst cycle only works when the mass transfer rate from the secondary is trying to drive the accretion disk to a temperature in between the outburst and quiescent states. If the mass transfer rate from the secondary exceeds a critical value then the accretion disk would stay in the hot "outburst" phase indefinitely, meaning that

this accreting white dwarf would not be a DN, but instead a "nova-like variable". When the Hubble Space Telescope (HST) measured the parallax of (and thus distance to) SS Cygni (Harrison et al., 1999), their measurement placed the DN far enough away that it must have a mass transfer rate too large to exhibit outbursts (Schreiber & Gänsicke, 2002; Schreiber & Lasota, 2007).

Before this dispute, the DIM had been successful in explaining the outbursts of SS Cygni (as well as other DNe), and was even used to place constraints on the level of turbulence (i.e. α) occurring in these accretion disks. This is possible because the outburst duration and periodicity of these events provide measurements of the viscous time scale, which is inversely proportional to α. However, the HST observation brought these results into doubt. In their aptly titled paper "An accurate geometric distance to the compact binary SS Cygni vindicates accretion disc theory", Miller-Jones et al. (2013) presented very long baseline interferometric (VLBI) radio observations that placed SS Cygni closer, in agreement with the DIM. This led to a reanalysis of the original HST measurement, which was found to be consistent with the Miller-Jones et al. (2013) VLBI measurements, after some calibration errors were rectified (Nelan & Bond, 2013), thus vindicating the DIM.

1.2 Motivation

Through the use of the DIM and other methods, we are continually learning more about accreting white dwarfs and their variability. This information can then be applied to

other accretion disk systems, which exhibit variations on much longer time scales such as black hole and neutron star X-ray binaries. There are a lot more similarities between the three systems than is generally acknowledged. For example, the outbursts in all three systems are powered by the hydrogen ionization instability and despite some differences in their state transitions there remains some similarities (see Hameury et al., 2017, for a recent detailed discussion). Additionally, white dwarfs exhibit radio jets in outbursts analogous to the jets observed in black hole and neutron star binaries (Russell et al., 2016).

Advances on basic accretion disk theory have also been made over roughly the past two decades. Local stratified shearing-box simulations have improved our understanding of how the MRI generates local turbulence (Hawley et al., 1995; Hirose et al., 2014). These simulations focus on a small co-rotating domain which straddles the disk in the vertical direction (perpendicular to the disk), and assumes a Cartesian grid (see Chapter 3 for more details). When there is no net vertical magnetic flux these types of simulations generally give time-averaged α values of approximately two or three percent (Hirose et al., 2006; Davis et al., 2010; Shi et al., 2010; Guan & Gammie, 2011; Simon et al., 2012). The inability of these simulations to produce a large α ($\gtrsim 0.1$) has been a substantial hurdle in reconciling MRI physics with the DIM (Lasota, 2001; Kotko & Lasota, 2012), and rectifying this is one of the prime motivators of this work.

1.3 Previously Published Work

1. The content from Section 3.2 to the end of Chapter 4 is mostly taken from Hirose et al. (2014).

2. The content of Chapter 5 first appeared in Coleman et al. (2017).

3. The content of Chapter 6 first appeared in Coleman et al. (2016).

Chapter 2

Accretion as We Knew It

Accretion disks are rotationally supported structures, with each annulus rotating at its corresponding Keplerian frequency. In order for these *accretion* disks to actually accrete (i.e. for matter to fall onto the central object) angular momentum and energy must be extracted from the disk. While radiation is effective at removing energy it is inefficient at removing angular momentum. This is why some form of viscosity[1] within the accretion flow is needed.

2.1 α-Disk Model

Our total ignorance of what this viscosity was or how it should be treated prevented development in this field until Shakura & Sunyaev (1973) devised a novel way of parameterizing this ignorance. They simply assumed that the vertically integrated turbulent/viscous

[1] In actuality, this is an effective viscosity arising from the stresses produced by turbulence.

stress was proportional to the vertically integrated thermal pressure:

$$\int_{-\infty}^{\infty} w_{r,\phi}\,\mathrm{d}z = \alpha \int_{-\infty}^{\infty} P_{\mathrm{therm}}\,\mathrm{d}z, \tag{2.1}$$

where $w_{r,\phi}$ is the radial-azimuthal component of the stress tensor, P_{therm} is the thermal pressure (gas plus radiation) and α (with $\alpha < 1$ for subsonic turbulence) is the proportionality constant which gives the α-disk model its name. Alternatively, this can be written in terms of the effective viscosity ($\bar{\nu}_{\mathrm{eff}}$):

$$\frac{3}{2}\bar{\nu}_{\mathrm{eff}}\Sigma\Omega = \alpha \int_{-\infty}^{\infty} P_{\mathrm{therm}}\,\mathrm{d}z, \tag{2.2}$$

where $\Sigma = \int \rho\,\mathrm{d}z$ is the surface mass density and Ω is the Keplerian orbital frequency. This formalism implicitly assumes that energy is dissipated locally, near where the corresponding stresses occur. With the additional assumptions that the accretion disk is optically thick and geometrically thin, this α prescription enables quantitative calculations, such as the effective temperature of a disk as a function of radius, and many of these calculations are relatively insensitive to α.

It is worth commenting that this model works by compressing our ignorance into one parameter; this is both its power and its downfall. Observations of accretion disks in combination with this model have placed empirical constraints on α, mainly through the disk instability model. However, the α-disk model does nothing to inform us on the physical phenomena which drive the stresses and thus set α.

2.2 Disk Instability Model

The DIM has been successful in its attempts to use the α-disk framework to model variability caused by instabilities within accretion disks (Lasota, 2001; Kotko et al., 2012). Comparing the outcomes of the DIM with observations (primarily of DNe) is what has placed the best constraints on α. Here we expand on some of the equations and assumptions used by the DIM. For a more detailed explanation we refer the reader to Hameury et al. (1998), which our DIM used in Chapter 6 is based on.

In short the DIM uses a library of vertical structure models to compute the fluxes of various quantities between adjacent annuli in an accretion disk. This implicitly decouples the vertical and radial structures of the disk. This decoupling should be a reasonable approximation as long as the vertical gradients are much sharper than the radial ones.

With this decoupling, the radial evolution of the disk is computed through the equations for mass, angular momentum, and energy conservation, which in an α-disk can be written as:

$$\frac{\partial \Sigma}{\partial t} = -\frac{1}{r}\frac{\partial}{\partial r}(r\Sigma v_{\rm r}) + \frac{1}{2\pi r}\frac{\partial \dot{M}_{\rm ext}}{\partial r} \tag{2.3}$$

$$j\frac{\partial \Sigma}{\partial t} = -\frac{1}{r}\frac{\partial}{\partial r}(r\Sigma j v_{\rm r}) + \frac{1}{r}\frac{\partial}{\partial r}\left(-\frac{3}{2}r^2\Sigma\nu\Omega_{\rm K}\right) + \frac{j_{\rm k}}{2\pi r}\frac{\partial \dot{M}_{\rm ext}}{\partial r} - \frac{1}{2\pi r}T_{\rm tid}(r), \tag{2.4}$$

$$\frac{\partial T_{\rm c}}{\partial t} = \frac{2(Q^+ - Q^- + J)}{C_P\Sigma} - \frac{\Re T_{\rm c}}{\mu C_P}\frac{1}{r}\frac{\partial (r v_{\rm r})}{\partial r} - v_{\rm r}\frac{\partial T_{\rm c}}{\partial r}, \tag{2.5}$$

where Σ is the surface mass density, $\dot{M}_{\rm ext}(r)$ is the rate at which the disk is being fed at radius r, v_r the radial velocity, $j = (GM_1 r)^{1/2}$ is the specific angular momentum,

$\Omega_K = (GM_1/r^3)^{1/2}$ is the Keplerian angular velocity (M_1 being the mass of the accreting object), ν is the kinematic viscosity coefficient, $j_{\rm k}$ the specific angular momentum of the material transfered from the secondary, $T_{\rm tid}$ is the torque due to tidal forces, Q^+ and Q^- are the surface heating and cooling rates respectively, J is the radial energy flux, $T_{\rm c}$ is the central temperature of the disk, $\Re$ is the ideal gas constant, μ is the mean molecular weight, and C_P is the specific heat. Additionally, Q^+ and J typically depend on ν, which itself is determined by the α disk model, and $Q^- = \sigma T_{\rm eff}^4$ is the radiative flux, where $T_{\rm eff}$ is the effective temperature.

The dependence of the equations on both $T_{\rm c}$ and $T_{\rm eff}$ (which is determined by the surface of the disk) requires the computation of vertical structures to connect these two temperatures. This is done through the following equations

$$\frac{{\rm d}\,P}{{\rm d}\,z} = -\rho\Omega^2 z \tag{2.6}$$

$$\frac{{\rm d}\,\varsigma}{{\rm d}\,z} = 2\rho \tag{2.7}$$

$$\frac{{\rm d}\ln T}{{\rm d}\ln P} = \nabla \tag{2.8}$$

$$\frac{{\rm d}\,F_z}{{\rm d}\,z} = Q^+ = \frac{3}{2}\alpha_{\rm eff}\Omega_{\rm K}P, \tag{2.9}$$

where P, ρ and T are the pressure, density and temperature respectively, $\varsigma(z)$ is the surface mass density between $\pm z$, $F_{\rm z}$ the vertical energy flux and ∇ the temperature gradient of the structure. ∇ is often set by radiative diffusion

$$\nabla_{\rm rad} \equiv \frac{3\kappa_{\rm R}\rho H_P F_{\rm tot}}{16\sigma T^4}, \tag{2.10}$$

where $\kappa_{\rm R}$ is the Rosseland mean opacity, H_P is the pressure scale height, and $F_{\rm tot}$ is the total flux passing through a given height. If this gives a superadiabatic gradient then it becomes necessary to use some prescription for convection such as mixing length theory (see Section 6.3.3).

The associated boundary conditions for these equations are as follows: the midplane boundary conditions are

$$z = 0 \tag{2.11}$$

$$F_z = 0 \tag{2.12}$$

$$\varsigma = 0 \tag{2.13}$$

$$T = T_0 \tag{2.14}$$

$$P = P_0, \tag{2.15}$$

and the exterior boundary conditions are

$$\kappa_R P = \frac{2}{3}\Omega^2 z \tag{2.16}$$

$$F_z = \sigma T^4 \tag{2.17}$$

$$\varsigma = \Sigma. \tag{2.18}$$

With these in place one can then relate disk surface conditions to the midplane and evolve the radial evolution equations. This enables the DIM to compute fluxes over time (i.e.

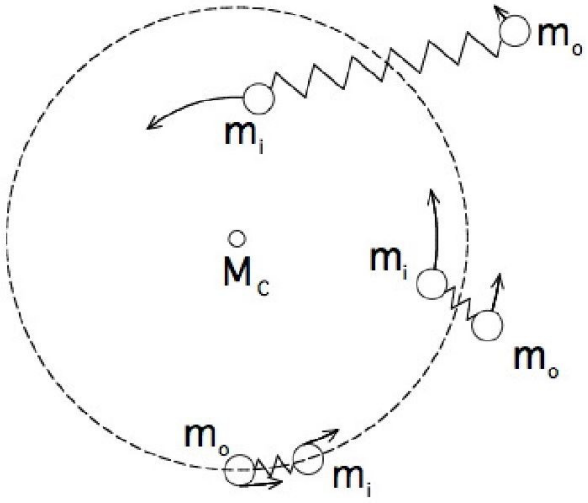

Figure 2.1 Cartoon depiction of the magnetorotational instability. The schematic spring connecting the inner mass ($m_{\rm i}$) from the outer mass ($m_{\rm o}$) represents a magnetic field line which threads these masses. The use of a spring schematic here is symbolic of the fact that the magnetic field acts like a spring to linear order (Balbus & Hawley, 1998). This configuration rotates/orbits around the central mass ($M_{\rm c}$).

light curves), giving if the power to constrain α through comparisons with observations.

However, the DIM is incapable of identifying the mechanisms which set α.

2.3 Magnetorotational Instability

This ignorance of what determines α was rectified by Balbus & Hawley (1991) when they discovered the importance of the magnetorotational instability (MRI) in accretion disks[2]. Balbus & Hawley (1998) note that the MRI is mathematically equivalent to considering two masses adjoined with a spring (see Fig. 2.1). In this depiction, the spring represents the magnetic field threading the two masses, which themselves represent two perfectly

[2]What is now called the magnetorotational instability was first discovered by Velikhov (1959) in the context of Couette flows, and generalized by Chandrasekhar (1960). The power and generality of the MRI were not fully realized until Balbus & Hawley (1991).

conductive fluid parcels. In this picture the conductivity is analogues to how well the spring sticks to the masses[3]. We then consider rotation of this configuration around a central point with angular frequency $\Omega(R)$ given as a function of radial distance. If one mass is perturbed inwards then it will start to rotate faster compared to the outer mass. The spring is unable to compensate for this displacement if

$$\frac{\mathrm{d}\ln\Omega}{\mathrm{d}\ln R} < 0 \tag{2.19}$$

and

$$\omega_{\mathrm{spring}} < \Omega\sqrt{\left|2\frac{\mathrm{d}\ln\Omega}{\mathrm{d}\ln R}\right|}, \tag{2.20}$$

where ω_{spring} is the natural oscillation frequency of the spring. In this situation, the distance between the masses increases and the spring stretches. This torques down the inner mass causing it to fall closer to the central object while simultaneously torquing up the outer mass and pushing it outwards, effectively transferring angular momentum from the inner mass to the outer one. This makes the spring stretch even more rapidly, signifying that this configuration runs away: the hallmark of a linear instability. In actuality, this spring analogy is only valid to linear order, and as the perturbation grows it eventually becomes non-linear breaking the analogy. At this point the flow becomes highly dynamical leading to the development of turbulence (Hawley & Balbus, 1991). For Keplerian rotation $\mathrm{d}\ln\Omega/\mathrm{d}\ln R = -3/2$, making the MRI a robust source of turbu-

[3]For most of this dissertation we will assume a perfectly conducting plasma, however we discuss the validity of this assumption in Section 7.3.

lence for all conductive, weakly magnetized accretion disks. As such, the MRI is widely considered to be the only viable mechanism for transporting angular momentum through local turbulence in accretion disks (Balbus & Hawley, 1991; Hawley et al., 1995) and this magnetic turbulence is one of the primary physical mechanisms which determine α.

2.4 Energy transport

The turbulence created by the MRI or other instabilities can form eddies at many different length scales and energy tends to be transported to smaller scales until it reaches the size associated with some form of dissipative process, such as viscosity or resistivity. At this point kinetic and magnetic energy are turned into heat and are radiated away. This process of taking energy from the largest eddies down to dissipative scales is called the *turbulent cascade*. Therefore, as long as these eddies are not significantly larger than the disk thickness, kinetic and magnetic energy are effectively dissipated locally, enabling one to use the α-disk model.

This turbulent cascade also ensures that energy is being constantly dissipated as radiation throughout the vertical extent of the disk, and to maintain a thermal equilibrium the disk must get this heat out. For the vast majority of accretion disks, the easiest way for photons to escape is in the vertical direction. They do so in a random walk as they interact with various electrons and atoms (this is what sets the opacity), which is well approximated by radiative diffusion. Once the photons reach the photosphere they

become free streaming and their energy is liberated from the disk[4].

Until recently, radiative diffusion had been presumed to be the predominant mechanism of extracting heat from accretion disks (other then AGN). However, it was shown that, under certain circumstances (e.g. radiation pressure dominated, very optically thick), advection of radiation can be an important energy transport mechanism (Hirose et al., 2009; Blaes et al., 2011). Radiation advection dominates diffusion when the speed of bulk vertical flows exceeds that of radiative diffusion. In this regime photons are advected with the fluid flow faster than they can diffuse outwards. However, to actually achieve this, the disk needs substantial vertical circulation, and Blaes et al. (2011) found that the previously discovered magnetic buoyancy (further discussed in the following section) provided this. Later in this dissertation we will also analyze convection's role in advecting heat.

2.5 Dynamos and the Butterfly Diagram

As alluded to earlier in this chapter, magnetic fields play an important role in accretion disks. From the MRI alone we know that even weak magnetic fields can robustly generate turbulence in conductive accretion disks. Moreover, this magnetic turbulence is fundamentally tied to the emergence of large scale magnetic dynamos. The most predominant of these is the so called butterfly diagram, named for its resemblance to the time inverse of the solar sunspot butterfly diagram. This dynamo is characterized by quasi-periodic

[4]For accretion disks around neutron stars and black holes, self-irradiation (i.e. the inner disk irradiating the outer disk) is often important.

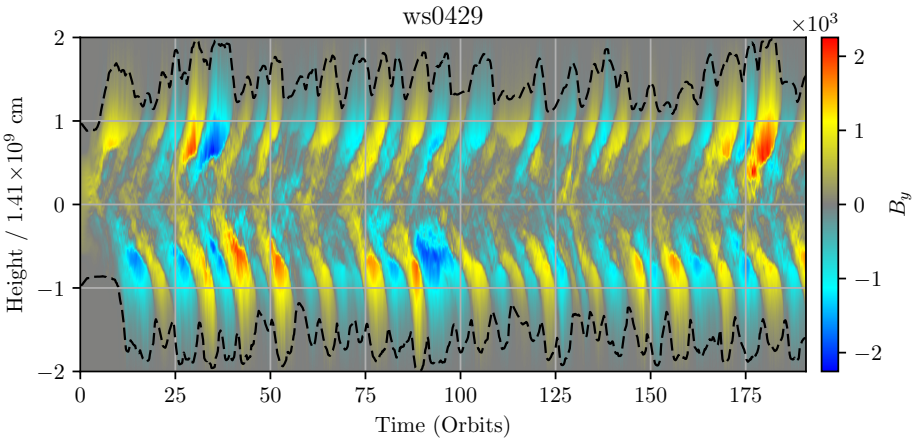

Figure 2.2 Horizontally-averaged azimuthal magnetic field (B_y) as a function of time and height for an accretion disk simulation (ws0429). This data should be interpreted as the time evolution of the vertical structure at one annulus in an accretion disk average over its azimuthal extent. The dashed black lines show the time-dependent heights of the photospheres in the horizontally averaged structures. This plot shows the standard pattern of field reversals normally associated with the butterfly diagram, and shows up again in figure 5.1 and will be discussed in more detail in Chapter 5.

field reversals of the azimuthal magnetic field (B_y) with periods of ~ 10 orbits (Brandenburg et al., 1995; Davis et al., 2010). These magnetic field reversals start at the midplane and move outwards, making the butterfly pattern seen in Fig. 2.2. This outward motion can be explained by the buoyant advection of magnetic flux tubes (Gressel, 2010), and as mentioned in the previous section, this buoyant motion can carry a significant amount of heat with it. While this explains how the reversals propagate, there is currently no consensus on the physical mechanism driving the reversals (e.g. Brandenburg et al., 1995; Gressel, 2010; Shi et al., 2010, 2016; Squire & Bhattacharjee, 2015).

Chapter 3

Simulation Framework

Most phenomena in astrophysics are related to some sort of fluid, making hydrodynamics, the study of fluid flows and motions, an essential part of understanding the universe. All fluids are characterized by their weak-to-nonexistent restoring forces. That is, once a fluid experiences a disturbance or deformation it will continue to deform until frictional effects have removed all the kinetic energy from the system. Additionally, without the help of viscosity or magnetic fields, fluids have trouble supporting shear stresses[1], with inviscid fluids completely incapable of supporting shear stresses. Gases, plasmas, and liquids all exhibit these qualities and therefore can be studied as hydrodynamic systems, and be simulated using the framework in this chapter.

Each of the three phases listed above is distinct. Liquids are (mostly) incompressible, i.e. they maintain the same density and volume under various pressures. Gases and

[1]Shear stresses are easily visualized on the surface of a cube as a force that acts tangent to one of the faces.

plasmas may, however, change their density and volume in a manner which conserves mass. Unlike gases, plasmas contain ionized material that is affected by electromagnetic fields. Thus most astrophysical "gases" are actually plasmas[2] and are governed by magnetohydrodynamics (MHD), which couples hydrodynamics to the Maxwell equations. For plasmas, the magnetic field (either externally imposed or internally generated) can provide its own restoring force and also introduces anisotropic behavior, as plasma can more readily flow along the magnetic field lines than perpendicular to them.

The remainder of this chapter discusses the equations required to model astrophysical fluids, as well as describing a means to solve the time evolution of these equations with computer simulations.

3.1 Magnetohydrodynamics

The equations of (magneto)hydrodynamics, while widely used, are not fundamental laws of nature. They are approximations, formally derived from the Liouville's theorem, which describes how the phase space volume of a system of particles must be conserved. This $6N$-dimensional equation can be reduced, through truncation of the BBGKY-hierarchy, to the 6-dimensional Boltzmann equation

$$\frac{\partial f}{\partial t} + \frac{\partial \boldsymbol{x}}{\partial t} \cdot \nabla_{\boldsymbol{x}} f + \frac{\partial \boldsymbol{p}}{\partial t} \cdot \nabla_{\boldsymbol{p}} f = \left(\frac{\partial f}{\partial t} \right)_{\text{coll}}, \tag{3.1}$$

[2]In astrophysics it is common to refer to plasmas as gases. This is because there is not a clear line separating them and even mostly neutral gases with low ionization fractions can still be influenced by magnetic fields.

where $\boldsymbol{x}$ is position, $\boldsymbol{p}$ is momentum, t is time, and f is the phase space distribution, i.e. $f(\boldsymbol{x}, \boldsymbol{p})$ is the number of particles within $\mathrm{d}\boldsymbol{x}$ of $\boldsymbol{x}$ and $\mathrm{d}\boldsymbol{p}$ of $\boldsymbol{p}$, and $\left(\frac{\partial f}{\partial t}\right)_{\text{coll}}$ is a complicated integral describing collisions between particles. The three main conservation equations of hydrodynamics (mass, momentum, and energy) can be derived by taking the zeroth through second momentum moments of Eqn. 3.1, and making some simplifying assumptions, such as all the particles have finite momentum, the collisional mean free path is small, relativistic effects are negligible, and that the plasma is neutral on most size scales. It is rather tedious and not terribly illustrative to actually derive these equations. Therefore we skip to the general solution of these conservation equations which have the same form:

$$\frac{\partial g}{\partial t} + \nabla \cdot F_g = S_g^+ - S_g^-, \tag{3.2}$$

where g is an unspecified fluid parameter, F_g is the flux of g (i.e. the rate a which g crosses some cross-sectional surface), S_g^+ describes the sources of g and S_g^- describes the sinks of g. Mass, momentum and energy conservation are as follows

$$\frac{\partial \rho}{\partial t} + \nabla \cdot (\rho \boldsymbol{v}) = 0 \tag{3.3}$$

$$\frac{\partial \rho \boldsymbol{v}}{\partial t} + \nabla \cdot \left[\rho \boldsymbol{v}\boldsymbol{v} + \left(P + \frac{B^2}{2\mu_0}\right)\mathsf{I} - \frac{\boldsymbol{B}\boldsymbol{B}}{\mu_0}\right] = \rho \boldsymbol{g} \tag{3.4}$$

$$\frac{\partial e_{\text{tot}}}{\partial t} + \nabla \cdot \left[\left(e_{\text{tot}} + P + \frac{B^2}{2\mu_0}\right)\boldsymbol{v} - \boldsymbol{B}\left(\boldsymbol{B} \cdot \boldsymbol{v}\right)\right] = \rho \frac{\partial \phi}{\partial t}, \tag{3.5}$$

where ρ is the mass density, $\boldsymbol{v}$ is the fluid velocity, P is the gas pressure, $\boldsymbol{B}$ is the magnetic field, μ_0 is the vacuum permeability (we choose a cgs unit scheme where $\mu_0 = 1$), I is the

identity matrix, $\boldsymbol{g} = \nabla\phi$ is the gravitational field (or any external force per unit mass), ϕ is the potential energy associated with $\boldsymbol{g}$, $e_{\rm tot} = e + \rho v^2/2 + B^2/(2\mu_0) + \rho\phi$ is total energy density, and e is the gas internal energy density. Additionally, Ampere's laws

$$\nabla \times \boldsymbol{B} = \mu_0 \boldsymbol{J}, \tag{3.6}$$

was used to eliminate the current density $\boldsymbol{J}$ from the Lorentz force in Eqn. 3.4.

In order to understand how magnetic fields are advected with the fluid, we must combine Faraday's law

$$\nabla \times \boldsymbol{E} = -\frac{\partial \boldsymbol{B}}{\partial t} \tag{3.7}$$

with Ohm's law

$$\boldsymbol{E} + \boldsymbol{v} \times \boldsymbol{B} = 0, \tag{3.8}$$

where $\boldsymbol{E}$ is the electric field. Note that Eqn. 3.8 as written assumes that the plasma has zero resistivity, i.e. we are assuming ideal MHD. The combination of these equations yields the induction equation:

$$\frac{\partial \boldsymbol{B}}{\partial t} = \nabla \times (\boldsymbol{v} \times \boldsymbol{B}) \,. \tag{3.9}$$

This is often also referred to as flux freezing, as it mathematically signifies that magnetic flux is frozen into the fluid.

3.1.1 Equation of State

An astute reader might realize that Eqns. 3.3 - 3.5 and 3.9 are not sufficient to close the system of equations; one additional constraint is needed. This final constraint is a relation between density (ρ), gas pressure (P), and internal energy density (e). This type of relation is called an equation of state (EOS), as it is a set of equations which define state parameters. The most commonly used EOS is that of an ideal gas

$$P = (\gamma - 1)e, \tag{3.10}$$

where γ is the (constant) adiabatic index and is closely related to the degrees of freedom the gas has ($\gamma = 5/3$ for a monatomic gas). While this is often a reasonable approximation in astrophysical contexts, it is not sufficient for the work presented in this dissertation. We therefore utilize an EOS which takes into account molecular dissociation and ionization (see Appendix A for details). The results of this EOS for solar abundance (Anders & Grevesse, 1989) are plotted in Fig. 3.1.

3.2 Radiation Magnetohydrodynamics

Surprising as it might be, radiation (i.e. light) plays an important role in astrophysics. In fact, at the time of writing, there are only five astrophysical sources that have confirmed non-electromagnetic detections. The sun (Bellerive, 2004) and supernova 1987A (Bahcall et al., 1987) have both been detected in neutrinos (as well as in light), and there are

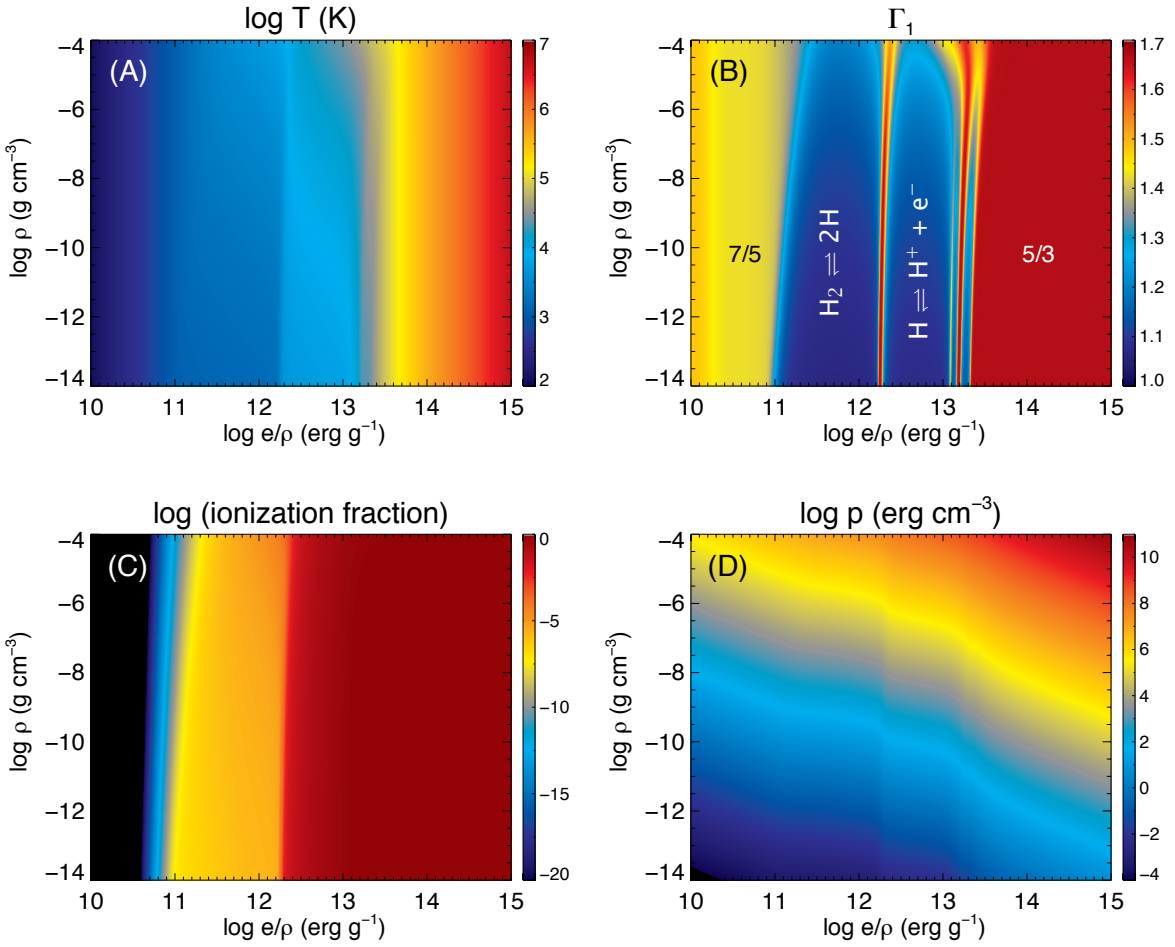

Figure 3.1 Non-ideal EOS computed from Saha equations: Gas temperature (A), generalized adiabatic index $\Gamma_1 \equiv (\partial \ln p / \partial \ln \rho)_s$ (B), ionization fraction (C), and pressure (D) as a function of specific energy density e/ρ (erg g^{-1}) and mass density ρ (g cm^{-3}).

also three confirmed gravitational wave sources[3] (Abbott et al., 2016b,a, 2017), which have no detected radiative counterpart. While cosmic rays have also been detected, their charged nature and interaction with magnetic fields makes it nearly impossible to localize their source. Nearly all other astrophysical objects have only been detected due to their emission of, or interaction with, photons. Therefore, for simulations and theories to make contact with observations it is paramount that radiation, and how it couples to MHD, be considered[4].

The basic radiation MHD equations that we use to run simulations are

$$\frac{\partial \rho}{\partial t} + \nabla \cdot (\rho \boldsymbol{v}) = 0, \tag{3.11}$$

$$\frac{\partial (\rho \boldsymbol{v})}{\partial t} + \nabla \cdot (\rho \boldsymbol{v}\boldsymbol{v}) = -\nabla P + \rho \boldsymbol{g} + \frac{1}{4\pi}(\nabla \times \boldsymbol{B}) \times \boldsymbol{B} + \frac{\kappa_{\mathrm{R}} \rho}{c} \boldsymbol{F}, \tag{3.12}$$

$$\frac{\partial e}{\partial t} + \nabla \cdot (e \boldsymbol{v}) = -(\nabla \cdot \boldsymbol{v}) P - (4\pi B(T) - cE)\, \kappa_{\mathrm{P}} \rho, \tag{3.13}$$

$$\frac{\partial E}{\partial t} + \nabla \cdot (E \boldsymbol{v}) = -\nabla \boldsymbol{v} : \mathsf{P}_{\mathrm{rad}} + (4\pi B(T) - cE)\, \kappa_{\mathrm{P}} \rho - \nabla \cdot \boldsymbol{F}, \tag{3.14}$$

$$\frac{\partial \boldsymbol{B}}{\partial t} - \nabla \times (\boldsymbol{v} \times \boldsymbol{B}) = 0, \tag{3.15}$$

where T is the gas temperature, E is the radiation energy density, $\mathsf{P}_{\mathrm{rad}}$ is the radiation pressure tensor, $\boldsymbol{F}$ is the radiation energy flux, $B(T) = \sigma_{\mathrm{B}} T^4/\pi$ is the Planck function (σ_{B} is the Stefan-Boltzmann constant), κ_{R} is the Rosseland mean opacity, κ_{P} is the Plank mean opacity, and c is the speed of light. The above equations treat radiation in a wavelength integrated or "gray" manner.

[3]The rate at which these sources are detected suggests that this number may be outdated before the end of 2017.

[4]The remainder of this chapter is largely based on the methods section of Hirose et al. (2014).

As before, these equations are not sufficient to close the system. In addition to our EOS, we need a relation between E, $\boldsymbol{F}$ and $\mathsf{P}_{\rm rad}$. Following Turner & Stone (2001), we use a flux-limited diffusion approximation of radiative transfer, where the energy flux $\boldsymbol{F}$ and pressure tensor P are related to the energy density E as

$$\boldsymbol{F} = -(c\lambda(R)/\kappa_{\rm R}\rho)\nabla E \tag{3.16}$$

$$\mathsf{P}_{\rm rad} = \mathsf{f}(R)E, \tag{3.17}$$

where $\lambda(R) \equiv (2+R)/(6+3R+R^2)$ is the flux limiter with $R \equiv |\nabla E|/(\kappa_{\rm R}\rho E)$, and $\mathsf{f}(R) \equiv (1/2)(1-f(R))\mathsf{I} + (1/2)(3-f(R))\boldsymbol{nn}$ is the Eddington tensor with $f(R) \equiv \lambda(R) + \lambda(R)^2R^2$ and $\boldsymbol{n} \equiv \nabla E/|\nabla E|$.

3.2.1 Opacity

As noted above the equations of radiation MHD depend on opacity. The Planck-mean opacity $\kappa_{\rm P}$ and Rosseland-mean opacity $\kappa_{\rm R}$ we use for solar composition (Anders & Grevesse, 1989) are given as a function of density ρ and gas temperature T (Fig. 3.2). These tables combined data from three published opacity tables, Semenov et al. (2003), Ferguson et al. (2005) and the Opacity Project (OP; Seaton, 2005), so that the relevant temperature range ($10^3 < T < 10^6$ K) for DNe are covered. The different opacity tables are connected using linear interpolation where they are mostly consistent: the Semenov et al. (2003) and Ferguson et al. (2005) opacities are connected where dust sublimation occurs, and the Ferguson et al. (2005) and OP tables are connected at

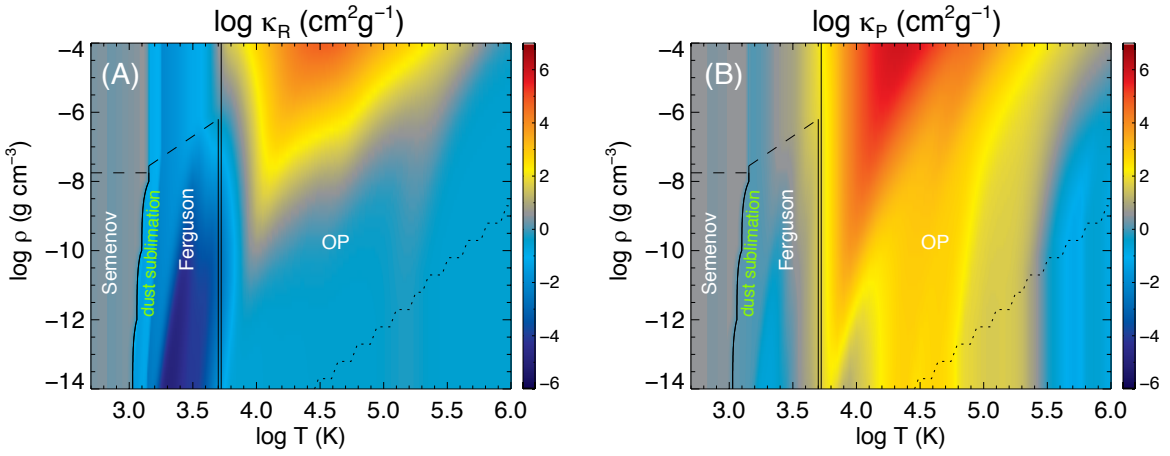

Figure 3.2 Mean opacities combining three published opacity tables by Semenov et al. (2003), Ferguson et al. (2005) and the Opacity Project (OPCD_3.3): Rosseland-mean opacity (A) and Planck-mean opacity (B) as a function of gas temperature T (K) and mass density ρ (g cm^{-3}). The solid curves are boundaries between adjacent opacity tables. The dashed curve denotes the upper bound of Semenov's and Ferguson's opacities while the dotted curve denotes the lower bound of OPCD_3.3.

$T = 10^{3.7}$ K. To estimate opacities which lie beyond the bounds of these tables, zero-gradient extrapolation is used, which has been shown to be a reasonable approximation for $T > 10^3$ K (c.f. Figure 1 in Malygin et al., 2013).

3.3 Local Accretion Disk Simulations

Evolving these equations to simulate physical properties of an accretion disk is a computationally expensive task. We therefore only simulate a small local co-rotating patch of an accretion disk within a given simulation[5]. This type of local approximation was first developed by Hawley et al. (1995) and is referred to as the vertically-stratified shearing

[5]Full global simulations of accretion disks incorporating all of the physics of interest are only now becoming feasible, and will be further discussed in Chapter 7.

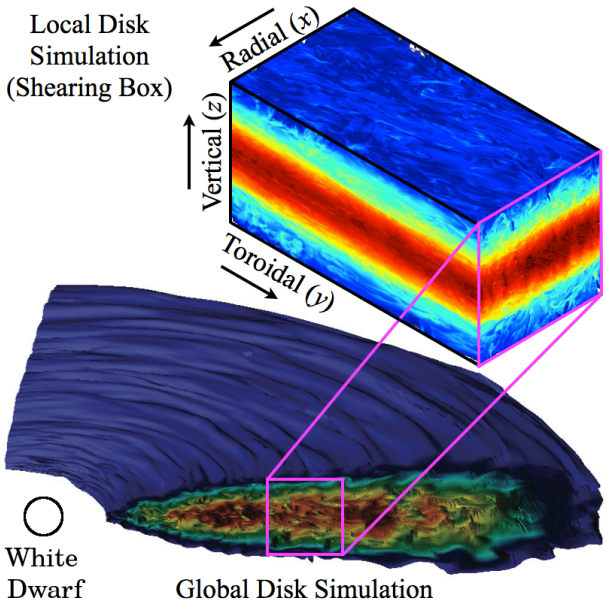

Figure 3.3 A depiction of a local shearing box simulation (data from Salvesen et al., 2016b) in relation to a global accretion disk simulation (data from Beckwith et al., 2011). Here the local Cartesian grid of the shearing box has been labeled. Thanks to Greg Salvesen for making this figure.

box approximation (see Fig. 3.3). The term vertically-stratified signifies that we take care to ensure that our vertical (direction perpendicular to the disk) domain is large enough to contain several pressure scale heights and that we keep track of the vertical gravity.

In the shearing box approximation, a local patch of an accretion disk is modeled as a co-rotating Cartesian frame (x, y, z) where the x, y, and z directions correspond to the radial, azimuthal, and vertical directions, respectively. To first order each annulus of the accretion disk rotates at its own Keplerian velocity, corresponding to a linearized Keplerian shear flow of $v_y = -(3/2)\Omega x$, where $\Omega = \sqrt{GM/R^3}$ is the Keplerian rotational frequency[6] a radial distance R from a central object of mass M. This choice of co-rotating

[6]The frequency Ω is a key defining parameter for a shearing box simulation.

frame is non-inertial, so the external forces on the fluid can be written as (Coriolis force + tidal force + vertical component of gravitational force, respectively)

$$\boldsymbol{g}_{\rm eff} = -2\Omega\hat{\boldsymbol{z}} \times \boldsymbol{v} + 3\Omega^2 x\hat{\boldsymbol{x}} - \Omega^2 z\hat{\boldsymbol{z}}, \tag{3.18}$$

where $\hat{\boldsymbol{x}}$ and $\hat{\boldsymbol{z}}$ are the unit vectors in the x and z direction, respectively. Note that at the center of the simulation domain, the centrifugal force and the radial component of gravity are equal and opposite in the co-rotating frame. Additionally, the vertical component of gravity here is approximate to second order in (z/R). Finally, this $\boldsymbol{g}_{\rm eff}$ should be used in place of $\boldsymbol{g}$ in Eqn. 3.12.

We chose the standard shearing box boundary conditions for the x and y directions which are shearing-periodic, and periodic, respectively (Hawley et al., 1995). The shearing-periodic condition is similar to the periodic condition but also takes into account the differential rotation between the inner and outer radial boundaries. Finally, outflow boundary conditions are used for the z boundaries of the simulation domain (Hirose et al., 2006). An interesting consequence of these boundary conditions is that the volume average of the vertical component of the magnetic field is conserved throughout the simulation run.

3.4 Zeus Code

The radiation MHD equations listed above are solved time-explicitly by the `Zeus` code, which uses the Method of Characteristics–Constrained Transport (MoC–CT) algorithm, except for the radiation-gas energy exchange terms $\pm(4\pi B - cE)\kappa_{\rm P}\rho$ and the radiative

diffusion term $-\nabla\cdot\boldsymbol{F}$ because these time scales are much shorter than the MHD time scale (Stone & Norman, 1992a,b; Turner & Stone, 2001). These radiation terms are coupled and solved time-implicitly using the multi-grid method with a Gauss-Seidel smoother and Newton-Raphson iteration (Tomida et al., 2013). Additionally, the gas temperature T used in evaluating the mean opacities is held fixed to that of the previous time step which linearizes the radiative diffusion equation.

Our computational implementation has no explicit resistivity and viscosity in the basic equations. Therefore any turbulent dissipation must occur through the sub-grid numerical dissipation. This model for sub-grid dissipation implicitly assumes that any energy that is transported to sub-grid scales will eventually follow the turbulent cascade down to dissipative scales, allowing it to be treated as a heat/energy source for the gas. This effectively results in an additional term $Q_{\rm diss}$ in the gas energy equation (3.13). This modification to the original `Zeus` algorithm ensures the conservation of total energy (Turner et al., 2003a; Hirose et al., 2006).

To avoid extremely small time-steps we use a density floor of 10^{-6} times the initial midplane density. We also use a similarly small internal energy floor for numerical stability (Hirose et al., 2006). The resulting cumulative artificial energy injection rate associated with these floors and numerical errors in the implicit solver is typically smaller than ~ 1 % of the cooling/heating rates of the final steady states achieved by the simulations.

3.5 Initial Conditions

The initial conditions within the disk photosphere are determined as follows: First, the vertical profiles of mass density $\rho(z)$, pressure $P(z)$ and temperature $T(z)$, as well the photosphere height h_0, are determined from an α model described in the following section (Sec. 3.5.1), by choosing two of the following initial values: an alpha (α_0), a surface mas density (Σ_0) and an effective temperature ($T_{\rm eff,0}$), where the third can be determined by the other two[7]. Then, the internal energy density is calculated via the EOS $e(z) = e(P(z), T(z))$ (see Appendix A), and the radiation energy density is calculated by assuming that the gas and radiation are in thermal equilibrium with each other (i.e. $E(z) = 4\sigma_{\rm B}T^4(z)/c$). Above the disk photosphere ($z > h_0$), we assume a uniform, low-density atmosphere with $\rho(z > h_0) = \rho(0) \times 10^{-6}$, $e(z > h_0) = e(h_0) \times 10^{-6}$, and $E(z > h_0) = E(h_0) \times 10^{-6}$.

For the initial velocity field we start with the linear Keplerian shear flow $\boldsymbol{v} = -\frac{3}{2}\Omega x\hat{\boldsymbol{y}}$, and add random perturbations with amplitude of 0.5 % of the local sound velocity to the x and z components of the velocity. A twisted azimuthal flux tube (with net azimuthal flux, but zero net vertical flux) is inserted at the center of the simulation domain to initialize the magnetic field and is initially confined within the photospheres. The magnetic field strength in this tube is uniform and the poloidal field component is, at maximum, 0.25 time the total field strength. The initial field strength is determined by the parameter β_0, which is defined as the the ratio of thermal pressure to magnetic pressure at the center

[7]There is a Σ range, where for a given α_0, there are two possible $T_{\rm eff,0}$.

of the flux tube. The outcome of the simulations are insensitive to β_0 and the shape of the flux tube, as long as the preliminary development of the MRI is well resolved.

3.5.1 Vertical Structure

We compute vertical structures of disks in thermal equilibria based on the alpha prescription following Mineshige & Osaki (1983), with the assumption of optically thick disks and we also neglected convection for simplicity. To compute the vertical structure we solve hydrostatic and radiative equilibrium in the vertical direction:

$$\frac{dp}{dz} = -\rho(p,T)\Omega^2 z, \tag{3.19}$$

$$\frac{dT}{dz} = \frac{3\kappa_{\rm R}(\rho,T)}{16\sigma_{\rm B}T^3}\frac{F(z)}{\Omega^2 z}\frac{dp}{dz}. \tag{3.20}$$

The EOS $\rho = \rho(p,T)$ and Rosseland-mean opacity $\kappa_{\rm R}(\rho,T)$ are taken to be the same as those used in our simulations. We assume that the radiative flux is

$$F(z) = \sigma T_{\rm eff,0}^4 \min(1, z/(h_0/2)). \tag{3.21}$$

This is the simplest from of $F(z)$ which satisfies the boundary conditions $F(0) = 0$ and $F(h_0) = \sigma_{\rm B}T_{\rm eff,0}^4$, where h_0 is the photosphere height (the location where the optical depth is 2/3) and $T_{\rm eff,0}$ is the effective temperature.

We integrate the equations from the disk photosphere $z = h_0$ toward the mid-plane $z = 0$ using the boundary condition $T(h_0) = T_{\rm eff,0}$ and $p(h_0) = p(\rho_0, T_{\rm eff,0})$. Here, the free parameters are h_0 and $T_{\rm eff,0}$, with the density at the photosphere ρ_0

determined by the condition that the optical depth down to the photosphere is 2/3: $\kappa_{\rm R}(\rho_0, T_{\rm eff,0})p(\rho_0, T_{\rm eff,0}) = (2/3)\Omega^2 h_0$.

To obtain a thermal equilibrium for a given alpha α_0, we seek the photosphere height h_0 that satisfies the Shakura & Sunyaev (1973) alpha prescription: $(3/2)\Omega\alpha_0 \int_0^{h_0} p(z)dz = \sigma_{\rm B} T_{\rm eff0}^4$. Once h_0 is found, we have equilibrium profiles of pressure $p(z)$, temperature $T(z)$, and density $\rho(z) = \rho(p, T)$ for the specified α_0 and effective temperature $T_{\rm eff0}$, from which we can compute the corresponding surface density as $\Sigma_0 = 2\int_0^{h_0} \rho(z)dz$. Repeating this procedure for different effective temperatures $T_{\rm eff0}$ at various fixed values of α_0, we obtain the surface density as a function of effective temperature $\Sigma_0 = \Sigma_0(T_{\rm eff0}; \alpha_0)$, which is the thermal equilibrium curve for each α_0.

3.6 Parameters

Parameters of the simulations are listed in below in Tables 3.1 and 3.2. As described above, the initial conditions are specified by two parameters, surface density Σ_0 (or equivalently α_0) and effective temperature $T_{\rm eff0}$. The table also lists time-averaged surface density $\bar{\Sigma}$, effective temperature $\bar{T}_{\rm eff}$, and α in the final steady state (the over-bar denotes a time average over a 100 orbit window, from t_1 to t_2 in Table 3.1).

There are also two numerical parameters: the box size and the number of cells. Because we consider dependence on the surface density in this work, it is desirable that the surface density does not change much during the simulation; therefore we adjust the box height so that the mass loss rate through the top/bottom boundaries is less

than about 10 % of the initial mass per hundred orbits, while the MRI is kept resolved reasonably near the disk midplane. Such a box is typically $\sim$ 10 scale heights tall when measured in terms of the final steady-state pressure scale height $h_{\rm p}$ (see Table 3.1 below). In the fiducial runs, which are the ones discussed in Section 4.1, the numbers of cells are $(32, 64, 256)$ and the aspect ratio of the box is $1 : 4 : 8$ in the x, y, and z directions, respectively. See the tables for the absolute size of the box. To check numerical convergence, we have also run a wide box version (the box size in both the x and y directions is doubled) and a high resolution version (the resolution is 1.5 times higher and the box length in each direction is 1.2 times larger) for some selected fiducial runs, which we discuss in Section 4.4.2.

Table 3.1. List of Runs for $R = 1.25 \times 10^{10}$ cm.

run	Σ_0	$T_{\rm eff0}$	α_0	h_0	β_0	$\bar{\Sigma}$	$\bar{T}_{\rm eff}$	α	$\tau_{\rm tot}$	N_x	N_y	N_z	L_x	L_y	L_z	$L_z/h_{\rm p}$	$t_{\rm th}$	t_1	t_2
Upper branch solutions																			
ws0430F	2983	14454	0.0097	1.81e9	100	2900	20617	0.0401	37931	32	64	256	0.500	2.000	4.000	8.37	6.53	50	150
ws0429F	1075	10000	0.0098	1.41e9	100	1030	13352	0.0332	24232	32	64	256	0.500	2.000	4.000	8.54	9.49	90	190
wa0429H	1075	10000	0.0098	1.41e9	100	1070	12570	0.0279	29083	48	96	384	0.600	2.400	4.800	10.4	11.5	90	190
wv0429W	1075	10000	0.0098	1.41e9	100	1052	13067	0.0311	26674	64	128	256	1.000	4.000	4.000	8.58	10.2	20	120
ws0439F	555	7943	0.0099	1.12e9	100	540	10649	0.0325	20337	32	64	256	0.500	2.000	4.000	7.79	10.9	50	150
ws0469F	402	7079	0.0098	9.74e8	100	391	9514	0.0323	19742	32	64	256	0.560	2.240	4.480	8.14	11.6	50	150
wa0469H	402	7079	0.0098	9.74e8	100	400	9463	0.0318	21031	48	96	384	0.672	2.688	5.376	9.75	11.7	50	150
wv0469W	402	7079	0.0098	9.74e8	100	385	9386	0.0328	22161	64	128	256	1.120	4.480	4.480	8.23	11.5	50	150
ws0468C	397	5011	0.0031	7.40e8	100	386	9594	0.0375	22518	32	64	256	0.750	3.000	6.000	8.37	10.2	50	150
ws0491F	342	12882	0.0988	1.27e9	100	332	8992	0.0347	22712	32	64	256	0.500	2.000	4.000	9.77	11.3	50	150
ws0470F	281	12022	0.0991	1.21e9	100	273	9059	0.0452	17420	32	64	256	0.500	2.000	4.000	9.81	8.74	50	150
ws0472C	248	4073	0.0031	5.15e8	100	239	8492	0.0459	23321	32	64	256	1.140	4.560	9.120	10.4	9.06	50	150
ws0471F	247	11481	0.0988	1.18e9	100	238	8853	0.0522	18117	32	64	256	0.500	2.000	4.000	10.0	7.84	50	150
wa0471H	247	11481	0.0988	1.18e9	100	243	8872	0.0496	29032	48	96	384	0.600	2.400	4.800	12.0	8.06	20	120
wv0471W	247	11481	0.0988	1.18e9	100	235	8766	0.0546	23992	64	128	256	1.000	4.000	4.000	10.3	7.69	50	150

Table 3.1 (cont'd)

run	Σ_0	$T_{\rm eff0}$	α_0	h_0	β_0	$\bar{\Sigma}$	$\bar{T}_{\rm eff}$	α	$\tau_{\rm tot}$	N_x	N_y	N_z	L_x	L_y	L_z	$L_z/h_{\rm p}$	$t_{\rm th}$	t_1	t_2
ws0492F	217	10964	0.0986	1.14e9	100	211	8366	0.0548	23980	32	64	256	0.500	2.000	4.000	10.5	7.90	50	150
ws0425F	204	10715	0.0985	1.11e9	100	197	8582	0.0668	20029	32	64	256	0.500	2.000	4.000	10.1	6.48	50	150
ws0427F	191	10471	0.0981	1.09e9	100	185	8482	0.0646	16517	32	64	256	0.500	2.000	4.000	10.0	6.66	50	150
ws0437F	179	10232	0.0975	1.07e9	100	174	8283	0.0651	16791	32	64	256	0.500	2.000	4.000	10.1	6.64	50	150
wa0437H	179	10232	0.0975	1.07e9	100	177	8908	0.0821	14401	48	96	384	0.600	2.400	4.800	11.5	5.17	50	150
wv0437W	179	10232	0.0975	1.07e9	100	168	8333	0.0795	23234	64	128	256	1.000	4.000	4.000	10.6	5.79	50	150
ws0433F	168	10000	0.0978	1.05e9	100	162	8263	0.0749	15595	32	64	256	0.500	2.000	4.000	10.2	5.99	50	150
ws0436F	158	9772	0.0978	1.03e9	100	154	8138	0.0747	17608	32	64	256	0.500	2.000	4.000	10.3	6.05	30	130
wt0487F	149	9549	0.0983	1.00e9	100	143	7914	0.0862	20503	32	64	256	0.500	2.000	4.000	10.6	5.58	50	150
ws0441F	140	9332	0.0981	9.77e8	100	134	7966	0.0927	17556	32	64	256	0.500	2.000	4.000	10.2	5.12	50	150
ws0494C	140	6606	0.0311	7.07e8	10	138	7868	0.0919	23865	32	64	256	0.700	2.800	5.600	10.8	5.29	10	90
ws0446F	132	9120	0.0987	9.51e8	100	127	7490	0.1062	34556	32	64	256	0.500	2.000	4.000	12.0	5.06	50	150
wa0446H	132	9120	0.0987	9.51e8	100	128	7876	0.1087	23795	48	96	384	0.600	2.400	4.800	13.0	4.66	50	150
wz0446W	132	9120	0.0987	9.51e8	10	123	7758	0.1210	28978	64	128	256	1.000	4.000	4.000	11.4	4.35	25	125
wt0442F	118	8709	0.0982	8.97e8	10	113	7522	0.1195	22037	32	64	256	0.500	2.000	4.000	11.4	4.53	50	150
ws0488R	99	8128	0.0982	8.12e8	10	—	—	—	—	32	64	256	0.500	2.000	4.000	—	—	—	—

Table 3.1 (cont'd)

run	Σ_0	$T_{\rm eff0}$	α_0	h_0	β_0	$\bar{\Sigma}$	$\bar{T}_{\rm eff}$	α	$\tau_{\rm tot}$	N_x	N_y	N_z	L_x	L_y	L_z	$L_z/h_{\rm p}$	$t_{\rm th}$	t_1	t_2
Lower branch solutions																			
ws0467R	373	2511	0.0031	1.24e8	100	—	—	—	—	32	64	256	1.000	4.000	8.000	—	—	—	—
ws0466F	353	1584	0.0031	8.18e7	100	348	2675	0.0204	13.2	32	64	256	0.750	3.000	6.000	8.18	17.3	20	100
ws0438F	285	1096	0.0010	1.13e8	100	275	2714	0.0287	8.8	32	64	256	0.500	2.000	4.000	7.70	12.3	50	150
wt0435F	211	1000	0.0010	1.06e8	100	191	2271	0.0271	2.6	32	64	256	0.450	1.800	3.600	7.44	10.9	120	220
ws0462F	176	1778	0.0099	6.51e7	100	174	2283	0.0282	2.4	32	64	256	1.000	4.000	8.000	10.1	9.78	50	150
ws0464C	121	3388	0.0313	1.35e8	100	117	1969	0.0254	2.7	32	64	256	0.500	2.000	4.000	10.9	10.6	50	150
ws0465F	120	2344	0.0314	5.18e7	100	116	2051	0.0312	2.3	32	64	256	1.000	4.000	8.000	8.29	8.89	50	150
ws0434F	100	1513	0.0099	5.85e7	100	93	1885	0.0295	3.2	32	64	256	0.750	3.000	6.000	7.12	9.75	50	150
ws0476F	49	1698	0.0315	5.28e7	100	45	1560	0.0314	5.4	32	64	256	0.800	3.200	6.400	7.34	9.02	50	150
ws0445F	32	1096	0.0098	8.63e7	100	31	1515	0.0418	4.4	32	64	256	0.500	2.000	4.000	7.52	6.66	50	150

Note. — The last letters in the names of runs denote the following: F = fiducial run, H = high resolution run, W = wide box run, R = runaway heating/cooling run, and C = run to check dependence on the initial condition. The units of surface densities (Σ_0 and $\bar{\Sigma}$), effective temperatures ($T_{\rm eff0}$ and $\bar{T}_{\rm eff}$), height (h_0), and thermal time ($t_{\rm th}$) are, respectively, g cm^{-2}, K, cm, and orbit. L_x, L_y, and L_z are the lengths given in units of h_0, and N_x, N_y, and N_z are the numbers of cells, in the x, y, and in z directions, respectively. The time-averaging in diagnostics is done for $t_1 < t < t_2$ orbits. The pressure scale height of the steady state is computed as $h_{\rm p} \equiv \int [\langle P_{\rm therm} \rangle]\, dz/2 \max([\langle P_{\rm therm} \rangle])$. These runs were first published in Hirose et al. (2014).

Table 3.2. List of Runs for Additional Radii.

$T_{\rm eff}$	Σ	α	$\tau_{\rm tot}$	$T_{\rm eff,0}$	Σ_0	α_0	β_0	$h_0/10^8$	N_x	N_y	N_z	L_x/h_0	L_y/h_0	L_z/h_0	L_z/h_P	$t_{\rm th}$	$t_{\rm max}$
$R = 1.25\times10^9$ cm																	
8932	10.7	0.090	5876	8709	10.9	0.042	10	0.226	32	64	384	0.50	2.00	6.00	15.2	13.8	189
9427	12.2	0.068	4910	7943	12.5	0.026	10	0.210	32	64	384	0.50	2.00	6.00	11.5	17.1	114
9698	14.7	0.055	5162	7943	14.9	0.020	10	0.221	32	64	384	0.50	2.00	6.00	10.9	19.7	118
17405	85.8	0.037	6985	16218	86.4	0.026	100	0.447	32	64	512	0.50	2.00	6.00	13.4	24.4	133
19471	106	0.042	6798	16218	107	0.020	10	0.462	32	64	512	0.50	2.00	6.00	13.0	20.9	139
$R = 4.13\times10^9$ cm																	
7546	36.7	0.134	17221	8709	37.2	0.067	10	1.55	32	64	384	0.50	2.00	6.00	22.7	11.0	165
8079	40.4	0.099	16800	9549	40.6	0.081	10	1.71	32	64	384	0.50	2.00	6.00	19.9	12.8	114
8542	45.2	0.076	14139	9549	45.5	0.070	10	1.75	32	64	384	0.50	2.00	6.00	16.4	15.1	122
9324	52.0	0.069	9283	9549	52.5	0.058	10	1.80	32	64	384	0.50	2.00	6.00	13.9	15.9	123

Note. — $T_{\rm eff}$, Σ, α, and $\tau_{\rm tot}$ are the time averaged effective temperature in K, column mass density in g cm^{-2}, Shakura & Sunyaev (1973) α-parameter, and optical depth respectively. $T_{\rm eff,0}$, Σ_0, α_0, and β_0 are the initial condition values where β_0 is the initial ratio of gas to magnetic pressure. $h_0/10^8$ is the simulation length unit over 10^8 cm. N_x, N_y, N_z are the number of grid cells in the x, y, and z directions respectively. L_x/h_0, L_y/h_0, L_z/h_0 are dimensions of the simulation domain in the x, y, and z directions respectively. L_z/h_P is the height of the simulation domain over the time averaged pressure scale height. $t_{\rm th}$ is the time averaged thermal time. $t_{\rm max}$ is the maximum runtime used for time averaging. These runs were first published in Coleman et al. (2016).

Chapter 4

Discovery of Convective Disks

Here we present the radiation MHD simulations that first appeared in Hirose et al. (2014)[1]. These simulations incorporate vertical stratification and realistic thermodynamics which consists of EOS and opacity tables that accurately portray the regime of hydrogen ionization that is fundamental to DNe. For further simulation details see Chapter 3. The thermal equilibrium of each simulation is determined by a balance between local turbulent dissipation and cooling, mostly in the form of radiative diffusion (calculated from a solution of the radiative transfer problem) and hydrodynamic convection which is directly simulated. We limit our analysis to the case of zero net vertical magnetic field, which results in the lowest values of α. To focus on the the effects of our thermodynamics we assume ideal MHD. While this is reasonable for the outburst phase of DNe, non-ideal effects will likely be important for quiescence in which hydrogen

[1]This chapter is an abridged version of Hirose et al. (2014) and we encourage the interested reader to consult it for more details.

is mostly neutral (Gammie & Menou, 1998; Sano & Stone, 2002, 2003; Kunz & Lesur, 2013; Coleman et al., 2016, see also Section 7.3). These simulations corroborate the existence of two distinct stable branches of thermal equilibria as inferred by the DIM. These branches correspond to the hot ionized outburst branch and the cool neutral quiescent branch.

4.1 Thermal Equilibria

One way to characterize the results of thermal equilibria is in terms of the effective temperature at the disk photosphere. Fig. 4.1 shows this quantity as a function of surface density for equilibrium states that last over 100 orbits.[2] The time-averaged effective temperature and surface density are computed as

$$\bar{T}_{\rm eff} \equiv \left[\left(\frac{1}{2\sigma_{\rm B}} \int \left\langle Q^- \right\rangle dz \right)^{\frac{1}{4}} \right], \tag{4.1}$$

$$\bar{\Sigma} \equiv \left[\int \langle \rho \rangle \, dz \right], \tag{4.2}$$

where $\langle Q^- \rangle$ is the total cooling rate,

$$\left\langle Q^- \right\rangle \equiv \frac{d}{dz} \langle F_z \rangle + \frac{d}{dz} \langle (e+E) v_z \rangle \, . \tag{4.3}$$

[2]The solution at the right edge of the lower branch (ws0466F) is an exception; see Section 4.4.1 for details.

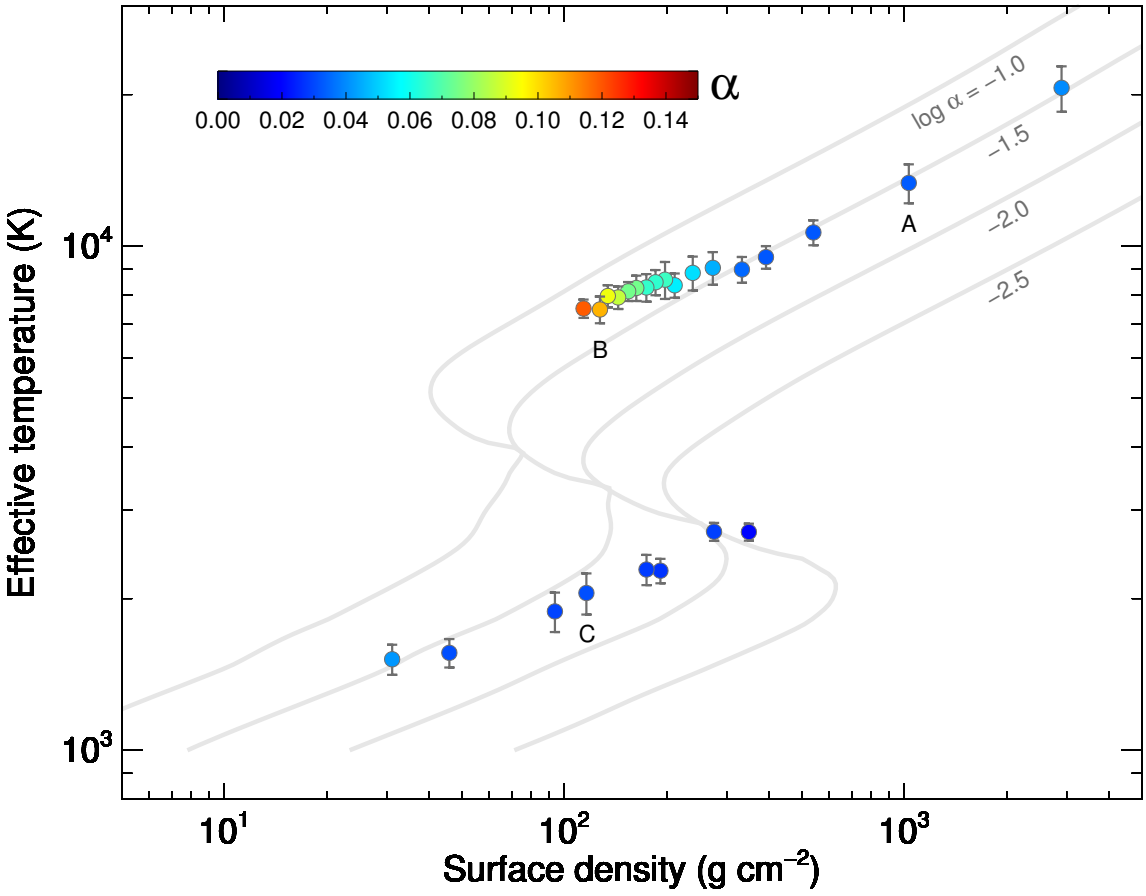

Figure 4.1 Time-averaged effective temperature $\bar{T}_{\rm eff}$ vs. surface density $\bar{\Sigma}$ in thermal equilibrium states. Error bars represent one standard deviation in the time variability of effective temperature $T_{\rm eff}(t) \equiv \left(\int \langle Q^- \rangle \, dz / 2\sigma_{\rm B}\right)^{1/4}$. Colors represent the time-averaged values of α. Gray curves are thermal equilibria produced by a DIM based on the alpha prescription. Solutions labeled with A, B, and C correspond to panels A, B, and C, respectively in Fig. 4.2.

The brackets [ ] here denote time averaging over a selected period of 100 orbits in which the disk is in quasi-steady state and the MRI in the disk is fairly resolved (the period of time averaging in each run is listed in Table 3.1), and the space integration is done for the full extent of the box in z. Additionally, the angular brackets $\langle\rangle$ denotes the vertical profile, for example $\langle f \rangle$ is computed as

$$\langle f \rangle (z,t) \equiv \frac{\iint f(x,y,z,t) dxdy}{\iint dxdy}, \tag{4.4}$$

where the integrations are done over the full extent of the simulation domain in the x and y directions. The surface density can vary due to the mass loss through the vertical boundaries, and thus the time averaged surface density $\bar{\Sigma}$ is typically smaller than the initial surface density Σ_0 by only a few percent, rising to at most 9 % (see Table 3.1).

The DIM based on the α prescription for the stress generally produce S-shaped thermal equilibrium curves in the $T_{\rm eff}$-Σ plane, as illustrated by the gray curves. Our simulations show that "S-curves" can also arise as a result of MRI turbulence at temperatures near the hydrogen ionization transition as reported by Latter & Papaloizou (2012). There are two major solution branches: the upper, hot, outburst branch ($\bar{T}_{\rm eff} \gtrsim 8000$ K, $\bar{\Sigma} \gtrsim 100$ g cm^{-2}) and the lower, cool, quiescent branch ($\bar{T}_{\rm eff} \lesssim 3000$ K, $\bar{\Sigma} \lesssim 300$ g cm^{-2}). For a limited range of surface density ($100 \lesssim \bar{\Sigma} \lesssim 300$ g cm^{-2}), there exist two different stable states for a single value of surface density, showing bistability. The disk is almost fully ionized and optically thick (with total optical depth $\tau_{\rm tot} > 10^4$) on the upper branch, but it is almost wholly neutral and much less optically thick ($2 < \tau_{\rm tot} < 14$) on the lower

branch. (See Table 3.1 for the value of $\tau_{\rm tot}$ in each run.) These features of the upper and lower branches are consistent with the DIM.

4.2 Enhancement of α

A new finding here is that α is not constant, as shown by the colors in Fig. 4.1. To be precise, we define α as

$$\alpha \equiv \frac{[W_{xy}]}{\left[\int P_{\rm therm}\,{\rm d}z\right]}, \tag{4.5}$$

where the vertically-integrated total stress W_{xy} is defined as

$$W_{xy}(t) \equiv \int \langle w_{xy}\rangle\,{\rm d}z. \tag{4.6}$$

Here $P_{\rm therm} \equiv P_{\rm gas} + E/3$ and $w_{xy} \equiv -B_x B_y + \rho v_x \delta v_y$, where $\delta v_y \equiv v_y + (3/2)\Omega x$. (We include radiation pressure $E/3$ in the thermal pressure, but its fraction is at most 0.057 in the largest surface density case on the upper branch.) Changing the definition of α to a time-average of the instantaneous ratio, $\left[W_{xy}/\int P_{\rm therm}\,{\rm d}z\right]$, changes the values by typically a few percent, and always less than 10 % for those simulations achieving a quasi-steady state.

Throughout the lower branch and for $T_{\rm eff} \gtrsim 10^4$ K on the upper branch, α is approximately 0.03, typical of values found previously in local numerical simulations of MRI turbulence that lack net vertical magnetic flux. However, near the left edge of the upper

branch ($7000 \lesssim T_{\rm eff} \lesssim 10000$ K), α rises to as much as 0.12, increasing as the surface density decreases. This behavior is in contrast with the DIM, where constant values of α are assumed on each branch: ~ 0.1 on the upper branch and ~ 0.01 on the lower branch (see Section 4.4.3). As shown below, vertical profiles of the energy transport reveal that the notable change in α in our simulations is associated with hydrodynamic convection.

In Fig. 4.2, time-averaged profiles of radiative heat flux $\bar{F}^{-}_{\rm rad}(z)$, advective heat flux $\bar{F}^{-}_{\rm adv}(z)$, and cumulative heating rate $\bar{F}^{+}_{\rm heat}(z)$ are shown for three selected runs: ws0429F, ws0446F, and ws0465F. Here, the heat fluxes are defined as

$$\bar{F}^{-}_{\rm rad}(z) \equiv \left[\langle F_z \rangle\right], \tag{4.7}$$

$$\bar{F}^{-}_{\rm adv}(z) \equiv \left[\langle (e+E) v_z \rangle\right], \tag{4.8}$$

$$\bar{F}^{+}_{\rm heat}(z) \equiv \int_0^z \left[\langle Q_{\rm diss} \rangle + \langle -\left(\nabla \cdot \boldsymbol{v}\right) P \rangle + \langle -\nabla \boldsymbol{v} : \mathsf{P} \rangle\right] dz. \tag{4.9}$$

From the energy equations (3.13) and (3.14), the thermal energy balance in a steady state is written as

$$Q_{\rm diss} - \left(\nabla \cdot \boldsymbol{v}\right) P - \nabla \boldsymbol{v} : \mathsf{P} = \nabla \cdot \boldsymbol{F} + \nabla \cdot \left((e+E)\boldsymbol{v}\right), \tag{4.10}$$

where the left hand side is the heating rate (turbulent dissipation and compressional heating) while the right hand side is the cooling rate (radiative diffusion and advection).

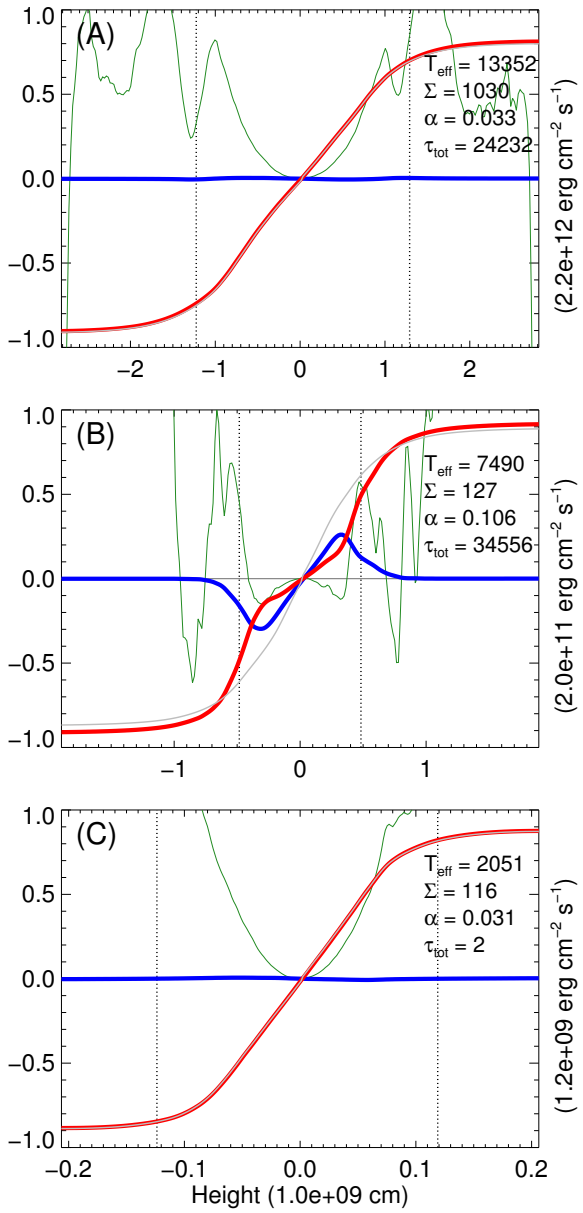

Figure 4.2 Time-averaged vertical profiles of radiative heat flux $\bar{F}^{-}_{\rm rad}$ (red), advective heat flux $\bar{F}^{-}_{\rm adv}$ (blue), and cumulative heating rate $\bar{F}^{+}_{\rm heat}$ (gray), normalized by the value shown on the right axis in each panel, for two upper branch simulations, (A) $\Sigma_0 = 1075$ g cm^{-2} (ws0429F) and (B) $\Sigma_0 = 132$ g cm^{-2} (ws0446F), and one lower branch simulation, (C) $\Sigma_0 = 120$ g cm^{-2} (ws0465F). The green curves show N^2/Ω^2, where N is the hydrodynamic Brunt-Väisälä frequency. The plasma β is larger than unity at the heights between the two vertical dotted lines. Also, in each frame, the corresponding values of $\bar{T}_{\rm eff}$ (K), $\bar{\Sigma}$ (g cm^{-3}), α, and the total optical depth $\tau_{\rm tot}$ are shown.

Therefore, it is expected in Fig. 4.2 that

$$\bar{F}^{+}_{\rm heat}(z) = \bar{F}^{-}_{\rm rad}(z) + \bar{F}^{-}_{\rm adv}(z), \tag{4.11}$$

which is a vertically-integrated form of equation (4.10). Actually, the equation (4.11) roughly holds in panel B, and almost exactly holds in panels A and C. (Note that the gray curve ($\bar{F}^{+}_{\rm heat}$) almost matches the red curve ($\bar{F}^{-}_{\rm rad}$) in panels A and C.)

When radiative diffusion is the predominant flux transporting the dissipated turbulent energy to the disk surface (Figs. 4.2A and 4.2C), the value of α is consistent with previous typical values generated by MRI turbulence. On the other hand, when advection plays a major role in the vertical heat transport near the disk midplane (Fig. 4.2B), α is large. As shown in the next subsection, this advective heat transport is associated with hydrodynamic convection, and it is triggered by high opacity that suppresses heat transport by radiative diffusion. We therefore refer to this advective heat transport as *convection* from now on. The energy transported upward by convection is deposited at higher altitude, but below the photosphere, and is then carried by radiative diffusion toward the disk surface.

As shown in Figs. 4.3A and 4.3B, the left edge of the upper branch, where α is large, is exactly the place where convection carries much of the heat flux. Here, to measure the convection strength, we define the advective fraction as the ratio of the advective energy

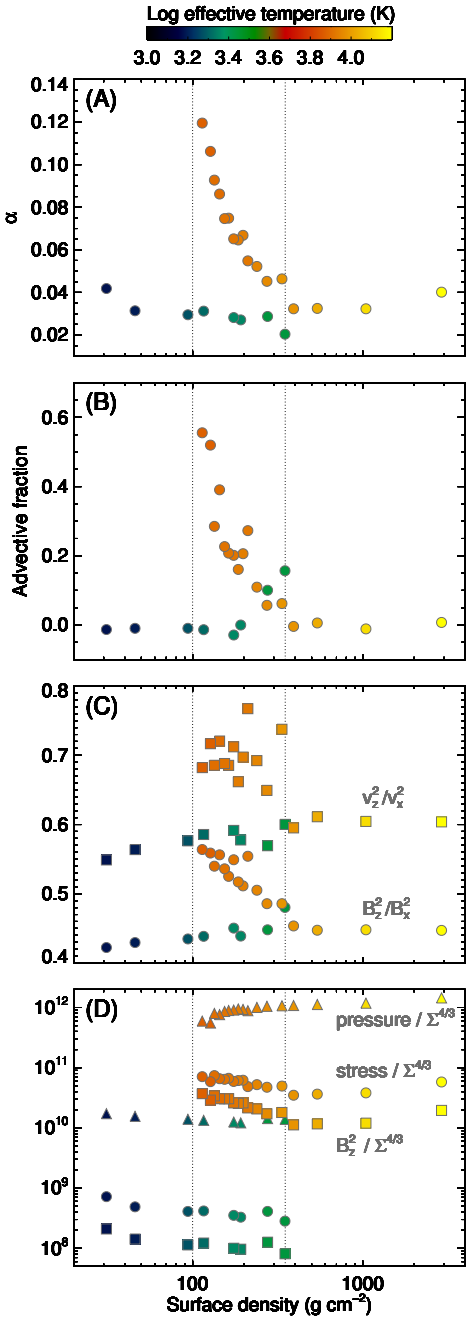

Figure 4.3 Various time-averaged quantities as a function of the surface density $\bar{\Sigma}$: (A) α, (B) advective fraction $f_{\rm conv}$, (C) ratios of the vertical to the radial components for velocity field $f_{\rm vel}$ (squares) and for magnetic field $f_{\rm mag}$ (circles), (D) vertically-integrated square of vertical magnetic field $\left[\int \langle B_z^2 \rangle \, dz\right]$ (squares), total stress $[W_{xy}]$ (circles), and thermal pressure $[P_{\rm therm}]$ (triangles), each divided by $\bar{\Sigma}^{4/3}$. Colors represent the time-averaged effective temperature $\bar{T}_{\rm eff}$ in each simulation. The two vertical dotted lines indicate the surface density range $100 \lesssim \bar{\Sigma} \lesssim 350$ (g cm^{-2}), where convection acts on the upper branch.

flux to the total energy flux,

$$f_{\rm conv} \equiv \frac{\int \left[\langle (e+E)\, v_z \rangle\right] {\rm sign}(z) \left[\langle P_{\rm therm} \rangle\right] dz}{\int \left[\langle (e+E)\, v_z \rangle + \langle F_z \rangle\right] {\rm sign}(z) \left[\langle P_{\rm therm} \rangle\right] dz}, \tag{4.12}$$

where the time-averaged pressure $[\langle P_{\rm therm} \rangle]$ is used as a weight function to emphasize the regions within the disk photospheres.[3] The figures also show that α has a strong correlation with the advective fraction, which increases as the surface density (and temperature) decrease on the upper branch, although Hirose (2015) found that the Mach number of the convective flow is better correlated with α. The reason for this trend of advective fraction is that much of the opacity on the upper branch is due to free-free absorption (i.e., Kramers opacity) and rises rapidly with falling temperature ($\propto T^{-7/2}$), driving stronger convection.

The reason why α is enhanced when hydrodynamic convection exists can be understood as follows. Convection drives vertical gas motions, which can create more vertical magnetic field than in the usual MRI turbulence. This assertion is supported by Fig. 4.3C, which shows that MRI turbulence is modified when convection exists so as to increase the time-averaged ratios of the vertical to the radial components for both velocity

[3]The advective fraction can be negative; when it is, energy is transported toward the midplane by advection and deposited there.

and magnetic field. Here the ratios are computed as

$$f_{\rm mag} \equiv \frac{\int \left[\langle B_z^2 \rangle\right] \left[\langle P_{\rm therm} \rangle\right] dz}{\int \left[\langle B_x^2 \rangle\right] \left[\langle P_{\rm therm} \rangle\right] dz}, \tag{4.13}$$

$$f_{\rm vel} \equiv \frac{\int \left[\langle v_z^2 \rangle\right] \left[\langle P_{\rm therm} \rangle\right] dz}{\int \left[\langle v_x^2 \rangle\right] \left[\langle P_{\rm therm} \rangle\right] dz}. \tag{4.14}$$

The strengthened vertical magnetic field enhances the magnetic stresses since it is the seed for the most powerful, axisymmetric, modes of the MRI. Indeed, when convection acts, time-averaged and vertically-integrated stress $[W_{xy}]$ and the squared vertical magnetic field $\left[\int \langle B_z^2 \rangle \, dz\right]$ scale in proportion to one another, both deviating upwards from the trend ($\propto \bar{\Sigma}^{4/3}$) seen in the non-convective cases (Fig. 4.3D). (The ratio of Reynolds stress to Maxwell stress hardly changes with $\bar{\Sigma}$ and is always ~ 0.23.) In contrast, the integrated pressure $\left[\int P_{\rm therm} \, {\rm d}z\right]$ has a slightly decreasing trend when convection is strong. Apparently, the cooling due to convection lowers the time-averaged equilibrium pressure from the standard trend line despite the increased magnetic stress. Therefore, α, the ratio of stress to pressure, increases when convection is stronger.

4.3 Hydrodynamic Convection

4.3.1 Evidence for True Thermal Convection

In Fig. 4.2, we plot the profiles of the squared hydrodynamic Brunt-Väisälä frequency,

$$\frac{N^2}{\Omega^2} \equiv \frac{1}{[\langle \Gamma_1 \rangle]} \frac{d \ln [\langle P \rangle]}{d \ln z} - \frac{d \ln [\langle \rho \rangle]}{d \ln z}, \tag{4.15}$$

where $\Gamma_1 \equiv (\partial \ln P / \partial \ln \rho)_s$ is the generalized adiabatic index and s is the specific entropy. Note that this hydrodynamic expression of buoyancy frequency is only valid where thermal pressure dominates magnetic pressure, i.e. the plasma β is larger than unity, which is interior to the two vertical dotted lines shown in the figure.

In solution (B), N^2 is negative in the midplane regions, precisely where the advective heat transport $\bar{F}^{-}_{\rm adv}(z)$ is substantial, indicating that the advective heat transport in the upper branch discussed in the previous subsection is really thermal convection associated with unstable hydrodynamical modes. We provide additional direct evidence that this is true hydrodynamic convection in the next subsection. Note that the large negative values of N^2 indicate that convection does not cause the time-averaged temperature gradient to be close to the adiabatic value, as supposedly happens in convection zones in stars. In fact, we have measured Mach numbers in the convective velocities as high as 0.1 in this simulation. Such superadiabatic gradients are also observed in MRI simulations with vertical convection by Bodo et al. (2013).

Apart from the case just mentioned, N^2 is generally positive, indicating convective

stability, provided that $\beta > 1$. On the other hand, in solution (B), N^2 is negative in some regions where $\beta < 1$, which, however, does not mean that they are convectively unstable. Because magnetic pressure supports the plasma rather than thermal pressure alone, the hydrodynamic Brunt-Väisälä frequency is not the relevant quantity for buoyancy instabilities there. Rather, Parker instabilities can in general act in these regions (Blaes et al., 2007).

Two solutions near the right edge of the lower branch (ws0438F and ws0466F) also show a nonzero advective fraction (Fig. 4.3B), but do not have an enhanced α (Fig. 4.3A). We have confirmed that N^2 is negative where advective heat transport is observed in these simulations. However, the convection in these solutions is too weak to strengthen the vertical magnetic field, with convective Mach numbers that are two orders of magnitude smaller than on the upper branch.

4.3.2 Convective/Radiative Limit Cycle

So far we have been discussing trends in the time-averages of the simulations. However, in a given simulation, convection is often intermittent, and the system traverses limit-cycles, switching convection on and off episodically. These limit-cycles are traversed on roughly a thermal timescale.[4] In contrast, the dwarf-nova limit cycles, are a separate phenomenon and take much longer, of order an inflow timescale because they require changes in the local surface density.

An example of a convective/radiative limit cycle is seen in Fig. 4.4, where time vari-

[4]The thermal time for each run, computed as $t_{\rm th} \equiv \int \langle e + E \rangle \, dz / \int \langle Q^+ \rangle \, dz$, is listed in Table 3.1.

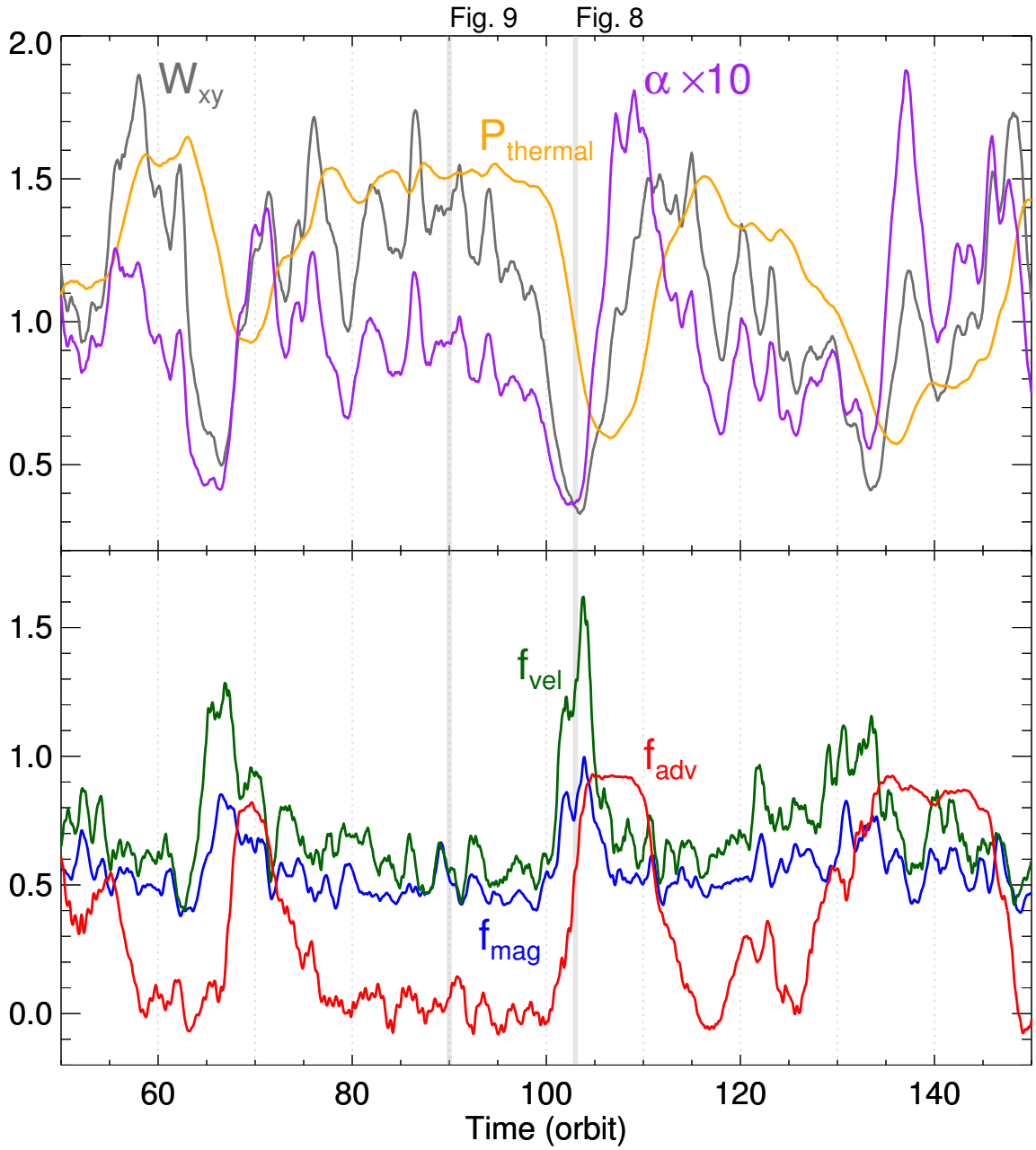

Figure 4.4 Time variations of various quantities for $\Sigma_0 = 140$ g cm^{-2} on the upper branch (ws0441F). Upper panel: Vertically-integrated total stress $\tilde{W}_{xy}$ (gray) and thermal pressure $\tilde{P}_{\rm thermal}$ (orange), and $\tilde{\alpha} \times 10$ (purple). The total stress and thermal pressure are normalized arbitrarily here. Lower panel: Advective fraction $\tilde{f}_{\rm conv}$ (red), and the ratios of the vertical to the radial components of velocity field $\tilde{f}_{\rm vel}$ (green) and magnetic field $\tilde{f}_{\rm mag}$ (blue). Hirose et al. (2014) explore the times denoted by the two vertical gray lines in further detail (see Figs. 8 and 9. of Hirose et al., 2014)

ations of the vertically-integrated pressure $\tilde{P}_{\rm thermal}(t) \equiv \{P_{\rm therm}\}$, stress $\tilde{W}_{xy}(t) \equiv \{W_{xy}\}$ and instantaneous advective fraction $\tilde{f}_{\rm conv}(t)$ defined as

$$\tilde{f}_{\rm conv}(t) \equiv \left\{ \frac{\int \{\langle (e+E)\, v_z \rangle\}\, {\rm sign}(z)\, \langle P_{\rm therm} \rangle\, dz}{\int \{\langle (e+E)\, v_z + F_z \rangle\}\, {\rm sign}(z)\, \langle P_{\rm therm} \rangle\, dz} \right\} \tag{4.16}$$

are shown for $\Sigma_0 = 140$ g cm^{-2} on the upper branch (ws0441F). Here the brackets { } denote box-car smoothing over a width of one orbit. Also shown are the instantaneous α and ratios of the vertical to the radial components for velocity and magnetic fields defined as

$$\tilde{\alpha}(t) \equiv \frac{\tilde{W}_{xy}(t)}{\tilde{P}_{\rm thermal}(t)}, \tag{4.17}$$

$$\tilde{f}_{\rm mag}(t) \equiv \left\{ \frac{\int \langle B_z^2 \rangle\, \langle P_{\rm therm} \rangle\, dz}{\int \langle B_x^2 \rangle\, \langle P_{\rm therm} \rangle\, dz} \right\}, \tag{4.18}$$

$$\tilde{f}_{\rm vel}(t) \equiv \left\{ \frac{\int \langle v_z^2 \rangle\, \langle P_{\rm therm} \rangle\, dz}{\int \langle v_x^2 \rangle\, \langle P_{\rm therm} \rangle\, dz} \right\}. \tag{4.19}$$

The curve of advective fraction demonstrates that convection occurs episodically, anti-correlated with the variation of pressure, indicating that convection is controlled by the temperature-sensitive opacity. The figure also shows that the ratios $\tilde{f}_{\rm mag}(t)$ and $\tilde{f}_{\rm vel}(t)$, whose time-averaged versions are enhanced when convection acts as discussed above, are actually enhanced at the beginning of each of the convective episodes. We interpret this as being due to the generation of vertical magnetic field by the onset of vertical convection, which seeds the axisymmetric MRI. The vertical to radial magnetic field ratio then falls back to the usual value as horizontal field is built by the MHD turbulence. The figure

also shows that the stress begins to increase when the convection is fully developed and is followed by pressure with a finite time lag of several orbits. The stress parameter α, which is already higher than that of normal MRI turbulence, is further amplified when stress is high while pressure is low.

We further confirm that hydrodynamic convection is actually operating during what we are calling the convective periods by noting that the specific entropy falls off with distance from the midplane, (i.e. a super adiabatic gradient). This drives low-density and high-temperature plumes that coherently transport heat upward. We therefore expect coherent vertical magnetic fields will be generated on the scale of the convective plumes, which is about half the pressure scale height.[5] Note that strong isolated magnetic fluxes are also associated with low density blobs, which suggests that the finite amplitude, slow mode buoyancy mechanism (Blaes et al., 2011) also contributes to vertical advection of heat. However, it is now completely dominated by the genuine hydrodynamic convection that fills much of the volume. These features in a convective period are contrasted with those in a radiative period. The vertical gradient of specific entropy is now almost zero, indicating that the disk is convectively neutrally stable. This adiabatic gradient is caused by convection in the preceding convective period. Also, we see mostly random motions and only the slow mode mechanism is operating for the small net vertical advection of heat; however, the main heat transport mechanism here is, of course, radiative diffusion ($\tilde{f}_{\rm conv} \sim 0$).

It might be instructive to visualize the convective/radiative limit cycles as trajectories

[5]See Table 3.1 for the pressure scale height in each run.

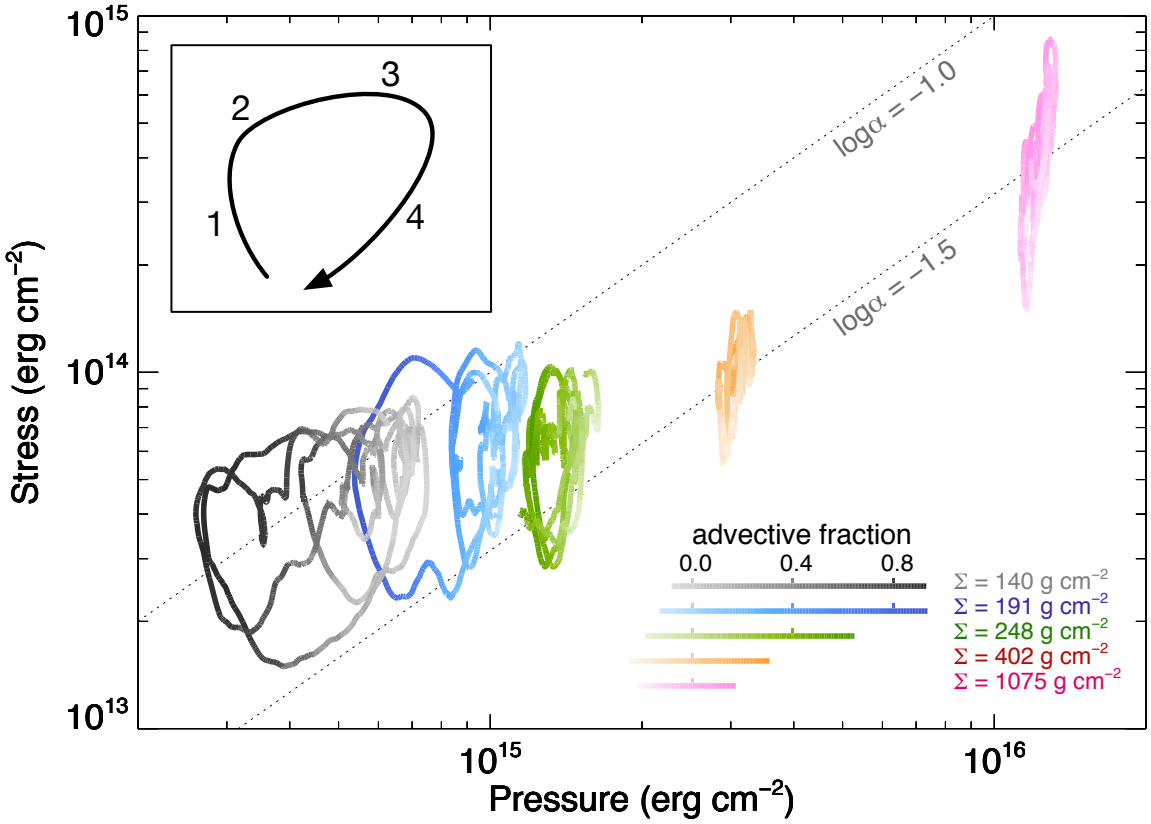

Figure 4.5 Trajectories in the plane of vertically-integrated pressure $\tilde{P}_{\rm thermal}(t)$ vs. stress $\tilde{W}_{xy}(t)$ for selected simulations on the upper branch ($\Sigma_0 = 140$ (ws0441F), 191 (ws0427F), 248 (ws0472F), 402 (ws0469F), and 1075 g cm^{-2} (ws0429F)) indicated by different colors. The color intensity represents the advective fraction $\tilde{f}_{\rm conv}$. The dotted lines are contours of $\alpha = 0.1$ and 0.03. The insert at the upper left shows a schematic picture of the limit-cycle described in the text.

in the pressure vs. stress plane. Fig. 4.5 shows such trajectories for $\Sigma_0 = 140$ (ws0441F), which we discussed above, as well as $\Sigma_0 = 191$ (ws0427F), 248 (ws0472F), 402 (ws0469F), and 1075 g cm^{-2} (ws0429F) on the upper branch, in terms of the time variation of the vertically-integrated pressure $\tilde{P}_{\rm thermal}(t)$ and stress $\tilde{W}_{xy}(t)$. The range of time is $t_1 < t < t_2$, where t_1 and t_2 are given in Table 3.1. The color intensity represents the instantaneous advective fraction $\tilde{f}_{\rm conv}(t)$. When the surface density is higher and convection is not present ($\Sigma_0 = 402$ and 1075 g cm^{-2}), no limit cycle is seen, as pressure is almost unchanged in the face of stress fluctuations and thus the trajectories are almost vertical. As the surface density decreases ($\Sigma_0 = 248$, 191 and 140 g cm^{-2}), the pressure fluctuation becomes larger and a limit cycle running clockwise in the plane is established: (1) magnetic stress is strengthened in fully-developed convection, (2) stronger magnetic turbulence leads to greater dissipation, which increases the temperature and therefore the pressure; (3) higher temperature reduces the opacity, suppressing convection, and (4) without convection, magnetic fields weaken and the temperature declines, increasing the opacity, which eventually restores convection. On the left edge of the trajectories in the lower surface density (convective) cases, stress increases while pressure stays low; this phase lag further increases α as we discussed above.

4.4 Discussion

4.4.1 Runaway Heating and Cooling

We always find runaway cooling (heating) of the disk beyond the left (right) edge of the upper (lower) branch, respectively, for example ws0488R showing runaway cooling and ws0467R showing runaway heating (for trajectories on the S-curve see Fig. 12 of Hirose et al., 2014). The initial development of MRI turbulence in both runs was similar to that in the other runs. However, both runs passed by the edge of the nearest stable branch and did not reach a steady state, which indicates that the two stable branches are actually truncated there. These facts indicate that any limit cycle in this plane runs anti-clockwise, which is consistent with the DIMs, where the cooling rate (heating rate) always exceeds the heating rate (cooling rate) beyond the left (right) edge of the upper (lower) branch, respectively. In fact, signs of the thermal runaway for the state transitions are seen near the edges of the branches. For example, the disk at the right edge of the lower branch (ws0466F) stayed in thermal equilibrium for ~ 80 orbits and then began to flare up; on the other hand, the disk at the left edge of the upper branch (wt0442F) began to collapse after thermal equilibrium of ~ 100 orbits. Similar behavior at the edges of the two stable branches was reported by Latter & Papaloizou (2012).

Run ws0488R was stopped at $t \sim 50$ orbits since the disk collapsed and the MRI near the disk midplane became significantly under-resolved. Run ws0467R was also stopped at $t \sim 100$ orbits when the mass loss from the simulation box became substantial ($\sim 25\%$).

The runs near the edges of the branches (ws0466F and wt0442F) were also stopped for the same reasons. To further simulate the thermal runaways or state transitions between the upper and lower branches, we would need to dynamically change the box size so that the MRI is always well resolved and the mass loss is kept small enough.

We could not find long-lived equilibria between the upper and lower branches, suggesting that the negative sloped portions of the alpha-based S-curves are unstable. In fact, in a few fiducial runs we found equilibria that lasted more than several tens of orbits, but these were not fully reproduced when the box size or the resolution was changed.

4.4.2 Numerical Robustness of the Results

To check the robustness of our results, we performed two kinds of tests; one to check dependence on the initial conditions and the other to check numerical convergence[6]. For four arbitrarily selected fiducial runs, we ran companion simulations with similar, albeit, different initial conditions. The final states of paired runs are roughly the same both in effective temperature and α, which confirms that the two branches are actually unique attractors.

We also arbitrarily selected five fiducial runs on the upper branch, and for each we ran two supplementary simulations: doubling the horizontal box size in one, and increasing the resolution by 1.5 times and the box size by 1.2 times in the other one. The final states of the fiducial run and the corresponding two supplementary runs are roughly the same, both in effective temperature and α for all five cases. We may therefore conclude

[6]For additional details of these robustness tests see Section 4.2 of Hirose et al. (2014).

that our two main results, the thermal equilibrium curve and the high α near the edge of the upper branch, are not sensitive to the box size or the resolution.

4.4.3 Comparison with the DIM Model

As shown in Fig. 4.1, those simulations that do not exhibit convection lie on our DIM-model curve with fixed $\alpha = 0.03$ on the upper branch, while they are slightly below the curve on the lower branch (cf. Latter & Papaloizou, 2012). We suspect that the discrepancy may come from our DIM's assumption that the disk is very optically thick even on the lower branch, where the measured optical depth in the simulations can be as low as 2.3 (Table 1).

On the other hand, our results near the left edge of the upper branch deviate upwards from the fixed α curve as α increases due to convection. In some cases, however, our results with larger values of α lie below a DIM-model curve computed assuming a smaller α. Also, the minimum (maximum) surface density of our upper (lower) branch, respectively, are larger than those of the relevant DIM-model curve. These discrepancies are presumably due to our neglect of convection in computing the DIM curves because convection tends to increase the critical surface densities (see, for example, Pojmański, 1986).

4.4.4 Effect of the Initially Imposed Net Toroidal Flux

It is widely known that the saturation of MRI turbulence in the local shearing box depends on the net vertical flux or net toroidal flux threading it (see, for example, Hawley et al., 1995; Latter & Papaloizou, 2012). Although we do not impose a net vertical flux in the box, we do impose a net toroidal flux initially in the box (see Section 3.5). Therefore one might argue that the saturation of MRI turbulence in our simulations could be affected by the initial net toroidal flux.

Stratified shearing box simulations, however, generally do not retain a net toroidal flux because of buoyant escape through the vertical boundaries. The net toroidal flux in our simulations fluctuates significantly in time, flipping in sign, and there is no indication of any memory of the initial net toroidal flux. (The reason for the sign flips is presumably that azimuthal flux arises from shear of radial flux, which also flips sign over time due to the still poorly understood dynamo of stratified MRI turbulence.) Therefore, we conclude that the saturation of MRI turbulence in our simulations is independent of the initially imposed toroidal flux.

4.4.5 Alternative Explanations for Large α in Outburst

We have shown that convection enhances MRI turbulent stress, which can increase α above 0.1. Since convection necessarily occurs in the outburst phase due to the strong temperature dependence of opacity, we have found an α-enhancement mechanism that is due to the internal physics within the disk in this regime.

There are other external mechanisms, however, that might be considered candidates for producing enhanced α. For example, it is well-known that imposition of net vertical magnetic flux raises the saturation level of the turbulence. However, it is also known that the dependency of stress on net vertical field $B_{z\mathrm{net}}$ is fairly strong, $\propto {B_{z\mathrm{net}}}^2$ (Suzuki et al., 2010; Okuzumi & Hirose, 2011). Therefore, the fact that the observed α in the outburst phase is always of order 0.1 is a strong constraint on the existence of a global net vertical field in the disk in the outburst phase (King et al., 2007). On the other hand, global simulations of MRI turbulent disks have produced local net vertical fluxes through magnetic linkages in the disk corona (Sorathia et al., 2010). It could be that this mechanism might play a role in producing large α's in the outburst phase, but why this would only occur in the outburst phase is unclear. Sorathia et al. (2012) have also suggested that the large α's inferred in the outburst phase may be due to transient periods of magnetic field growth in the jump to outburst, together with gradients in the global disk. For these and many other reasons, thermodynamically consistent, global MRI simulations of disks in the hydrogen ionizing regime will be of great interest (see also Section 7.2).

Another point worth mentioning is that an enhanced stress does not necessarily lead to an enhanced α. If, for example, pressure also rises in proportion to the enhanced stress (via enhanced dissipation), α, the ratio of stress to pressure, would not be increased. In our simulations, the convective cooling controls the pressure well enough to lead to an increase in α. Net vertical flux, which increases stress, could in principle also explain

the high α in the high state, but whether it does or not will depend on the scaling of cooling rate with pressure in the presence of vertical flux. New simulations that carefully account for thermodynamics will be necessary to determine this scaling.

4.4.6 Relation to the Radiation Pressure Dominated Thermal Instability

We have remarked on the possible thermal instability of the S-curve branch that should link the low and high states. Any such instability would be qualitatively different from any thermal instability that affects a radiation pressure dominated regime (Shakura & Sunyaev, 1976; Turner, 2004; Hirose et al., 2009; Jiang et al., 2013). In the temperature range between the low and high states relevant to dwarf novae, the opacity increases rapidly with increasing temperature because this is the regime in which H ionizes, so that the dominant opacity source is free-free or bound-free absorption of the negative hydrogen ion H^-. Thus, an upward fluctuation in heating receives positive feedback because it is accompanied by weaker cooling. By contrast, thermal fluctuations in the radiation-dominated regime are aided both by the sensitivity of radiation pressure to temperature ($\propto T^4$) and possible dynamical coupling between total thermal pressure (gas plus radiation) and heating associated with MHD turbulence (Jiang et al., 2013).

4.5 Chapter Summary

We have successfully identified two distinct stable branches of thermal equilibria in the hydrogen ionization regime of accretion disks: a hot ionized branch and a cool neutral branch. We have measured high values of α on the upper branch that are comparable to those inferred from observations of dwarf nova outbursts, the very systems where α is measured best. The physical mechanism for creating these high α values is specific to the physical conditions of the hydrogen ionization transition that is responsible for these outbursts. That mechanism is hydrodynamic convection triggered by the strong dependence of opacity upon temperature. We confirm the finding of Bodo et al. (2012)[7] that convection modifies the MRI dynamo to enhance magnetic stresses, but our more realistic treatment of opacity and thermodynamics yields a larger effect, with a substantial increase in α. Convection acts only in a narrow range of temperatures near the ionization transition because that is where the opacity is greatest. Thus the high values of α are restricted to the upper bend in the S-curve. Because the observational inference of high values of α is based on outburst light-curves, our finding that α is especially large near the low surface density end of the upper branch is relevant to the quantitative interpretation of these light-curves. Similarly, when we understand better the stresses in the plasma on the lower branch, where non-ideal MHD effects are important (see, for example, Menou, 2000), those results will bear on observational inferences tied to the recurrence times of dwarf novae.

[7] Although we express some doubts on the validity of their results in Section 5.5.1.

Chapter 5

Convection Quenches Magnetic Field Reversals

Vertically stratified shearing box simulations of magnetorotational turbulence commonly exhibit a so-called butterfly diagram of quasi-periodic azimuthal field reversals (as discussed in Chapter 2). However, in the presence of hydrodynamic convection, field reversals no longer occur. Instead, the azimuthal field strength fluctuates quasi-periodically while maintaining the same polarity, which can either be symmetric or antisymmetric about the disc midplane. Using data[1] from the simulations of Hirose et al. (2014), we demonstrate that the lack of field reversals in the presence of convection is due to hydrodynamic mixing of magnetic field from the more strongly magnetized upper layers into the midplane, which then annihilate field reversals that are starting there. Our convective simulations differ in several respects from those reported in previous work by others,

[1]These are the data from the simulations listed in Table 3.1 and presented in Chapter 4.

in which stronger magnetization likely plays a more important role than convection[2].

5.1 Introduction

Hydrodynamic convection does not simply enhance the turbulent stress to pressure ratio (i.e. α). It also fundamentally alters the character of the MRI dynamo. In the standard weak-field MRI, vertically stratified shearing box simulations exhibit quasi-periodic field reversals of the azimuthal magnetic field (B_y) with periods of ~ 10 orbits (Brandenburg et al., 1995; Davis et al., 2010). These reversals start near the midplane and propagate outward making a pattern (see top-left panel of Figure 5.1 below) which resembles a time inverse of the solar sunspot butterfly diagram. The means by which these field reversals propagate away from the midplane is likely the buoyant advection of magnetic flux tubes (Gressel, 2010), and many studies have also suggested that magnetic buoyancy is important in accretion disks (e.g. Galeev et al., 1979; Brandenburg & Schmitt, 1998; Miller & Stone, 2000; Hirose et al., 2006; Davis et al., 2010; Blaes et al., 2011). Magnetic buoyancy is consistent with the Poynting flux which tends to be oriented outwards (see top-right panel of Fig. 5.1), and we give further evidence supporting this theory below. While this explains how field reversals propagate through the disk, it does not explain how these magnetic field reversals occur in the first place, and despite numerous dynamo models there is currently no consensus on the physical mechanism driving the reversals (e.g. Brandenburg et al., 1995; Gressel, 2010; Shi et al., 2010, 2016; Squire & Bhattacharjee,

[2]The content of this chapter was first published in Coleman et al. (2017).

Simulation	h_0	Σ	$T_{\rm eff}$	α	N_x	N_y	N_z	L_x	L_y	L_z	$\frac{L_z}{h_{\rm p}}$	$t_{\rm th}$
ws0446 (conv)	9.51e8	127	7490	0.106	32	64	256	0.500	2.000	4.000	12.0	5.06
ws0429 (rad)	1.41e9	1030	13352	0.033	32	64	256	0.500	2.000	4.000	8.54	9.49

Table 5.1 Simulation parameters for the convective simulation ws0446 and radiative simulation ws0429. The units of time averaged surface densities (Σ), effective temperatures ($T_{\rm eff}$), height (h_0), and thermal time ($t_{\rm th}$) are, respectively, g cm^{-2}, K, cm, and orbits. L_x, L_y, and L_z are the lengths (in units of h_0), and N_x, N_y, and N_z are the numbers of cells, in the x, y, and in z directions, respectively. The pressure scale height of the steady state is computed as $h_{\rm p} \equiv \int [\langle p_{\rm thermal} \rangle]\, dz/2 \max([\langle p_{\rm thermal} \rangle])$. These simulations also appear in Table 3.1.

2015).

However, in the presence of convection, the standard pattern of azimuthal field reversals is disrupted. Periods of convection appear to be characterized by longer term maintenance of a particular azimuthal field polarity, and this persistent polarity can be of even (Bodo et al., 2015) or odd parity with respect to the disk midplane. As we discuss in this paper, the simulations of Hirose et al. (2014) also exhibit this pattern of persistent magnetic polarity during the intermittent periods of convection, but the field reversals associated with the standard butterfly diagram return during the episodes of radiative diffusion (see Fig. 5.1 below). Here we exploit this intermittency to try and understand the cause of the persistent magnetic polarity in the convective episodes. We demonstrate that this is due to hydrodynamic mixing of magnetic field from strongly magnetized regions at high altitude back toward the midplane.

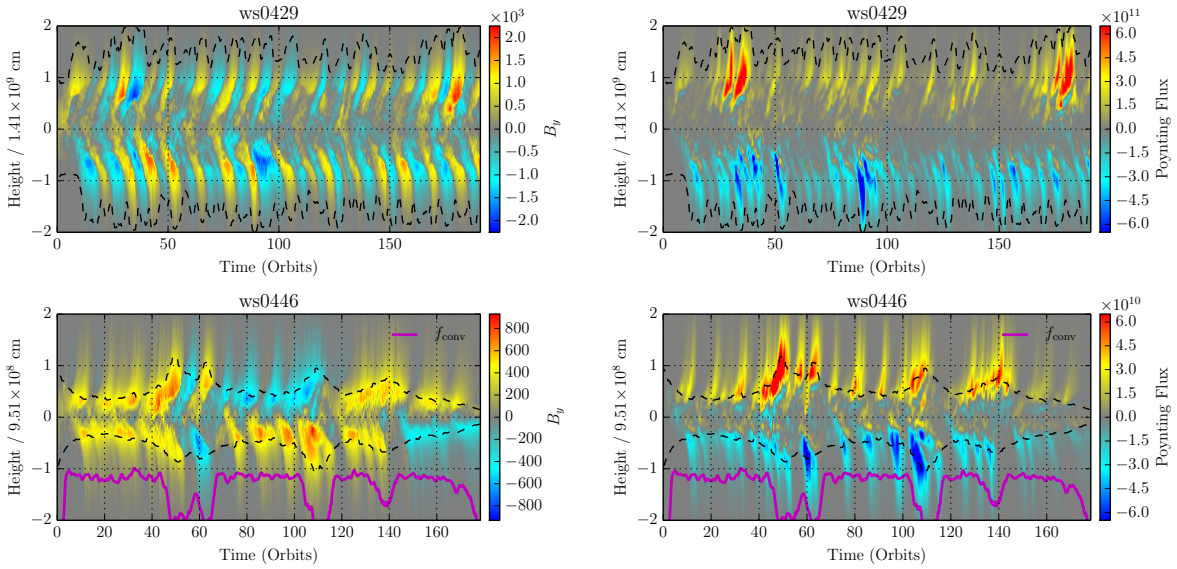

Figure 5.1 Horizontally-averaged azimuthal magnetic field $\langle B_y \rangle$ (left frames), and 1 orbit smoothed horizontally-averaged vertical Poynting flux $\{\langle F_{\mathrm{Poynt},z} \rangle\}_t$ (right frames) as a function of time and height for a radiative simulation (ws0429, top frames) and a simulation which exhibits convective epochs (ws0446, bottom frames). For the Poynting flux frames, we have purposely allowed some of the data to lie outside the colorbar range (which then shows up as saturated regions) in order to increase the color contrast in the midplane regions. The normalizations indicated in the vertical axes are the respective simulation length units. The dashed black lines show the time-dependent heights of the photospheres in the horizontally averaged structures. For simulation ws0446, which exhibits convection, the convective fraction $f_{\mathrm{conv}} - 2$ (see Eqn. 5.2) is plotted in magenta. Note that $f_{\mathrm{conv}} - 2$ uses the same vertical scale as B_y, i.e. when the magenta line is near -1 then $f_{\mathrm{conv}} \approx 1$. Focusing on B_y, the radiative simulation ws0429 shows the standard pattern of field reversals normally associated with the butterfly diagram. In simulation ws0446 where f_{conv} is high, the field maintains its sign and all changes in sign/parity are associated with a dip in f_{conv}.

5.2 The Butterfly Diagram

To construct the butterfly diagram and explore its physical origin, it is useful to define the following quantities related to some fluid variable f: the horizontal average of this quantity, the variation with respect to this horizontal average, and a version of the variable that is smoothed in time over one orbit. These are defined respectively by

$$\langle f \rangle (t,z) \equiv \frac{1}{L_x L_y} \int_{-L_x/2}^{L_x/2} dx \int_{-L_y/2}^{L_y/2} dy f(t,x,y,z) \tag{5.1a}$$

$$\delta f \equiv f - \langle f \rangle , \tag{5.1b}$$

$$\{f\}_t (t) \equiv \int_{t-1/2}^{t+1/2} f(t')\, dt' \Big/ 1 \text{ orbit} . \tag{5.1c}$$

Here L_x, L_y, and L_z are the radial, azimuthal and vertical extents of the simulation domain, respectively (listed in Table 5.1). Additionally we define the quantity $f_{\rm conv}$ as a means to estimate the fraction of vertical energy transport which is done by convection:

$$f_{\rm conv}(t) \equiv \left\{ \frac{\int \{\langle (e+E)\, v_z \rangle\}_t \, {\rm sign}(z) \, \langle P_{\rm th} \rangle \, dz}{\int \{\langle F_{{\rm tot},z} \rangle\}_t \, {\rm sign}(z) \, \langle P_{\rm th} \rangle \, dz} \right\}_t , \tag{5.2}$$

where e is the gas internal energy density, E is the radiation energy density, v_z is the vertical velocity, $P_{\rm th}$ is the thermal pressure (gas plus radiation), and $F_{{\rm tot},z}$ is the total energy flux in the vertical direction, including Poynting and radiation diffusion flux. These quantities will assist us in analyzing and discussing the interactions between convection and dynamos in accretion disks.

The butterfly diagram is obtained by plotting $\langle B_y \rangle$ as a function of time and distance from the disk midplane (see left frames of Fig. 5.1). The radiative simulation ws0429

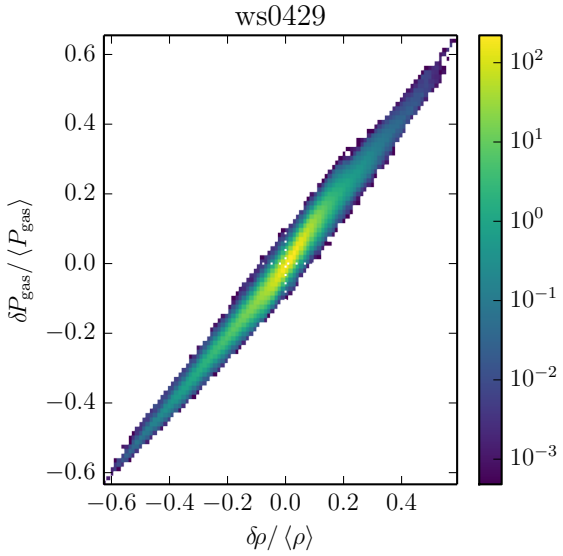

Figure 5.2 A 2D histogram of horizontal variations (see Eqn. 5.1b) of mass density ($\delta\rho$, horizontal axis) and gas pressure ($\delta P_{\rm gas}$, vertical axis) for the fully radiative simulation ws0429. Each grid zone saved to file from this simulation with $90 \leq t \leq 190$ and $|z| \leq 0.5$ simulation units is placed into one of 100×100 bins based on its local properties. The resulting normalized probability density is shown here with the given color bar. The probability density, p, is normalized so that $\int p(\tilde{x}, \tilde{y})\, d\tilde{x}\, d\tilde{y} = 1$ where $\tilde{x}$ and $\tilde{y}$ are the variables used for the horizontal and vertical axes, respectively. The tight linear correlation between $\delta\rho$ and $\delta P_{\rm gas}$ signifies that temperature variations are small at any fixed height, i.e. horizontal fluctuations are isothermal.

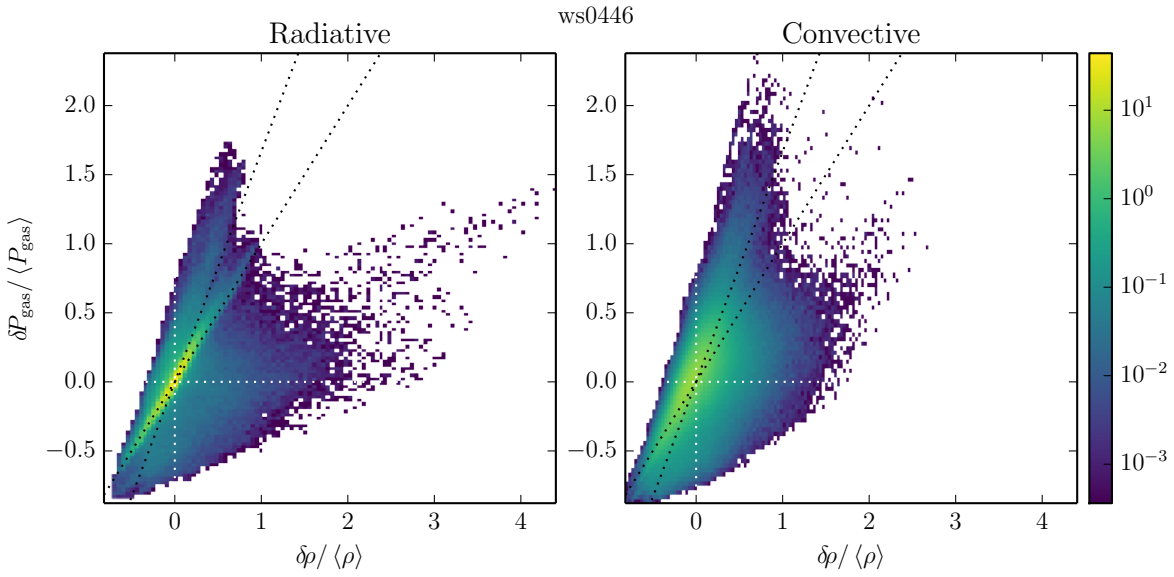

Figure 5.3 2D histograms of horizontal variations of mass density ($\delta\rho$, horizontal axis) and gas pressure ($\delta P_{\rm gas}$, vertical axis) in the convective simulation ws0446. The left panel shows data from a radiative epoch ($49 \leq t \leq 64$), and the right panel shows data from a convective epoch ($70 \leq t \leq 100$). The two dotted black lines in each figure show the expected relations for isothermal (slope 1) and monatomic adiabatic (slope 5/3) gases. During the radiative epoch there is a significant population of cells that lie on the line $\delta P_{\rm gas} = \delta\rho$ just as in Fig. 5.2. However there is also a significant amount of dispersion which resembles the probability distribution of the convective epoch, therefore it is likely that this dispersion is a remnant of the previous convective epoch. During the convective epoch the yellow core of the probability distribution follows a linear trend with a slope steeper than 1. This is indicative of perturbations which are adiabatic and the spread in slopes over this yellow region are likely due to the variation in $\Gamma_1 \equiv (\partial \ln P_{\rm gas}/\partial \ln \rho)_s$ from our equation of state, which includes in particular the effects of ionizing hydrogen. Values of Γ_1 range from about 1.15 to 5/3 in this simulation. The population below $\delta P_{\rm gas} = \delta\rho$ is likely a result of vertical mixing.

(from Hirose et al., 2014, and listed in Table 5.1) shows the standard pattern of field reversals normally associated with the butterfly diagram, which appear to start at the midplane and propagate outwards. This outward propagation of magnetic field is consistent with the Poynting flux (also shown in Fig. 5.1), which generally points outwards away from the midplane.

When simulations with convection are examined (e.g. ws0446 listed in Table 5.1), however, the butterfly diagram looks completely different (see bottom left frame of Fig. 5.1), as first discussed by Bodo et al. (2015). Similar to the lack of the azimuthal magnetic field reversals found by these authors, we find that when convection is present in the Hirose et al. (2014) simulations, there is also a lack of field reversals. Additionally, we find that the azimuthal magnetic field in the high altitude "wings" of the butterfly diagram is better characterized by quasi-periodic pulsations, rather than quasi-periodic field reversals. These pulsations have roughly the same period as the field reversals found in radiative epochs. For example, the convective simulation ws0446 shown in Fig. 5.1 has a radiative epoch where field reversals occur (centered near 55 orbits), and the behavior of this epoch resembles that of the radiative simulation ws0429. However, during convective epochs where $f_{\rm conv}$ is high, the field maintains its polarity and pulsates with a period of ~ 10 orbits. In fact, the only time field reversals occur is when $f_{\rm conv}$ dips to low values[3], indicating that radiative diffusion is dominating convection.

This lack of field reversals during convective epochs locks the vertical structure of

[3]As discussed in Chapter 4 $f_{\rm conv}$ can be slightly negative. This can happen when energy is being advected inwards to the disk midplane.

B_y into either an even parity or odd parity state, where B_y maintains sign across the midplane or it changes sign, respectively (compare orbits 10-40 to orbits 70-100 in the bottom left panel of Fig. 5.1). This phenomenon of the parity of B_y being held fixed throughout a convective epoch shall henceforth be referred to as *parity locking*. During even parity epochs (e.g. orbits 10-40 and 120-140 of ws0446), there are field reversals in the midplane, but they are quickly quenched, and what field concentrations are generated here do not migrate away from the midplane as they do during radiative epochs. Also during even parity convective epochs, the Poynting flux tends to be oriented inwards roughly half way between the photospheres and the midplane. For odd parity convective epochs the behavior of the Poynting flux is more complicated but is likely linked to the motion of the $\langle B_y \rangle = 0$ surface.

In summary, we seek to explain the following ways in which convection alters the butterfly diagram:

1. Magnetic field reversals near the midplane are quickly quenched during convective epochs.

2. Magnetic field concentrations do not migrate away from the midplane during convective epochs as they do during radiative epochs.

3. During convective epochs, the magnetic field in the wings of the butterfly diagram is better characterized by quasi-periodic pulsations, rather than quasi-periodic field reversals, with roughly the same period.

4. B_y is held fixed in either an odd or even parity state during convective epochs.

5.3 Thermodynamics and Magnetic Buoyancy

Much like in Blaes et al. (2011), we find that that during radiative epochs, nonlinear concentrations of magnetic field form in the midplane regions, and these concentrations are underdense and therefore buoyant. The resulting upward motion of these field concentrations is the likely cause of the vertically outward moving field pattern observed in the standard butterfly diagram. In our simulations, this magnetic buoyancy appears to be more important when radiative diffusion, rather than convection, is the predominant energy transport process. This is due to the different opacities and rates of radiative diffusion between these two regimes, which alter the thermodynamic conditions of the plasma.

When the disk is not overly opaque, and convection is therefore never present, temperature variations (δT) at a given height are rapidly suppressed by radiative diffusion. This causes horizontal variations in gas pressure ($\delta P_{\rm gas}$) and mass density ($\delta\rho$) to be highly correlated (see Fig. 5.2), and allows us to simplify our analysis by assuming $\delta T = 0$. This should be contrasted with convective simulations (see Fig. 5.3) which show a much noisier relation and show a tendency towards adiabatic fluctuations during convective epochs.

By computing rough estimates of the thermal time we can see how isothermal and adiabatic behaviour arise for radiative and convective epochs, respectively. The time

scale to smooth out temperature fluctuations over a length scale ΔL is simply the photon diffusion time times the ratio of gas internal energy density e to photon energy density E,

$$t_{\rm th} \simeq \frac{3\kappa_{\rm R}\rho(\Delta L)^2}{c}\frac{e}{E}. \tag{5.3}$$

For the midplane regions of the radiative simulation ws0429 at times $75-100$ orbits, the density $\rho \simeq 7\times10^{-7}$g cm^{-3}, $e \simeq 2\times10^{7}$ erg cm^{-3}, $E \simeq 9\times10^{5}$ erg cm^{-3}, and the Rosseland mean opacity $\kappa_R \simeq 10$ cm^2 g^{-1}. Hence, $t_{\rm th} \simeq 30(\Delta L/H)^2$ orbits. Radiative diffusion is therefore extremely fast in smoothing out temperature fluctuations on scales of order several tenths of a scale height, causing horizontal fluctuations to be roughly isothermal.

Isothermality ($T = \langle T\rangle$) in combination with pressure equilibrium ($P_{\rm tot} = \langle P_{\rm tot}\rangle$) leads to the following equation:

$$\langle P_{\rm tot}\rangle = \frac{\rho}{\mu m_p}k\,\langle T\rangle + P_{\rm mag}, \tag{5.4}$$

where radiation pressure has been neglected, as $P_{\rm rad} \ll P_{\rm gas}$. During radiative epochs, this requires that regions of highly concentrated magnetic field (e.g. flux tubes) must be under-dense. Figure 5.4 confirms this for the radiative simulation ws0429 by depicting a 2D histogram of magnetic pressure and density fluctuations. A clear anticorrelation is seen which extends up to very nonlinear concentrations of magnetic field, all of which are underdense. This anticorrelation was also observed in radiation pressure dominated simulations appropriate for high luminosity black hole accretion disks in Blaes et al. (2011). This anti-correlation causes the buoyant rise of magnetic field which would

explain the outward propagation seen in the butterfly diagram and is also consistent with the vertically outward Poynting flux (see top panels of Figure 5.1).

On the other hand, for the midplane regions of the convective simulation ws0446 at the times $80-100$ orbits, $\rho \simeq 2\times10^{-7}$g cm^{-3}, $e \simeq 3\times10^{6}$ erg cm^{-3}, $E \simeq 1\times10^{3}$ erg cm^{-3}, and $\kappa_{\rm R} \simeq 7 \times 10^{2}$ cm^{2} g^{-1}. Hence, $t_{\rm th} \simeq 4 \times 10^{4}(\Delta L/H)^{2}$ orbits. All fluctuations in the midplane regions that are resolvable by the simulation are therefore roughly adiabatic. Perhaps somewhat coincidentally, $\Gamma_1 \approx 1.3$ in the midplane regions of the convective simulation, so the pressure-density fluctuations, even though adiabatic, are in any case close to an isothermal relationship[4]. However, the biggest difference between the radiative and convective cases is caused by the departure from isothermality in convective epochs, allowing for the possibility of highly magnetized regions to be overdense. This leads to much larger scatter in the probability distribution of the density perturbations in convective epochs. How this affects magnetic buoyancy in radiative and convective epochs will be discussed in detail in the next section.

5.4 Effects of Convection

In this section we lay out the main mechanisms by which convection acts to modify the dynamics of the dynamo and thereby fundamentally alter the large scale magnetic field

[4] This reduction in the adiabatic gradient within the hydrogen ionization transition actually contributes significantly to establishing a convectively unstable situation in our dwarf nova simulations. We typically find that the adiabatic temperature gradient $\nabla_{\rm ad}$ within the hydrogen ionization transition is significantly less than the value 0.4 for a monatomic gas. In fact, the gas pressure weighted average value of $\nabla_{\rm ad}$ can be as low as 0.18. For $\sim 60\%$ of the convective simulations of Hirose et al. (2014) and Coleman et al. (2016), the temperature gradient ∇ is superadiabatic but less than 0.4 during convective epochs.

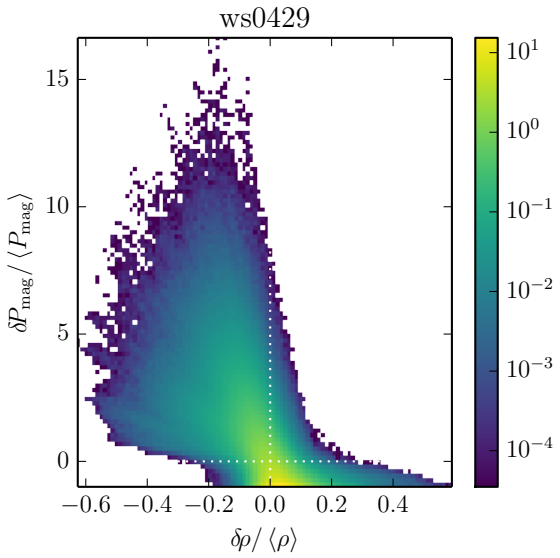

Figure 5.4 A 2D histogram of horizontal variations of mass density ($\delta\rho$, horizontal axis) and magnetic pressure ($\delta P_{\rm mag}$, vertical axis), using data from the same vertical and temporal ranges as Fig. 5.2. The rough anti-correlation between $\delta\rho$ and $\delta P_{\rm mag}$ signifies that highly magnetized regions are likely to be underdense, causing them to be buoyant.

structure in the simulations.

5.4.1 Mixing from the Wings

As a convective cell brings warm underdense plasma from the midplane outward towards the photosphere (i.e. the wing region of the butterfly diagram), it must also circulate cold overdense material from the wing down towards the midplane. As is typical of stratified shearing box simulations of MRI turbulence (e.g. Miller & Stone 2000; Krolik et al. 2007), the horizontally and time-averaged magnetic energy density peaks away from the midplane, and the surface photospheric regions are magnetically dominated. Dense fluid parcels that sink down toward the midplane are therefore likely to carry

significant magnetic field inward. These fluid parcels that originated from high altitude can actually be identified in the simulations because the high opacity, which contributes to the onset of convection, prevents cold fluid parcels from efficiently thermalizing with their local surroundings. Hence they retain a lower specific entropy compared to their surroundings as they are brought to the midplane by convective motions. We therefore expect negative specific entropy fluctuations in the midplane regions to be correlated with high azimuthal magnetic field strength of the same polarity as the photospheric regions during a convective epoch. Figures 5.5 and 5.6 show that this is indeed the case.

Figure 5.5 shows a 2D histogram of entropy fluctuations and azimuthal field strength B_y in the midplane regions for the even parity convective epoch $15 \leq t \leq 40$ in simulation ws0446 (see Fig. 5.1). The yellow vertical population is indicative of adiabatic fluctuations (i.e. $\delta s = 0$) at every height which are largely uncorrelated with B_y. However, the upper left quadrant of this figure shows a significant excess of cells with lower than average entropy for their height and large positive B_y. It is important to note that this corresponds to the sign of the azimuthal field at high altitude, even though near the midplane $\langle B_y \rangle$ is often negative (see bottom panel of Fig. 5.1). This is strong evidence that convection is advecting low entropy magnetized fluid parcels from the near-photosphere regions into the midplane.

Figure 5.6 shows the same thing for the odd parity convective epoch $80 \leq t \leq 100$. Because the overall sign of the horizontally-averaged azimuthal magnetic field flips across the midplane, cells that are near but above the midplane are shown in the left panel, while

cells that are near but below the midplane are shown on the right. Like in Figure 5.5, there is a significant excess of negative entropy fluctuations that are correlated with azimuthal field strength and have the same sign as the field at higher altitudes *on the same side of the midplane*. Again, these low entropy regions represent fluid parcels that have advected magnetic field inward from higher altitude. The correlation between negative entropy fluctuation and azimuthal field strength is somewhat weaker than in the even parity case (Fig. 5.5), but that is almost certainly due to the fact that inward moving fluid elements can overshoot across the midplane.

In contrast, Figure 5.7 shows a similar histogram of entropy fluctuations and B_y for the radiative simulation ws0429, and it completely lacks this correlation between high azimuthal field strength and negative entropy fluctuation. This is in part due to the fact that fluid parcels are no longer adiabatic, but isothermal. But more importantly, it is because there is no mixing from the highly magnetized regions at high altitude down to the midplane. Instead, the tight crescent shaped correlation of Figure 5.7 arises simply by considering the linear theory of isothermal, isobaric fluctuations at a particular height. Such fluctuations have perturbations in entropy given by

$$\delta s = \frac{k}{\mu m_p} \frac{B^2 - \langle B^2 \rangle}{2 \langle P_{\rm gas} \rangle}. \tag{5.5}$$

This is shown as the dotted line in Figure 5.7, and fits the observed correlation very well.

The inward flux of magnetic energy from high altitude is also energetically large enough to quench field reversals in the midplane regions. To demonstrate this, we examined the divergence of the Poynting flux and compared it to the time derivative of the

magnetic pressure. During radiative epochs when the magnetic field is growing after a field reversal, typical values for $\mathrm{d}\left\langle P_{\mathrm{mag}}\right\rangle/\mathrm{d}t$ in the midplane are about half of the typical value of $-\mathrm{d}\left\langle F_{\mathrm{Poynt},z}\right\rangle/\mathrm{d}z$ near the midplane during convective epochs. This shows that the magnetic energy being transported by the Poynting flux during convective epochs is strong enough to quench the field reversals that would otherwise exist. The sign of the divergence of the Poynting flux during convective epochs is also consistent with magnetic energy being removed from high altitude (positive) and deposited in the midplane (negative).

To conclude, by using specific entropy as a proxy for where a fluid parcel was last in thermal equilibrium, we have shown that convection advects field inward from high altitude, which is consistent with the inward Poynting flux seen during even parity convective epochs (see Fig. 5.1). The lack of such clear inward Poynting flux during the odd parity convective epochs is likely related to the movement of the $\langle B_y\rangle = 0$ surface by convective overshoot across the disk midplane. However, in both even and odd convective epochs $\mathrm{d}\left\langle F_{\mathrm{Poynt},z}\right\rangle/\mathrm{d}z$ is typically a few times $\mathrm{d}\left\langle P_{\mathrm{mag}}\right\rangle/\mathrm{d}t$ and is consistent with enough magnetic energy being deposited in the midplane to quench field reversals that would otherwise take place. This further suggests that regardless of parity, this convective mixing from high altitude to the midplane is quenching field reversals in the midplane by mixing in field of a consistent polarity.

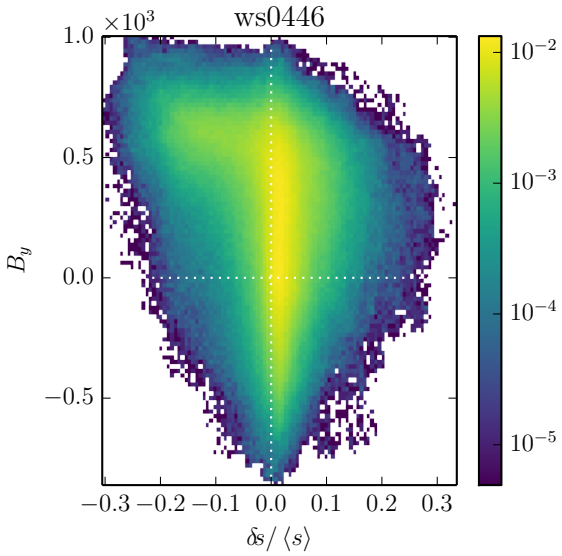

Figure 5.5 A 2D histogram of azimuthal magnetic field (B_y, vertical axis) and horizontal variations of specific entropy (δs, horizontal axis) for an even parity convective epoch. Each cell saved to file from ws0446 with $15 \leq t \leq 40$ and $|z| \leq 0.25$ simulation units is placed into one of 100×100 bins based on its local properties. The light green region at low entropy ($-0.2 \lesssim \delta s < 0$) and high magnetic field ($B_y \gtrsim 500$) signifies highly magnetized fluid parcels which have been mixed towards the midplane by convection.

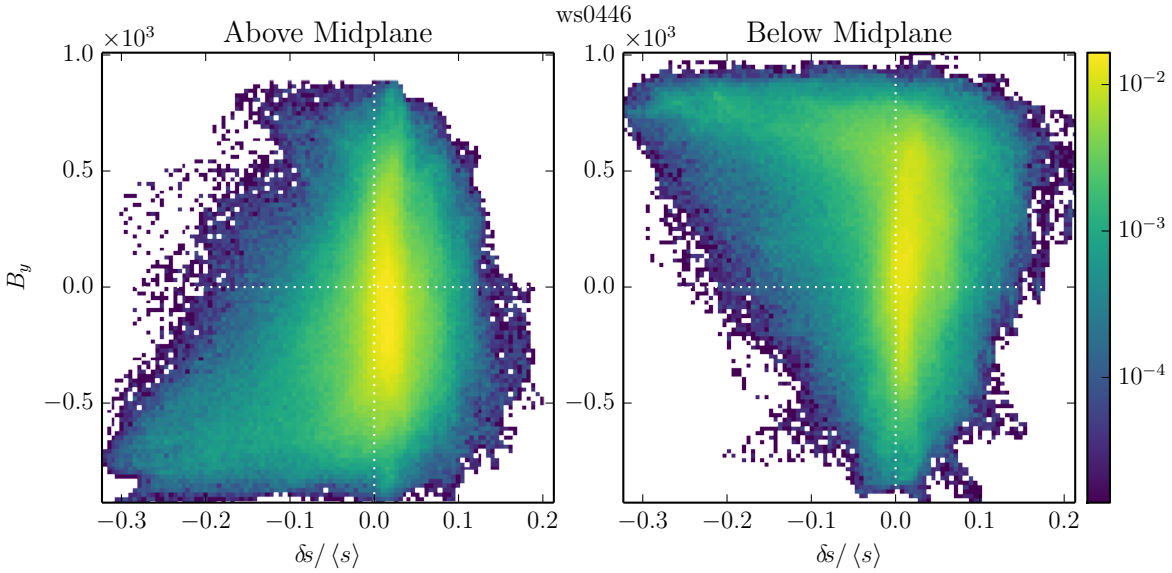

Figure 5.6 2D histograms of azimuthal magnetic field (B_y, vertical axis) and horizontal variations of specific entropy (δs, horizontal axis). Each cell saved to file from ws0446 with $80 \leq t \leq 100$ and $0 \leq z \leq 0.25$ simulation units (left) and $-0.25 \leq z \leq 0$ simulation units (right) are used to create the respective histograms. It is important to note that for both panels there is a low entropy, high $|B_y|$ tail which corresponds to the sign of the respective wings of the butterfly diagram (see bottom panel of Fig. 5.1), indicating that convection is mixing regions of high magnetization from the wings into the midplane.

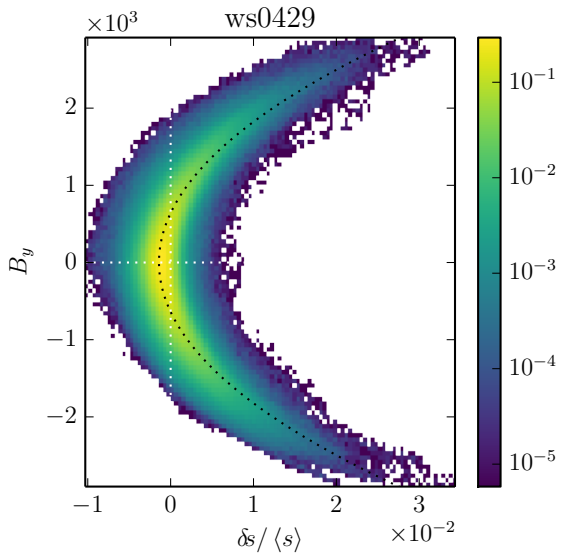

Figure 5.7 A 2D histogram of azimuthal magnetic field (B_y, vertical axis) and horizontal variations of specific entropy (δs, horizontal axis) for the radiative simulation ws0429. Note the symmetry and how the probability distribution curves to high entropy at high magnetic field strength. This curvature is indicative of isothermal, isobaric fluctuations and matches well with linear theory (black dotted line) which is computed from Eqn. 5.5 assuming that $B^2 = B_y^2$. This trend should be contrasted with what we observe during convective epochs in Figs. 5.5 and 5.6. Note that the entropy fluctuations here are an order of magnitude smaller compared to those of the convective simulation ws0446.

5.4.2 Disruption of Magnetic Buoyancy

In addition to quenching magnetic field reversals, convection and the associated high opacities act to disrupt magnetic buoyancy which transports field away from the mid-plane, thereby preventing any reversals which do occur, from propagating vertically outwards. The large opacities which contribute to the onset of convection also allow for thermal fluctuations on a given horizontal slice (δT) to persist for several orbits. This breaks one of the approximations which lead to the formulation of Eqn. 5.4, allowing for the possibility for large magnetic pressures to be counterbalanced by low temperatures, reducing the anti-correlation between density and temperature. Additionally, convective turbulence also generates density perturbations that are uncorrelated with magnetic fields, and combined with the lack of isothermality can cause fluid parcels to have both a high magnetic pressure and be overdense (see Fig. 5.8). These overdense over-magnetized regions can be seen in the right (convective) frame of Fig. 5.8 where the probability density at $\delta\rho \approx 0.5 \langle\rho\rangle$, $\delta P_{\rm mag} \approx \langle P_{\rm mag}\rangle$ is only about one order of magnitude below its peak value. This should be contrasted with the left (radiative) frame of the same figure and with Fig. 5.4 where the probability density at this coordinate is very small or zero respectively. Hence while the overall anti-correlation between magnetic pressure and density still exists in convective epochs, indicating some magnetic buoyancy, the correlation is weakened by the presence of overdense high magnetic field regions. Magnetic buoyancy is therefore weakened compared to radiative epochs.

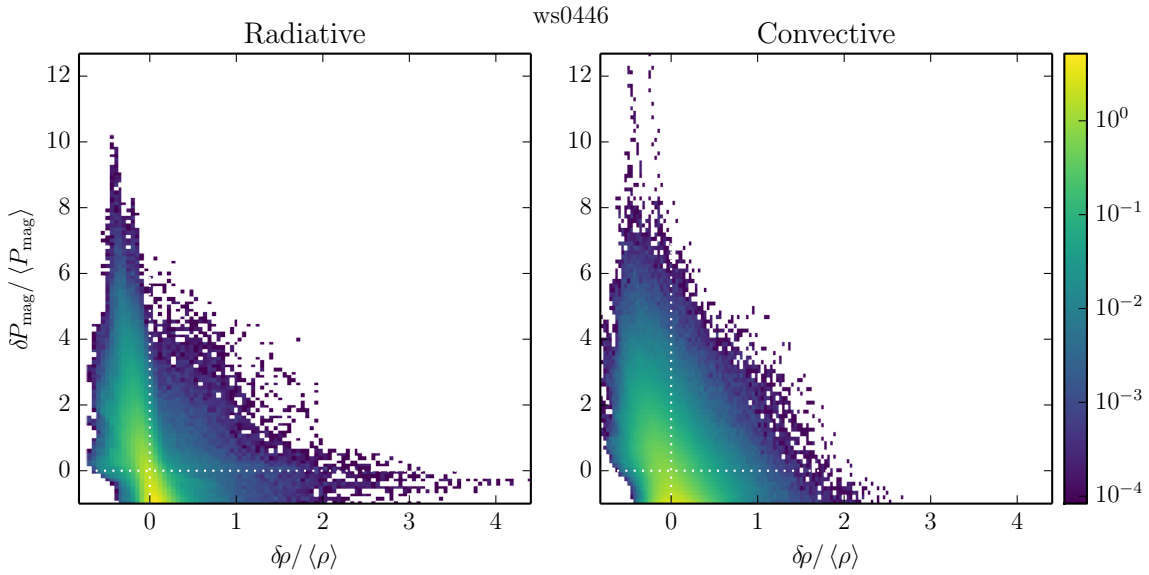

Figure 5.8 2D histograms of horizontal variations of mass density ($\delta\rho$, horizontal axis) and magnetic pressure ($\delta P_{\rm mag}$, vertical axis). The left panel shows data from a radiative epoch ($49 \leq t \leq 64$) of simulation ws0446 and the right panel shows data from a convective epoch ($70 \leq t \leq 100$) of the same simulation. While there is still a rough anti-correlation between $\delta\rho$ and $\delta P_{\rm mag}$ as seen in Fig. 5.4 this correlation is much weaker here. Also, note that the scale of the x-axis here is an order of magnitude higher than that of Fig. 5.4. The left frame is similar to the data from ws0429 but has an extra source of dispersion which is likely connected to previous episodes of convection. The right frame has a significantly higher population of overdense and highly magnetized fluid parcels compared to the radiative epoch. This signifies that magnetic buoyancy is weakened during convective epochs.

5.4.3 Parity Locking

The effects described above both prevent magnetic field reversals in the midplane and reduce the tendency for any reversals which manage to occur from propagating outwards. Therefore convection creates an environment which prevents field reversals, and leads to the parity of the field being locked in place. Due to the variety of parities seen, it appears likely that it is simply the initial conditions when a convective epoch is initiated that set the parity for the duration of that epoch.

5.5 Discussion

It is important to note that we still do not understand many aspects of the MRI turbulent dynamo. Our analysis here has not shed any light on the actual origin of field reversals in the standard (non-convective) butterfly diagram, nor have we provided any explanation for the quasi-periodicities observed in both the field reversals of the standard diagram and the pulsations that we observe at high altitude during convective epochs. However, the outward moving patterns in the standard butterfly wings combined with the fact that the horizontally-averaged Poynting flux is directed outward strongly suggests that field reversals are driven in the midplane first and then propagate out by magnetic buoyancy. On the other hand, we continue to see the same quasi-periodicity at high altitude in convective epochs as we do in the field reversals in the radiative epochs. Moreover, it is clear from Figure 5.1 that field reversals occasionally start to manifest in the midplane regions during convective epochs, but they simply cannot be sustained because they are

annihilated by inward advection of magnetic field of sustained polarity. This suggests perhaps that there are two spatially separated dynamos which are operating. This modification of the dynamo by convection presents a challenge to dynamo models. However, potentially promising dynamo mechanisms have recently been discovered in stratified and unstratified shearing boxes.

Recently, Shi et al. (2016) found that quasi-periodic azimuthal field reversals occur even in unstratified, zero net flux shearing box simulations, provided they are sufficiently tall ($L_z/L_x \geq 2.5$). Furthermore, they found that the magnetic shear-current effect (discussed in Squire & Bhattacharjee, 2015) was responsible for this dynamo; however, they were not able to explain why the reversals occurred. The shear-current effect can also apparently be present during hydrodynamic convection (Rogachevskii & Kleeorin, 2007), implying that this dynamo mechanism might be capable of persisting through convective epochs.

Most of the work on the MRI dynamo has been done with vertically stratified shearing box simulations. One of the earliest examples of this is Blackman & Tan (2004), who found that multiple dynamos can work in conjunction with the MRI on different scales. This is consistent with the findings of Gressel (2010), that an "indirect" larger scale dynamo should coexist with the MRI, and they propose two candidates: a Parker-type dynamo (i.e. the α-effect; Parker, 1955; Ruediger & Kichatinov, 1993), and a "buoyant" dynamo caused by the Lorentz force. Furthermore, Gressel & Pessah (2015) find that the $\alpha\Omega$ dynamo produces cycle frequencies comparable to that of the butterfly diagram, and

that there is a non-local relation between electromotive forces and the mean magnetic field which varies vertically throughout the disk. This sort of non-local description may be necessary to understand how the midplane and high altitude regions differ from each other, and we hope to pursue such an analysis in future work.

5.5.1 Departures from Standard Disc Dynamo: Comparison with Other Works

We find that some properties of the dynamo during convective epochs are similar to the convective simulations of Bodo et al. (2012, 2015), such as prolonged states of azimuthal magnetic field polarity and an enhancement of Maxwell stresses compared to purely radiative simulations (see, e.g. Figure 6 of Hirose et al. 2014). However, there are some dynamo characteristics observed by Bodo et al. (2015) that are not present in our simulations. For example, their simulations typically evolved to a strongly magnetized state, something which we never find. We also find that in our simulations, which exhibit intermittent convection, the time-averaged Maxwell stress in the midplane regions is approximately the same in both the convective and radiative epochs[5], and is independent of the vertical parity of the azimuthal field. In contrast, Bodo et al. (2015) find substantially less Maxwell stress during odd parity epochs. Azimuthal field reversals occasionally occur during their convective simulations, whereas we never see such reversals during our convective epochs. Finally, their simulations exhibit a strong preference for epochs of

[5]Although the Maxwell stress is approximately the same between radiative and convective epochs in a given simulation, the α parameter is enhanced during convective epochs because the medium is cooler and the time-averaged midplane pressure is smaller.

even parity, and a lack of quasi-periodic pulsations in the wings of the butterfly diagram.

Remarkably, all of these aforementioned properties arise in strongly magnetized shearing box simulations (Bai & Stone, 2013; Salvesen et al., 2016b). We suggest here that these properties of the dynamo that Bodo et al. (2015) attribute to convection are actually a manifestation of strong magnetization. To demonstrate this, we start by noting that the simulations presented in Bodo et al. (2015) adopted: (1) impenetrable vertical boundary conditions that prevented outflows, trapping magnetic field within the domain, and (2) initial configurations with either zero or non-zero net vertical magnetic flux.

We first consider the Bodo et al. (2015) simulations with net vertical magnetic flux. Figure 10 of Bodo et al. (2015) shows that for increasing net vertical flux, the strength of the azimuthal field increases and field reversals decrease in frequency with long-lived (short-lived/transitionary) epochs of even (odd) parity. No dynamo flips in the azimuthal field were seen for the strongest net flux case. Figure 5.9 shows that the *isothermal* net vertical flux simulations of Salvesen et al. (2016b) reproduce all features of the butterfly diagrams in the convective simulations of Bodo et al. (2015), for the same range of initial plasma-β. This remarkable similarity between these simulations with and without convective heat transport suggests that strong magnetization (i.e., $\beta \sim 1$ at the disk midplane) is responsible for the conflicts listed in the previous paragraph with the Hirose et al. (2014) simulations under consideration.

We now seek to understand the role of convection on dynamo behavior in the zero net vertical magnetic flux simulations of Bodo et al. (2015). These simulations also developed

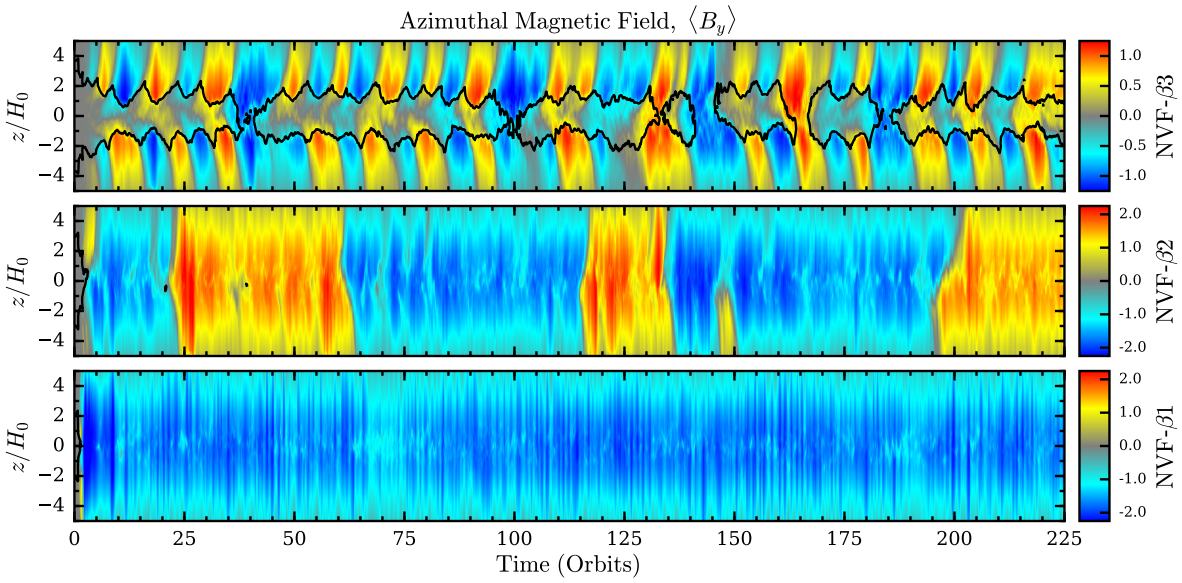

Figure 5.9 Vertical profiles of the horizontally-averaged azimuthal magnetic field for isothermal shearing box simulations with different levels of net vertical magnetic flux corresponding to an initial mid-plane plasma-β of: $\beta_0^{\rm mid} = 1000$ (*top*), $\beta_0^{\rm mid} = 100$ (*middle*), $\beta_0^{\rm mid} = 10$ (*bottom*). *Black lines* in the top panel mark the $\beta = 1$ contour and are absent in the bottom two panels because $\beta < 1$ throughout the entire vertical column. For these simulations and the net vertical flux simulations considered by Bodo et al. (2015) where $\beta_0^{\rm mid} \lesssim 1000$, the entire disk becomes strongly magnetized (i.e., $\beta \lesssim 1$ everywhere). The butterfly patterns seen in the convective net vertical flux simulations in Figure 10 of Bodo et al. (2015) bears a striking resemblance to these isothermal simulations, which do not have convective heat transport. This is suggestive that the dramatic departure from the usual butterfly pattern seen in the net flux simulations of Bodo et al. (2015) is due to strong magnetization. (This figure is reproduced from Salvesen et al. 2016b.)

into a strongly magnetized state and exhibited similarly dramatic departures from the standard butterfly pattern as their net flux counterparts. Gressel (2013) demonstrated that zero net vertical flux shearing box simulations with constant thermal diffusivity and the same impenetrable vertical boundaries adopted by Bodo et al. (2015) lead to the following: (1) A butterfly pattern that is irregular, yet still similar to the standard pattern that is recovered for outflow boundaries. However, the box size in Gressel (2013) was comparable to the smallest domain considered in Bodo et al. (2015), which was not a converged solution. (2) Maxwell stresses that are enhanced by a factor of ~ 2 compared to the simulation with outflow boundaries. This is likely because impenetrable boundaries confine magnetic field, which would otherwise buoyantly escape the domain (Salvesen et al., 2016a). (3) Substantial turbulent convective heat flux, which is significantly reduced when using outflow boundaries. Therefore, perhaps the enhanced convection resulting from using impenetrable boundaries is indeed responsible for the strongly magnetized state and dynamo activity seen in the "Case D" zero net flux simulation of Bodo et al. (2015).

Despite starting with identical initial and boundary conditions, the zero net vertical flux simulation M4 of Gressel (2013) does not evolve to the strongly magnetized state seen in the Bodo et al. (2015) simulations. The reason for this discrepancy is unclear. In an attempt to reproduce Case D in Bodo et al. (2015) and following Salvesen et al. (2016a), we ran an *isothermal*, zero net vertical flux shearing box simulation that had an initial magnetic field, $\mathbf{B} = B_0 \sin(2\pi x/L_x)$, where B_0 corresponded to $\beta_0 = 1600$. This

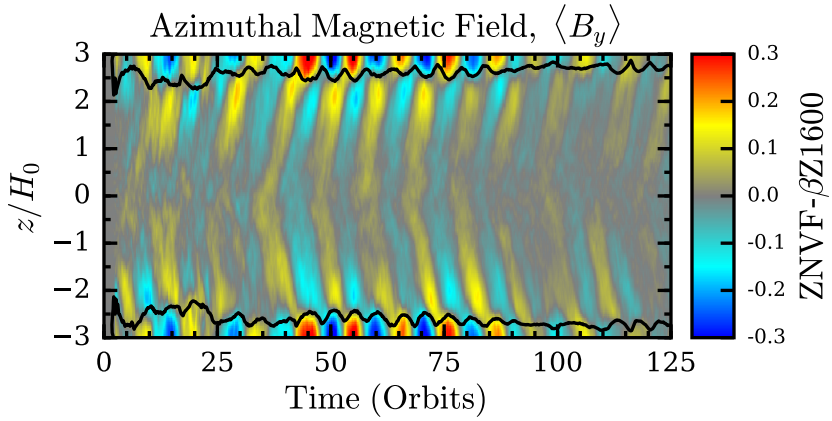

Figure 5.10 Vertical profile of the horizontally-averaged azimuthal magnetic field for the isothermal, zero net vertical flux shearing box simulation ZNVF-β1600, which was designed to reproduce the Case D simulation of Bodo et al. (2015). Unlike Case D, the ZNVF-β1600 simulation displays the standard butterfly pattern and does not develop strong magnetization. We note that the Gressel (2013) simulations with finite thermal diffusivity also did not generate dynamically important magnetic fields.

simulation, labeled ZNVF-βZ1600, had domain size $(L_x, L_y, L_z) = (24H_0, 18H_0, 6H_0)$ with H_0 being the initial scale height due to thermal pressure support alone, resolution 24 zones/H_0 in all dimensions, and periodic vertical boundaries that trap magnetic field, which we believe to be the salient feature of the impenetrable boundaries discussed above. Figure 5.10 shows that the space-time diagram of the horizontally-averaged azimuthal magnetic field for this simulation does not reproduce Case D, but instead evolves to a weakly magnetized state with a conventional butterfly pattern.

However, we note that Gressel (2013) found that the standard butterfly diagram is recovered when replacing impenetrable boundaries with outflow boundaries. Similarly, Salvesen et al. (2016a) initialized two zero net vertical flux simulations with a purely azimuthal magnetic field corresponding to $\beta_0 = 1$. In simulation ZNVF-P, which adopted

periodic boundary conditions that prevent magnetic field from buoyantly escaping, the butterfly pattern was not present and the azimuthal field locked into a long-lived, even parity state. However, for simulation ZNVF-O, which adopted outflow vertical boundaries, the initially strong magnetic field buoyantly escaped and the disk settled down to a weakly magnetized configuration with the familiar dynamo activity (see Figure 2 of Salvesen et al., 2016a). Therefore, vertical boundaries that confine magnetic field may dictate the evolution of shearing box simulations without net poloidal flux.

Based on the discussion above, we suggest that the dynamo behavior in the Bodo et al. (2015) simulations with net vertical magnetic flux is a consequence of strong magnetization and not convection. For the zero net vertical flux simulations with impenetrable vertical boundaries, the relative roles of convection *vs.* strong magnetization in influencing the dynamo is less clear. The main result of this paper — that convection quenches azimuthal field reversals in accretion disk dynamos — applies to the case of zero net vertical magnetic flux and realistic outflow vertical boundaries. Future simulations in this regime with larger domain size will help to determine the robustness of this result.

5.5.2 Quasi-Periodic Oscillations

In addition to the outburst cycles observed in dwarf novae, cataclysmic variables in general exhibit shorter timescale variability such as dwarf nova oscillations (DNOs) on ~ 10 s time scales and quasi-periodic oscillations (QPOs) on $\sim$ minute to hour time scales (Warner, 2004). A plausible explanation for DNOs in CVs involving the disk/white dwarf

boundary layer has been proposed (Woudt & Warner, 2002; Warner & Woudt, 2002). However, a substantial number of QPOs remain unexplained. It is possible that the quasi-periodic magnetic field reversals seen in the MRI butterfly diagram are responsible for some of these QPOs and other variability. Temporally, one would expect variations from the butterfly diagram to occur on minutes to an hour timescales:

$$\tau_{\rm bf} = 223\,{\rm s} \times r_9^{3/2} \left(\frac{M}{0.6\,M_\odot} \right)^{-1/2} \frac{\tau_{\rm bf}}{10\,\tau_{\rm orb}}, \tag{5.6}$$

where $\tau_{\rm bf}$ is the period of the butterfly cycle, r_9 is the radial location of variability in units of 10^9 cm, M is the mass of the white dwarf primary, and $\tau_{\rm orb}$ is the orbital period.

Indeed, this suggestion has already been made in the context of black hole X-ray binaries (O'Neill et al., 2011; Salvesen et al., 2016b), however, no plausible emission mechanism to convert these field reversals into radiation has been identified. However, it is noteworthy that quasi-periodic azimuthal field reversals have also been seen in global accretion disk simulations with substantial coherence over broad ranges of radii (e.g. O'Neill et al., 2011; Flock et al., 2012; Jiang et al., 2014), indicating that this phenomena is not unique to shearing box simulations. If QPOs in dwarf novae are in fact associated with azimuthal field reversals, then our work here further suggests that these QPOs will differ between quiescence and outburst due to the fact that the convection quenching of field reversals (i.e. the butterfly diagram) only occurs in outburst, and this quenching may leave an observable mark on the variability of dwarf novae.

5.6 Chapter Summary

We analyzed the role of convection in altering the dynamo in the shearing box simulations of Hirose et al. (2014). Throughout this paper we explained how convection acts to:

1. quickly quench magnetic field reversals near the midplane;
2. weaken magnetic buoyancy which transports magnetic field concentrations away from the midplane;
3. prevent quasi-periodic field reversals, leading to quasi-periodic pulsations in the wings of the butterfly diagram instead; and
4. hold the parity of B_y fixed in either an odd or even state.

All of these are dramatic departures from how the standard quasi-periodic field reversals and resulting butterfly diagram work during radiative epochs.

The primary role of convection in disrupting the butterfly diagram is to mix magnetic field from high altitude (the wings) down into the midplane. This mixing was identified through correlations between entropy and B_y (see Figs. 5.5, 5.6). Due to the high opacity of the convective epochs, perturbed fluid parcels maintain their entropy for many dynamical times. Hence the observed low-entropy highly-magnetized fluid parcels found in the midplane must have been mixed in from the wings. The sign of B_y for these parcels also correspond to the wing which is closest and tend to oppose the sign found in the midplane, quenching field reversals there.

The high opacity which allows for the fluid parcels to preserve their entropy also allows for thermal fluctuations to be long lived. This combined with the turbulence generated by convection weakens the anti-correlation between magnetic pressure and density found in radiative simulations (contrast Figs. 5.4 and 5.8) and creates an environment where some flux tubes can be overdense. This acts to weaken, but not quench, magnetic buoyancy thereby preventing the weak and infrequent field reversals which do occur from propagating outwards to the wings.

It is through these mechanisms that convection acts to disrupt the butterfly diagram and prevent field reversals, even though it is clear that the MRI turbulent dynamo continues to try and drive field reversals in the midplane regions. This results in the sign of B_y and its parity across the midplane to be locked in place for the duration of a convective epoch. The quenching of field reversals and the maintenance of a particular parity (odd or even) across the midplane is a hallmark of convection in our simulations, and we hope that it may shed some light on the behavior of the MRI turbulent dynamo in general.

Chapter 6

Observational Implications

The phenomenological Disk Instability Model has been successful in reproducing the observed light curves of dwarf nova outbursts by invoking an enhanced Shakura-Sunyaev α parameter $\sim 0.1-0.2$ in outburst compared to a low value ~ 0.01 in quiescence. Recent thermodynamically consistent simulations of magnetorotational (MRI) turbulence with appropriate opacities and equation of state for dwarf nova accretion disks have found that thermal convection enhances α in disks in outburst, but only near the hydrogen ionization transition (see Hirose et al., 2014, Chapter 4). At higher temperatures, convection no longer exists and α returns to the low value comparable to that in quiescence. In order to check whether this enhancement near the hydrogen ionization transition is sufficient to reproduce observed light curves, we incorporate this MRI-based variation in α into the Disk Instability Model, as well as simulation-based models of turbulent dissipation and convective transport. These MRI-based models can successfully reproduce observed

outburst and quiescence durations, as well as outburst amplitudes, albeit with different parameters from the standard Disk Instability Models. The MRI-based model lightcurves exhibit reflares in the decay from outburst, which are not generally observed in dwarf novae. However, we highlight the problematic aspects of the quiescence physics in the Disk Instability Model and MRI simulations that are responsible for this behavior[1].

6.1 Introduction

The DIM is a well-tested model that attributes the outbursts to a thermal-viscous[2] instability that arises at temperatures where hydrogen is ionizing in the accretion disk. During quiescence, a cold dwarf nova disk accumulates matter and heats until somewhere the temperature crosses a critical value which triggers the thermal instability. This creates heating fronts which propagate into the low-temperature zones, leaving behind ionized regions. In these hot regions of the disk, the turbulence and the Shakura & Sunyaev (1973) α parameter are assumed to be enhanced, leading to an increase in angular momentum transport. This causes mass, which during quiescence had gathered mostly in the outer parts of the disk, to diffuse inwards at a high rate. The DIM is also successful in explaining soft X-ray transient outbursts observed in close binary systems containing accreting neutron stars and black holes, although X-ray irradiation of the outer disk modifies the stability criterion (van Paradijs, 1996) and plays an important

[1]The content of this chapter was first published in Coleman et al. (2016).

[2]As before, "viscosity" here and throughout this work is an effective turbulent viscosity as opposed to a true molecular viscosity.

role in extending the duration of the outburst in these systems (King & Ritter, 1998; Dubus et al., 2001).

In addition to their intrinsic interest, the observed amplitudes and time scales present in dwarf nova light curves provide the best quantitative measurements of the stresses responsible for angular momentum transport in accretion disks (King et al., 2007). It was realized early on (e.g. Mineshige & Osaki 1983; Smak 1984; Meyer & Meyer-Hofmeister 1984) that the observed outburst amplitudes can only be reproduced in the DIM if the stress parameter α takes on different values in the outburst (denoted by h for hot) and quiescent (denoted by c for cold) states, with $\alpha_{\rm h}$ being larger than $\alpha_{\rm c}$ by about a factor of ten. Modern versions of the DIM use an interpolation scheme between constant values of $\alpha_{\rm h}$ and $\alpha_{\rm c}$ in the outburst and quiescent states, but this does not imply that α is necessarily constant for all high or for all low temperatures[3]. Detailed fits of the DIM to the observed correlations between orbital period (or, equivalently, outer disk radius) and the outburst duration and decay rate in normal, U Gem-type systems and normal outbursts of SU UMa systems, give values for $\alpha_{\rm h}$ of between 0.1 and 0.2, and certainly rule out significantly smaller values (Smak, 1999; Kotko & Lasota, 2012). Moreover, only such high values are able to explain the observed linear relationship between outburst amplitude and the logarithm of outburst recurrence time (the Kukarkin-Parenago relation; Kotko & Lasota 2012).

Ever since the first application of the magnetorotational instability (MRI) to accretion disks (Balbus & Hawley, 1991; Hawley & Balbus, 1991), it has been widely suspected that

[3]E.g. Mineshige & Wheeler (1989) used $\alpha \sim (H/R)^{1.5}$.

both angular momentum transport and dissipation of mechanical energy is mediated by MRI turbulence, at least if the disk is sufficiently electrically conducting. The accretion stress is due to correlations between radial and azimuthal magnetic field fluctuations, as well as radial and azimuthal velocity fluctuations (e.g. Balbus & Hawley 1998). One can measure this stress directly from numerical simulations of the turbulence. Equivalent values of the α parameter can then be derived by scaling this stress with the average thermal pressure.

Because the values of α are among the most fundamental ways of confronting MRI turbulence with observations, many groups have measured these values from their simulations. In the absence of net vertical magnetic flux, local shearing box simulations that incorporate vertical gravity generally give time-averaged α values of around two or three percent (Hirose et al., 2006; Davis et al., 2010; Shi et al., 2010; Guan & Gammie, 2011; Simon et al., 2012). Global simulations without net vertical flux of the entire disk, but which allow for large scale field loops that can produce local vertical magnetic fluxes threading the disk, also so far produce comparably small values of α (Sorathia et al., 2010; Hawley et al., 2011; Sorathia et al., 2012), though more work needs to be done in exploring the effects of various field topologies.

A number of suggestions have been made as to how to resolve the discrepancy between the high values of α inferred from dwarf novae in outburst, and these low values measured in MRI simulations. First, it has been known for some time that shearing box simulations with no vertical gravity have stronger α values when the box is threaded by a vertical

magnetic field, and the resulting α increases with magnetic field strength so long as the critical vertical wavelength of the MRI lies within the box (Hawley et al., 1995; Sano et al., 2004; Pessah et al., 2007).[4] Because the initial total vertical magnetic flux is necessarily conserved in shearing box simulations, this would appear to require imposing a net external vertical magnetic field in the disk from the outside in order to increase the value of α in outburst states. This might result from the magnetic field of the companion star, although one would then have to explain why the resulting value of α is so universal in the outburst state.

On the other hand, the increase in local stress with *local* vertical magnetic flux has been confirmed in global simulations with no overall net vertical magnetic flux, although the global disk still has a low value of α when averaged over the entire disk (Sorathia et al., 2010). Having net vertical flux may also drive magnetocentrifugal winds, which can also extract angular momentum from the disk (Suzuki & Inutsuka, 2009; Fromang et al., 2013; Lesur et al., 2013; Bai & Stone, 2013). In addition to the vertical magnetic field, transient phases such as those caused by the dwarf nova outbursts themselves may also produce periods of enhanced α that are similar to that observed in transient magnetic field growth phases in global simulations (Sorathia et al., 2012).

Even without vertical magnetic field or transient behavior, however, radiation MHD stratified shearing box simulations that incorporate a realistic equation of state and opacities near the hydrogen ionization transition reproduce thermal equilibria resembling

[4]Recent work by Shi et al. (2016) has also shown that the value of α in shearing boxes with no vertical magnetic field or vertical gravity is sensitive to the height of the box: taller boxes produce significantly higher values of α.

the stable upper and lower branches of the local "S-curve" of the DIM (Hirose et al., 2014). As in previous MRI simulations, α values of a few percent generally result, but α dramatically increases as one approaches the lower end of the upper branch. This appears to be due to the onset of intermittent vertical convection caused by the large increase in opacity near the ionization transition. The resulting vertical motions at the beginning of the convective episodes build up vertical magnetic field, which may be seeding the axisymmetric MRI. In addition, temporal phase differences between the variations of stress and pressure may also be increasing the time-averaged α.[5] These simulations therefore reproduce the observed high values of α on the upper branch of the S-curve, but only near the low-temperature end of the upper branch.

In addition to the variations of α on the upper branch, there are significant differences in the time-averaged vertical structure observed in the simulations and the standard assumptions used in the DIM. First, the DIM generally assumes that the stress to pressure ratio is constant with height, so that the dissipation rate per unit volume is proportional to pressure. MRI simulations, on the other hand, generally produce a more extended vertical dissipation profile (Turner, 2004; Hirose et al., 2006). Moreover, the simulated upper, near-photosphere layers are generally supported against the vertical tidal gravity by magnetic forces, not thermal pressure forces (Miller & Stone, 2000; Hirose et al., 2006), in contrast to the DIM vertical structure models. Finally, as we have just discussed, vertical transport of heat in the simulations is caused by alternating episodes of radiative

[5]Persistent convection can also enhance α, provided the Mach numbers of the convective motions exceed ~ 0.01 (Hirose, 2015).

diffusion and thermal convection, at least near the end of the upper branch. The DIM incorporates the possibility of convection using mixing length theory, but it is not clear that this prescription adequately describes what is happening in the MRI simulations.

The primary purpose of this paper is to incorporate the variation of α measured in the MRI simulations into the DIM, to see whether an enhancement of α just near the end of the upper branch is sufficient to reproduce the observed amplitudes and time scales in dwarf nova outburst light curves. A secondary objective is to use the dissipation and heat transport observed in the simulations to produce more physics-based vertical structure models that can be incorporated in the DIM.

6.2 MRI Simulation-Based Stress Prescription

As discussed in the introduction, the ratio of vertically averaged stress to vertically averaged thermal pressure, α, can be inferred from observations and can be measured directly from simulations. The difference in α between the lower and upper branches of the S-curve has been crucial for getting DIMs to produce realistic light curves. In the standard version of the DIM two values of alpha were used; $\alpha_{\rm h} \sim 0.1$ for the hot, ionized upper branch, and $\alpha_{\rm c}$, 4 to 10 times smaller, for the lower branch, with some smooth and rapid transition between them. In particular, our modeling of the standard DIM here in this paper will use a slightly modified version of the prescription first introduced by

Hameury et al. (1998):

$$\log(\alpha) = \log(\alpha_{\rm c}) + [\log(\alpha_{\rm h}) - \log(\alpha_{\rm c})] \left[1 + \left(\frac{T_{\rm c0}}{T_{\rm c}}\right)^{16}\right]^{-1}, \tag{6.1}$$

where $T_{\rm c}$ is the central (midplane) temperature and $T_{\rm c0}$ is a critical temperature. The choice of this parameter is somewhat arbitrary and we take $T_{\rm c0} = 2.9 \times 10^4$ K (Lasota et al., 2008), and take the limiting α-parameters to be $\alpha_{\rm c} = 0.03$ and $\alpha_{\rm h} = 0.12$.

Until recently, local shearing box MRI simulations (without net vertical flux through the simulation domain) produced values of α which are too low for the hot ionized outburst state of dwarf novae. However, for the first time, α measured in local MRI simulations (Hirose et al., 2014) appear to be consistent with α values inferred from observations and commonly used to reproduce dwarf novae outbursts by the DIM. Hirose et al. (2014) found that the α parameter varies along the S-curve and is not constant on the upper branch, with an enhancement of α towards the tip (low temperature end) of the upper branch. This provides an intriguing replacement for the previous ad hoc bimodal α prescription previously used (e.g. Hameury et al., 1998; Lasota, 2001; Kotko & Lasota, 2012).

The Hirose et al. (2014) simulations are done in the geometry of a vertically stratified shearing box, in which a small local patch of an accretion disk is approximated as a co-rotating Cartesian frame (x, y, z) with linearized Keplerian shear flow $-(3/2)\Omega x$, where x, y, and z correspond to the radial, azimuthal, and vertical coordinates, respectively (Hawley et al., 1995). The simulations assume no explicit shear viscosity in the basic equations, and no Ohmic, Hall, or ambipolar diffusion effects are included either, i.e. ideal

MHD is assumed. The simulations are therefore probably not accurate for the quiescent, largely electrically neutral state where Ohmic dissipation and the Hall effect are likely important (see Appendix 7.3). Magnetic and kinetic energy losses at the grid scale are captured and added to the local internal energy of the gas, creating an effective turbulent dissipation (Turner et al., 2003b; Hirose et al., 2006). Additionally, the simulations include realistic equation of state and opacity tables in order to accurately model the hydrogen ionization regime (see Hirose et al., 2014, for details), and the flux limited diffusion approximation (which breaks down at low optical depths) is used to model radiation transport and cooling.

The simulations in Hirose et al. (2014) were computed for only one angular frequency $\Omega = 6.4 \times 10^{-3}$ s^{-1}, which corresponds to a distance[6] of $1.25{\times}10^{10}$ cm from a white dwarf of $0.6M_{\odot}$. In order to explore a larger parameter space, we utilize the same methods to run simulations at two additional orbital radii, 1.25×10^{9} cm and 4.13×10^{9} cm. The parameters for these additional simulations can be found in Table 3.2.

We incorporate simulation data into the DIM's vertical thermal equilibrium equations (Hameury et al., 1998) by first discarding the initial 10 orbits of data (this is the time it take for turbulence to develop and erase details of the initial conditions) and taking a time average of the remaining duration of the simulations. All the simulations have been run long enough so that at least 100 orbits (and up to 220 orbits) of data are included in the time averaging. This ensures that averaging is done over many thermal times so that

[6]Due to some rounding differences our distance slightly differs from the 1.23×10^{10} cm that Hirose et al. (2014) state.

thermal fluctuations are smoothed out and that the average is well behaved (i.e. running the simulation for another 10 orbits would have little effect on the time average). We also horizontally average the data over the radial (x) and azimuthal (y) directions. Finally, we vertically symmetrize the data about the midplane $z = 0$. Simulation data which have undergone these operations will henceforth be referred to as profiles. To summarize, for some scalar data f the profile is calculated as follows

$$f(z) \equiv \frac{\iiint \left[f(x,y,z,t) + f(x,y,-z,t)\right] \, \mathrm{d}x \, \mathrm{d}y \, \mathrm{d}t}{2 \iiint \mathrm{d}x \, \mathrm{d}y \, \mathrm{d}t}. \tag{6.2}$$

We then fit some of these profiles in order to produce vertical structures that more accurately represent simulation physics than the standard DIM.

The parameter α is computed from each simulation as follows

$$\alpha \equiv \frac{\int w_{xy}(z) \, \mathrm{d}z}{\int \left[P_{\mathrm{gas}}(z) + P_{\mathrm{rad}}(z)\right] \mathrm{d}z}, \tag{6.3}$$

where w_{xy} is the sum of the Maxwell and Reynolds stresses

$$w_{xy} \equiv -\frac{B_x B_y}{4\pi} + \rho v_x \delta v_y. \tag{6.4}$$

Here B_x and B_y are the radial and azimuthal components of the magnetic field respectively[7], v_x is the radial velocity, and $\delta v_y \equiv v_y + 3\Omega x/2$ is the difference between the azimuthal velocity and the mean rotational velocity in the disk. We also examined how the temporal mean of α varies with time and we found these fluctuations diminished with time, indicating that the time averaged α is well behaved. Provided the time average is

[7]Note that the magnetic fields as defined here differ by a factor of $\sqrt{4\pi}$ from the magnetic fields defined in the simulations. Here we use standard cgs Gaussian units.

done over an interval of at least 100 orbits, differences in the time-averaged value of α within a single simulation are less than ten percent.

We fit the variation of α between all the simulations at radius $r = 1.25 \times 10^{10}$ cm with a prescription depending only on local effective temperature $T_{\rm eff}$ of the following form

$$\alpha = a \exp\left(-\frac{x^2}{2}\right) + \frac{b}{2}\tanh(x) + c, \tag{6.5}$$

$$x = \frac{T_{\rm eff} - T_0}{\sigma}. \tag{6.6}$$

The best fit parameter values are $a = 8.79 \times 10^{-2}$, $b = 2.41 \times 10^{-3}$, $c = 3.27 \times 10^{-2}$, $T_0 = 7034$ K, and $\sigma = 1000$ K. Figure 6.1 compares this fit to the simulation data at this radius. Also shown are the results from simulations at two additional radii (which are not included in the fit), which are also reasonably consistent with this fit, though there is some indication that the simulations at smaller radii have slightly greater convective enhancements of α. We will use the fit of equations (6.5) and (6.6) in the simulation-based light curve modeling below.

6.3 MRI Simulation-Based Vertical Structure Models

In addition to the overall behavior of the stress to pressure ratio α discussed in the previous section, MRI simulations also exhibit differences with the standard DIM assumptions

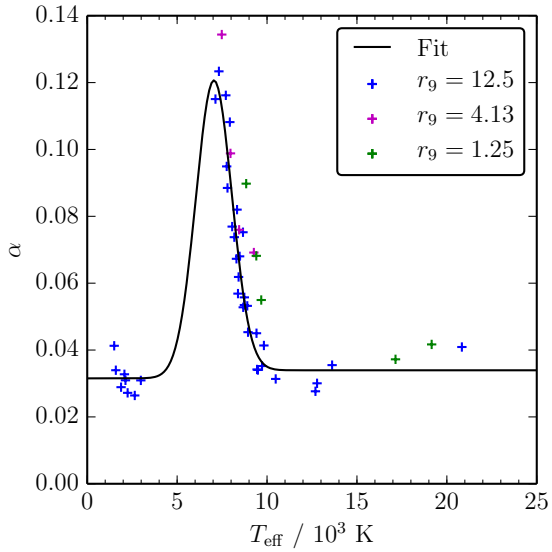

Figure 6.1 Time averaged α versus effective temperature for all the MRI simulations at three different radii around a $0.6M_\odot$ white dwarf: $r = 1.25\times10^{10}$ cm (blue crosses), $r = 4.13\times10^{9}$ cm (magenta crosses), and $r = 1.25\times10^{9}$ cm (green crosses). The best fit curve for the $r = 1.25\times10^{10}$ cm simulations is plotted in black.

concerning the local vertical structure of the disk. Here we utilize data from the Hirose et al. (2014) vertically stratified shearing box MHD simulations to show how to make DIM vertical structure models that better reflect some of the actual properties of the turbulence observed in the simulations.

6.3.1 Dissipation Profile

Previously the DIM has relied on an ad hoc assumed vertical profile of turbulent dissipation, in particular a *vertically local* α prescription in which the dissipation rate per unit volume is proportional to the local thermal pressure. This is very different from what is observed in vertically stratified MRI simulations. Such simulations of course cannot

spatially resolve the actual microscopic viscous and resistive length scales in the plasma, and the simulations of Hirose et al. (2014) do not include any explicit resistivity or shear viscosity in the basic equations. Instead, a total energy scheme is employed in which grid scale losses of magnetic and kinetic energy are automatically transferred to internal energy of the plasma, thereby effecting a dissipation of turbulent mechanical energy. This will capture the true dissipation rate in the turbulence provided the turbulent cascade that would exist in reality below the grid scale is capable of transferring most of the energy down to the true microscopic dissipation scales. Whether this accurately captures the dissipation occurring in real disks in nature remains to be seen.

In fact, there is strong numerical evidence that the saturation level of the turbulent stresses, and even whether long-lived turbulence can be maintained, depends on the values of the fluid and magnetic Reynolds numbers or their ratio, the magnetic Prandtl number. This is particularly true of shearing box simulations that lack vertical gravity (e.g. Fromang et al. 2007; Lesur & Longaretti 2007). Including vertical gravity appears to slightly extend the range of magnetic Prandtl numbers that allow sustained turbulence to lower (but still greather than unity) values (Davis et al., 2010). This is also true of shearing box simulations which lack vertical gravity, provided the box height is large enough (Shi et al., 2016). Because the simulations used here have no explicit viscosity or resistivity, and dissipation effectively occurs at the grid scale, the effective magnetic Prandtl number must be of order unity. While the simulations nevertheless exhibit sustained turbulence, more work needs to be done to investigate whether and how the

dissipation profiles, and even the saturation level of the turbulence, might be affected by the actual dissipation scales. Dependencies of the turbulent stresses on magnetic Prandtl number may even themselves lead to thermal instabilities in accretion disks (Potter & Balbus, 2014).

In any case, as shown in Figure 6.2, the time and horizontally-averaged vertical profile of dissipation rate per unit volume in the simulations is not proportional to the pressure, in contrast to the simple assumption used in the DIM. In fact, the vertical dissipation profile generally does not even decline monotonically away from the midplane, but instead peaks off the midplane, possibly due to the effects of magnetic buoyancy (Blaes et al., 2011). Despite this non-monotonic behavior, we find that we can adequately replace the usual DIM assumption of dissipation rate per unit volume Q^+ being simply proportional to thermal pressure with, instead, a power law dependence on thermal pressure (see Figure 6.2):

$$\frac{Q^+}{Q_0^+} = \left(\frac{P}{P_0}\right)^{\delta}, \tag{6.7}$$

where the subscript zero is used to denote midplane values. By thermal pressure P, we mean the sum of gas pressure ($P_{\rm gas}$) and the much smaller radiation pressure ($P_{\rm rad} \ll P_{\rm gas}$), but we exclude magnetic pressure, which typically dominates the thermal pressure far from the midplane. Using linear regression (in log space) we determined that the best fit exponent $\delta = 0.35$. The ratio Q_0^+/P_0^δ is chosen such that the vertically integrated Shakura & Sunyaev (1973) α relation holds:

$$\frac{3}{2}\alpha\Omega \int_{-\infty}^{\infty} P(z)\ \mathrm{d}z = \int_{-\infty}^{\infty} Q^+(z)\ \mathrm{d}z. \tag{6.8}$$

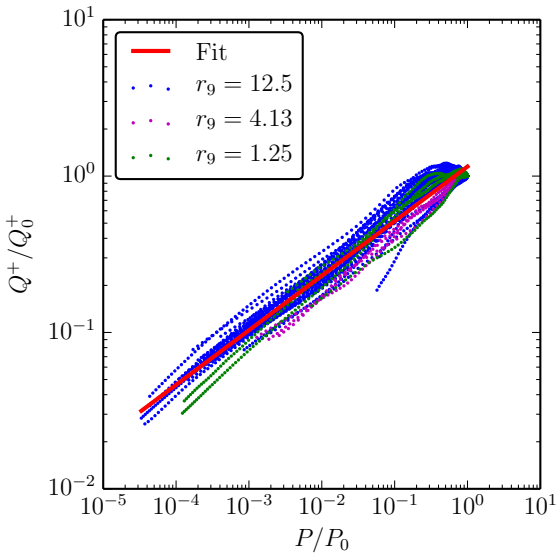

Figure 6.2 Time and horizontally averaged profiles of dissipation rate per unit volume as a function of thermal pressure, each scaled by their respective midplane values, for each of the MRI simulations used in this paper. The different colors refer to simulations done at three different radii around a $0.6M_{\odot}$ white dwarf: $r = 1.25\times10^{10}$ cm (blue points), $r = 4.13\times10^{9}$ cm (magenta points), and $r = 1.25\times10^{9}$ cm (green points). A power law fit to all the profiles is also plotted (red line). Note that the slope of the fit is significantly more important than the vertical offset, which we determine in our light curve modeling by enforcing energy conservation using equation (6.8).

6.3.2 Non-Equilibrium Dissipation

During the passage of a heating or cooling front through the disk, annuli at the location of the fronts are of course out of thermal equilibrium. Within the DIM (Hameury et al., 1998), this is handled by constructing hydrostatic vertical structures with a local vertical energy flux divergence given by

$$\frac{dF_z}{dz} = \frac{3}{2}\alpha_{\rm eff}\Omega P(z), \tag{6.9}$$

where $P(z)$ is the local thermal pressure and $\alpha_{\rm eff}$ is a parameter that differs from α when the annulus is not in thermal equilibrium, both because vertically integrated heating and cooling will then no longer be equal and because of the concomitant vertical thermal expansion or contraction. The actual value that $\alpha_{\rm eff}$ takes is determined by solving for the complete vertical structure for a given effective temperature and surface mass density. If thermal equilibrium does hold, then $\alpha_{\rm eff} = \alpha$, and we recover the standard DIM assumption that the dissipation rate per unit volume is proportional to the local thermal pressure at every height in the annulus.

As just noted, the time and horizontally averaged vertical profiles of dissipation rate per unit volume measured in the MRI simulations do not simply scale with local thermal pressure. We therefore modify equation (6.9) to be consistent with our fit to the equilibrium dissipation profile, equation (6.7):

$$\frac{dF_z}{dz} = \frac{3}{2}\alpha_{\rm eff}\Omega P_0 \left(\frac{P(z)}{P_0}\right)^{\delta}. \tag{6.10}$$

However, it is not obvious that the MRI simulations should behave according to this equation outside thermal equilibrium.

If the assumption of equation (6.10) were perfect, then all simulation data would fall directly on the best-fit line in Figure 6.2. While time averaged profiles lie near this line, it is not apparent that one should expect this behavior from a thermally evolving simulation. To test this we defined

$$\alpha_{\rm eff}(z,t) \equiv \frac{2}{3}\frac{1}{\Omega P_0}\frac{\partial F_z}{\partial z}\left(\frac{P_0}{P}\right)^{\delta}, \tag{6.11}$$

with $\delta = 0.35$ as previously discussed, and examined variations in $\alpha_{\rm eff}$ for a few simula-

tions (see Figures 6.3-6.5). In addition to stable simulations (e.g. ws0446 shown in Figure 6.3), we specifically examined two non-equilibrium simulations: one heating (ws0467, see Figure 6.4), and one cooling (ws0488, see Figure 6.5). These simulations were started just beyond the edges of the lower and upper branches of the S-curve, respectively (see Figure 11 of Hirose et al. 2014). As these two simulations evolve, they move around on the plane of $T_{\rm eff}$ vs. total column mass density Σ, which allows $\alpha_{\rm eff}$ to vary with time. However, $\alpha_{\rm eff}$ should be approximately constant in height at a given time if equation (6.10) is to adequately describe the simulation behavior. With the exception of variations near and outside the photospheres, this seems to be a reasonable approximation for simulations ws0446 and ws0467. There are some clear issues for the cooling simulation ws0488 just below the photosphere (see Figure 6.5), which manifest as asymmetric regions of enhanced $\alpha_{\rm eff}$. It is possible that these regions arise from asymmetric cooling/collapsing of the disk, which is not possible to incorporate into the DIM and show a clear limitation of our strategy. However, outside these regions, ws0446 and ws0488 show comparable variations, signifying that this approach is not unreasonable.

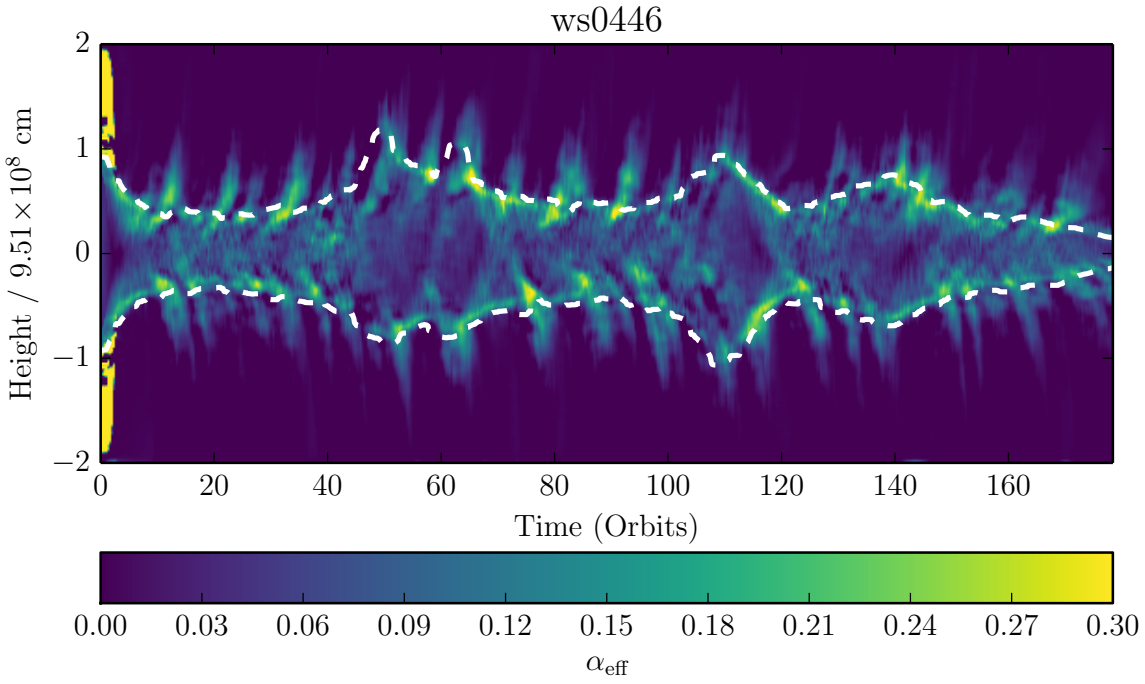

Figure 6.3 Horizontally averaged α_{eff} for simulation ws0446, a stable convective simulation. The horizontal axis is time in orbits, and the vertical axis is height. The white dashed contours are the photospheres. The data has been smoothed with a two orbit running boxcar.

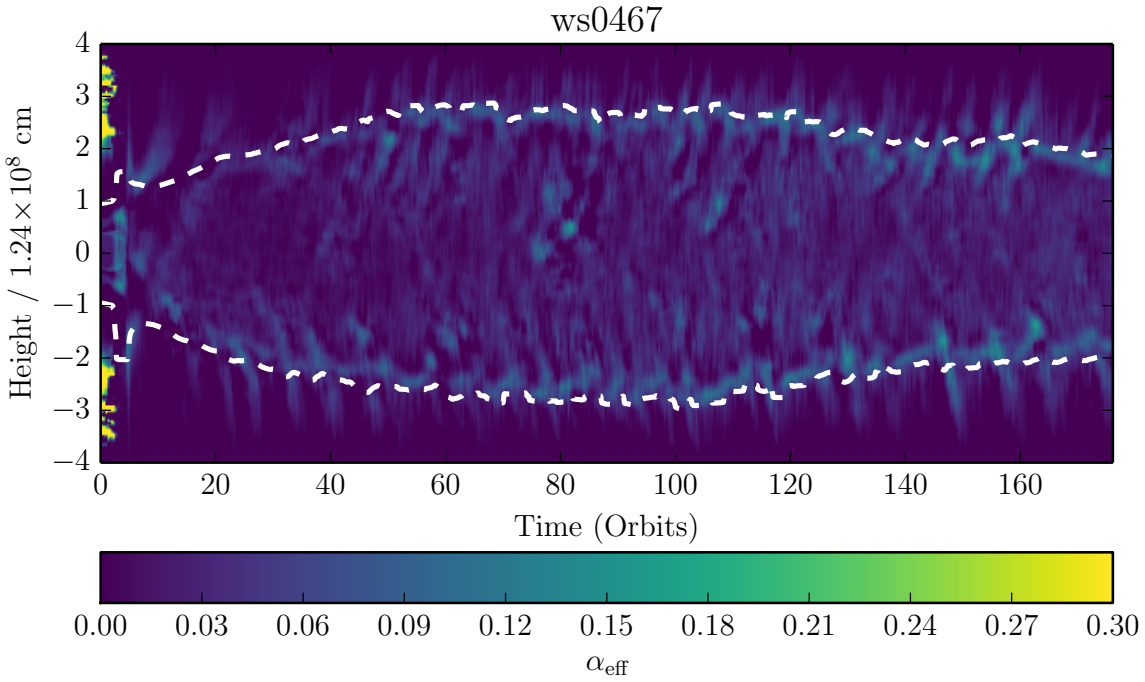

Figure 6.4 Horizontally averaged $\alpha_{\rm eff}$ for simulation ws0467, an unstable simulation that undergoes runaway heating until significant mass loss occurs through the vertical boundaries. The horizontal axis is time in orbits, and the vertical axis is height. The white dashed contours are the photospheres. The data has also undergone two orbit boxcar smoothing. This simulation exhibits continuous convective vertical transport of heat.

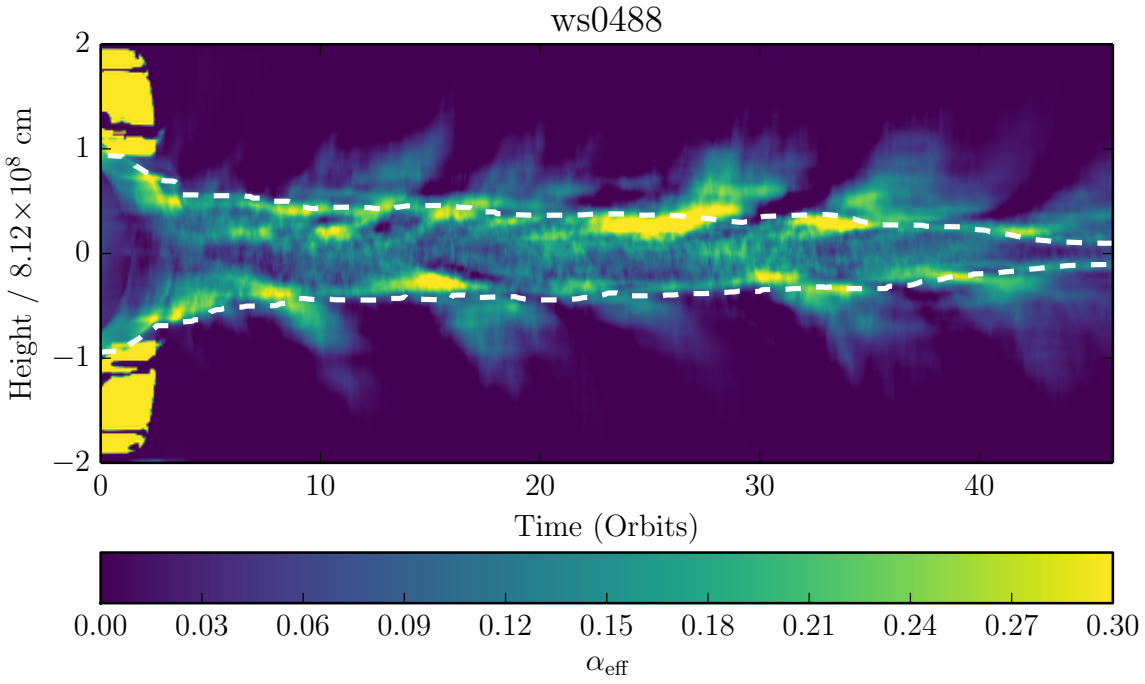

Figure 6.5 Horizontally averaged α_{eff} for simulation ws0488, an unstable simulation that undergoes runaway cooling. The horizontal axis is time in orbits, and the vertical axis is height. The white dashed contours are the photospheres. The data has also undergone two orbit boxcar smoothing.

6.3.3 Mixing Length Theory

The vertical temperature profile is computed in the DIM according to

$$\nabla \equiv \frac{\mathrm{d}\ln T}{\mathrm{d}\ln P} = \begin{cases} \nabla_{\mathrm{rad}} & \text{if } \nabla_{\mathrm{rad}} \leq \nabla_{\mathrm{ad}} \\ \nabla_{\mathrm{conv}} & \text{if } \nabla_{\mathrm{rad}} > \nabla_{\mathrm{ad}} \end{cases} \tag{6.12}$$

$$\nabla_{\mathrm{rad}} \equiv \frac{3\kappa\rho H_p F_{\mathrm{tot}}}{16\sigma T^4}, \tag{6.13}$$

where ∇_{rad} and ∇_{ad} are the standard radiative and adiabatic temperature gradients, respectively, ∇_{conv} is the convective temperature gradient computed using mixing length theory (Paczyński, 1969; Hameury et al., 1998), κ is the Rosseland mean opacity, H_P is the pressure scale height, and F_{tot} is the total flux passing through a given height. Through trial and error we determined that using a value of six for the mixing length parameter ($\alpha_{\mathrm{ml}} = 6$) produced vertical structure models which closely resemble the time and horizontally averaged vertical profiles measured in the MRI simulations that exhibit convection (see Figure 6.6). This is compared to the much lower and more conventional value of 1.5 used in the DIM by Hameury et al. (1998). We note that if the mixing length theory is to be taken at face value then $\alpha_{\mathrm{ml}} = 6$ implies that the length scale of convective eddies is several (~ 6) times larger than the pressure scale height of the disk, which seems unphysical.

However, it is important to note that this value of the mixing length parameter actually reflects the fact that when convection occurs in the simulations, it does so

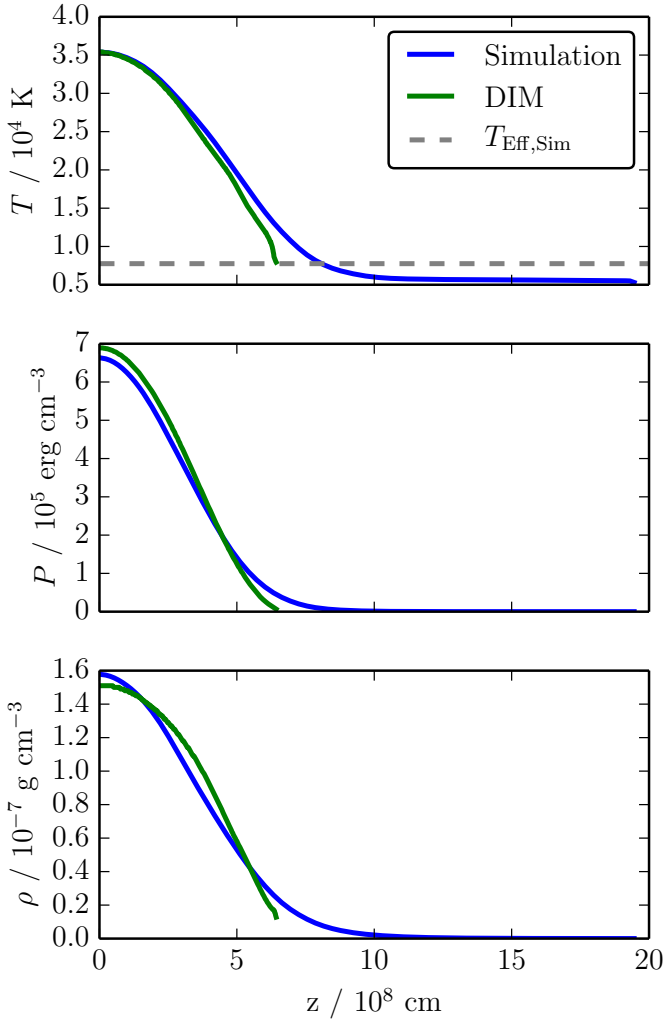

Figure 6.6 Comparison of vertical structure model to a convective simulation (ws0441) with $r = 1.25 \times 10^{10}$ cm. Profiles of temperature (top), thermal pressure (middle), and mass density (bottom) are plotted verses z for profiles measured from the simulation (blue) and vertical structure models (green). In these plots, it is clear that the simulations extend further than our models. This is because our DIM vertical structures use the photosphere as a vertical boundary condition and terminate there. This means the minimum temperature in the vertical structure model is also the effective temperature. The time averaged effective temperature of the simulation is plotted as the dashed gray horizontal line, showing good agreement between our modified DIM and the simulations.

intermittently. This intermittency is the result of a limit cycle, operating on timescales of ~ 10 thermal times, which is driven by the interplay of temperature dependent opacities and enhancement of stress by convective turbulence (see Section 3.4 of Hirose et al., 2014, for further discussion). Averaging over this time dependent cycle results in a high effective $\alpha_{\rm ml}$, but the time dependent $\alpha_{\rm ml}$ tend to have more canonical values of ~ 1 when convection is occurring. By measuring the horizontally-averaged convective heat flux $F_{\rm conv}$ directly from the simulations, we compute the mixing length parameter $\alpha_{\rm ml}$ that would produce this flux as a function of height and time. We accomplished this by solving the following equations using the Newton-Raphson method:

$$\alpha_{\rm ml}^2 \beta^{3/2} = \frac{2F_{\rm conv}}{C_P \rho u T}, \tag{6.14}$$

where

$$u \equiv \sqrt{-\frac{g_z H_P}{8}\left(\frac{\partial \ln \rho}{\partial \ln T}\right)_P}, \tag{6.15}$$

$$H_P \equiv -\mathrm{sign}(z)\frac{\partial z}{\partial \ln P}, \tag{6.16}$$

$\beta \equiv (\nabla - \nabla')$ is the positive root of the quadratic

$$\beta = (\gamma_0 \alpha u)^2 \left(\nabla - \nabla_{\rm ad} - \beta\right)^2, \tag{6.17}$$

and

$$\gamma_0 \equiv \frac{C_P \rho}{8\sigma T^3 \theta},\ \theta \equiv \frac{3\tau}{3+\tau^2},\ \tau \equiv \alpha_{\rm ml}\kappa\rho H_P. \tag{6.18}$$

Note that β and γ_0 are implicit functions of $\alpha_{\rm ml}$. $F_{\rm conv}$, C_P, ρ, T, $g_z = -\Omega^2 z$, H_P, ∇, $\nabla_{\rm ad}$, and κ are read or computed from the MHD simulations. These variables are then

horizontally averaged and smoothed by 1 orbit in time before $\alpha_{\rm ml}$ is computed.

The results are shown in Figure 6.7. The epochs that are white at all heights in this figure are epochs when radiative diffusion dominates, and there is little vertical convective transport of heat. Most of the epochs that are actually convective have very reasonable values of $\alpha_{\rm ml}$ that are of order unity. It is generally only near the epochs that are radiative that $\alpha_{\rm ml}$ takes on substantially larger values.

The vertical profiles of the simulation data shown in Figure 6.6 average over both the convective and radiative epochs, so it is not surprising, given the behavior shown in Figure 6.7, that unusually large mixing length parameters are required to describe these profiles with a pure convective transport treatment.

From the discussion here it is clear that time averaging the intermittent convection obscures some of the physics discovered in the MRI simulations of Hirose et al. (2014). It is unclear how much this simplification affects the outcome. The duration of the convective limit cycle is ~ 50 orbits, so for timescales $\gtrsim 1$ day, this averaging procedure should be a reasonable approximation. It is during the rapid transition from quiescence to outburst that this simplification becomes questionable, making the inability of the DIM to capture this time dependent behavior a clear limitation, but nothing better can be done in the framework of the standard DIM.

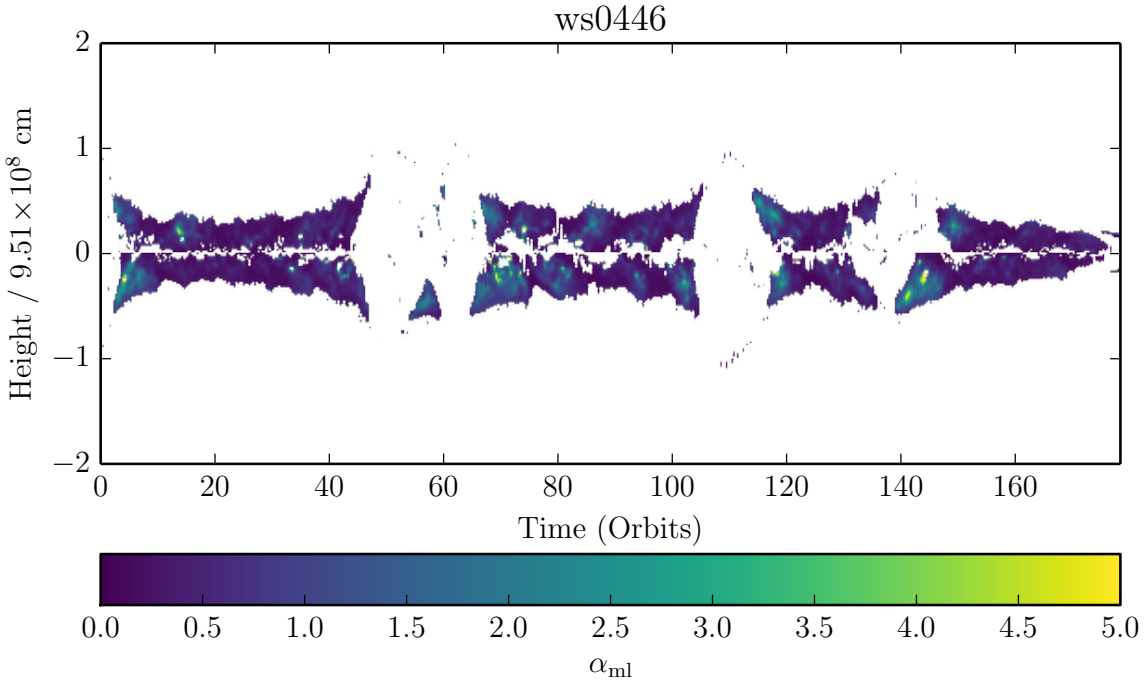

Figure 6.7 Convective mixing length parameter $\alpha_{\rm ml}$ computed locally from horizontally-averaged simulation data for upper branch simulation ws0446 from Hirose et al. (2014), as a function of height and time. The $\alpha_{\rm ml}$ data (already computed from quantities smoothed over 1 orbit) has been smoothed by an additional 0.2 orbits in time to improve clarity. White regions within two pressure scale heights are either convectively stable, or are regions for which our Newton-Raphson method to solve equations (6.14)-(6.18) failed to converge within 100 iterations. Data outside two pressure scale heights are discarded. The white gaps approximately centered on the 55 orbit, 110 orbit, and 140 orbit epochs are times when radiative diffusion dominated convection in the vertical transport of heat.

6.3.4 Summary of MRI Simulation-Based Vertical Structure Equations and Boundary Conditions

The DIM framework uses the thermal pressure to provide both the vertical hydrostatic support and to specify the vertical dissipation profile. In the simulations, magnetic pressure support can dominate thermal pressure near the photosphere, although the magnetic to thermal pressure ratio is at most $1.5\alpha \lesssim 20\%$ near the midplane. Including magnetic pressure in a single pressure framework is complicated, as it requires a modification of the alpha relation (equation 6.8) and it complicates the temperature gradient (equation 6.12) used in mixing length theory. We have therefore neglected this additional aspect of the simulation physics. Additionally, the DIM uses different, albeit similar, equation of state and opacity tables.

With our modifications to the DIM our vertical structure equations become

$$\frac{\mathrm{d}\,P}{\mathrm{d}\,z} = -\rho\Omega^2 z \tag{6.19}$$

$$\frac{\mathrm{d}\,\varsigma}{\mathrm{d}\,z} = 2\rho \tag{6.20}$$

$$\frac{\mathrm{d}\ln T}{\mathrm{d}\ln P} = \nabla \tag{6.21}$$

$$\frac{\mathrm{d}\,F_z}{\mathrm{d}\,z} = Q^+ = A_0\Omega P_0 \left(\frac{P}{P_0}\right)^{\delta} \tag{6.22}$$

$$A_0 = \frac{3}{2}\alpha \frac{P_0^{\delta-1}\int_0^\infty P\,\mathrm{d}z}{\int_0^\infty P^\delta\,\mathrm{d}z}, \tag{6.23}$$

where $\varsigma(z)$ is the surface mass density between $\pm z$, and ∇ is determined by equation (6.12). Equations (6.22) and (6.23) are equivalent to our dissipation fit and the alpha

relation (equations 6.7 and 6.8, respectively). Our midplane boundary conditions are

$$z = 0 \tag{6.24}$$

$$F_z = 0 \tag{6.25}$$

$$\varsigma = 0 \tag{6.26}$$

$$T = T_0 \tag{6.27}$$

$$P = P_0, \tag{6.28}$$

and our exterior boundary conditions are

$$\kappa_R P = \frac{2}{3}\Omega^2 z \tag{6.29}$$

$$F_z = \sigma T^4 \tag{6.30}$$

$$\varsigma = \Sigma, \tag{6.31}$$

where κ_R is the Rosseland mean opacity.

6.3.5 Thermal equilibria: the S-curves

Before presenting outburst light curves based on the physical models discussed in the previous two sections we briefly discuss the properties of the disk's thermal equilibria. We consider two MRI-based models, DIMa and DIMRI, and compare them to the standard DIM. DIMa adopts the same vertical structure assumptions as the standard DIM, but

uses the MRI-based $\alpha(T_{\rm eff})$ prescription of equations (6.5)-(6.6) discussed in section 2. DIMRI also uses this MRI-based α prescription, combined with the MRI-based vertical structure equations (6.19)-(6.31) summarized in section 6.3.4. Figure 6.8 illustrates the differences in the S-curves produced by these models at radius $R = 1.25 \times 10^{10}$ cm around a $0.6 M_{\odot}$ white dwarf.

The most important parameters emerging from the S-curves shown in Figure 6.8 are the critical surface mass densities ($\Sigma^{+}_{\rm crit}$, $\Sigma^{-}_{\rm crit}$) and effective temperatures ($T^{+}_{\rm eff,crit}$, $T^{-}_{\rm eff,crit}$) at the ends of the (upper, lower) branches, marking the points where (cooling, heating) transitions occur. In particular, the quotient of critical surface mass densities, $Q\Sigma_{\rm crit} \equiv \Sigma^{-}_{\rm crit}/\Sigma^{+}_{\rm crit}$, plays an important role in determining the shape of the outburst lightcurve. It is therefore worth noting that $Q\Sigma_{\rm crit}$ is different for all of the S-curves, with DIM having the largest $Q\Sigma_{\rm crit}$. Despite our efforts, there is still a basic discrepancy between the actual MRI simulation data and the DIMRI S-curve in Figure 6.8. Both branches of the simulation S-curve extend a little further in Σ, leading to a larger $Q\Sigma_{\rm crit}$ compared to that of DIMRI, and $T^{-}_{\rm eff,crit}$ is significantly larger in DIMRI on the lower branch. The mismatch on the upper branch can be explained by our choice of $\alpha_{\rm ml} = 6$. As an annulus in outburst approaches the critical point ($\Sigma^{+}_{\rm crit}$, $T^{+}_{\rm eff,crit}$) the role of convection increases and presumably $\alpha_{\rm ml} = 6$ becomes increasingly less adequate. This is because the high value of $\alpha_{\rm ml}$ that we adopt is due to radiative diffusion dominated episodes in the intermittent convection, which become less prominent as the annulus reaches the end of the upper branch. One possible solution would be to decrease $\alpha_{\rm ml}$ towards the tip of

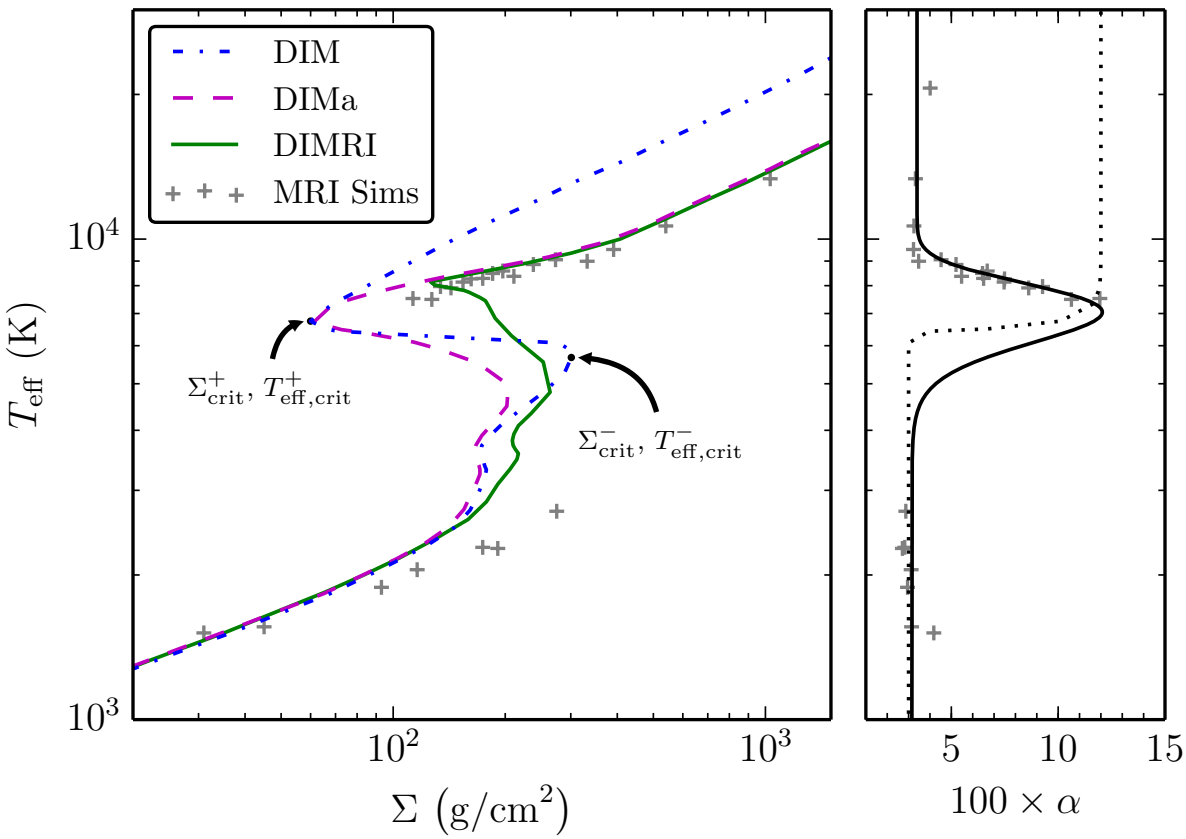

Figure 6.8 Left: Loci of thermal equilibria in the $T_{\rm eff}$ vs. surface mass density Σ plane (the "S-curve") at radius $R = 1.25 \times 10^{10}$ cm for the standard DIM (blue), DIMa (magenta) and DIMRI (green). The MRI simulation results are gray crosses (one point for each stable simulation). Additionally, the critical points ($\Sigma^+_{\rm crit}$, $T^+_{\rm eff,crit}$) and ($\Sigma^-_{\rm crit}$, $T^-_{\rm eff,crit}$) are marked for DIM. Right: The MRI-based $\alpha\,(T_{\rm eff})$ fit from Figure 6.1 plotted sideways in solid black (DIMa and DIMRI both use this fit) with the results from the same MRI simulations from the left plotted as gray crosses. Equation (6.1) for the standard DIM, with $\alpha_{\rm c} = 0.03$ and $\alpha_{\rm h} = 0.12$, is plotted as the dotted black line.

the upper branch in the DIMRI, and this may be worth exploring in the future. We show how adopting a smaller constant value of $\alpha_{\rm ml}$ in DIMRI affects the outburst lightcurves below.

There are several issues which contribute to the mismatch between the simulation data and DIMRI on the lower branch, and these all stem from the fact that we have been unable to find stable thermal equilibria in the simulations for effective temperatures higher than 3000 K. At such low temperatures, the opacities are so small that these equilibria are only marginally optically thick, with midplane optical depths $\tau \lesssim 5$. This may be a problem given that the simulations assume flux limited diffusion which may not accurately treat radiation transport at such low optical depths. The corresponding DIM models (i.e. DIM, DIMa, DIMRI) at these low temperatures also have low optical depths. As a consequence, the density at the photosphere (the exterior boundary condition) is a significant fraction of the central density implying that a large fraction of mass ($\sim 10-50\%$) is ignored/neglected[8]. This missing mass likely has a significant impact on the temperature and density profiles of DIM models and is, at least partly, responsible for the miss-match between the DIMRI curve and the simulation data on the lower branch of the S-curve. The influence that this missing mass has on the temperature profiles may also explain why the DIMRI models near the end of the lower branch are convective (which is why the DIMRI S-curve turns up at $\Sigma \approx 180$ g cm^{-2} in Figure 6.8), while there is no convection in any of the lower branch MRI simulations. Again, we have been unable

[8] These inaccuracies do not affect standard DIM models of real outbursts, because in these models the disk never cools down to temperatures at which these discrepancies appear. In the standard DIM one simply tunes $\alpha_{\rm h}$ and $\alpha_{\rm c}$ to obtain the required ratio of the critical surface densities.

to find any stable thermal equilibria at higher temperatures on the lower branch, where the opacities would be higher and missing mass would be less of an issue in the DIM models. However, there is perhaps an even bigger problem with the simulations on the lower branch, and that is that they neglect non-ideal MHD effects. As we demonstrate in Appendix 7.3, Ohmic resistivity and the Hall term are likely to be important here, and so this also casts uncertainty on the lower branch results, and specifically the critical point of the lower branch ($\Sigma^{-}_{\rm crit}$, $T^{-}_{\rm crit}$) which contributes to the determination of $Q\Sigma_{\rm crit}$. Future work will have to account for these effects on the lower branch. Our focus here, however, is to see whether the variation in α on the upper branch that has been found in the simulations can produce reasonable dwarf nova light curves.

Coming to the differences between our variants of the DIM, we first note that $\Sigma^{-}_{\rm crit}$ and $T^{-}_{\rm eff,crit}$ at the end of the lower branch are much higher on the classic DIM S-curve compared to both the DIMa and DIMRI S-curves, consequently DIM has the largest $Q\Sigma_{\rm crit}$. As DIMa shares exactly the same vertical structure assumptions and equations as the classic DIM, this can only be due to the different alpha-prescriptions between the two models (equations 6.5-6.6 and equation 6.1, respectively). Recall from Figure 6.1 that our fit to the simulation data has α starting to increase at $T_{\rm eff} \sim 4000$ K, roughly indicating the end of the lower branch. By contrast, the choice of $T^{+}_{\rm crit}$ in the classic DIM equation (6.1) corresponds to a much higher effective temperature (~ 6000 K) at the end of the lower branch.

It should be noted that we have no simulation data for 3000 K$\lesssim T_{\rm eff} \lesssim$7000 K in Figure

6.1, precisely because the simulations failed to produce stable thermal equilibria in this range. Therefore, our fit in equations 6.5-6.6 has some flexibility in this temperature range. In principle, we could have fit the simulation data in Figure 6.1 with a function that keeps α low until the effective temperature increases above 6000 K, and that would bring the lower branches of the DIMa and DIM S-curves into much better agreement. However, simulation ws0467 shown in Figure 6.4, was started near the end of the lower branch at $T_{\rm eff} \simeq 3000$ K and underwent runaway heating[9]. Hence our fits (equations 6.5-6.6) produce S-curves that better represent the behavior observed in the simulations.

Another alternative to achieve agreement on the lower branch is to reduce $T_{\rm c0}$ in the classic DIM. This has actually already been done by Hameury (2002), who modified this parameter to 8000 K, thereby producing a lower branch that only extended up to an effective temperature of 3000 K. This modification produces very similar outburst light curves, except that the quiescent light curves are flatter in shape, which actually may agree somewhat better with observations (Hameury, 2002). Whether the low $T^{-}_{\rm eff,crit}$ can be claimed as a success of the MRI simulations will require a full treatment of the non-ideal MHD effects that have so far been neglected, but are likely to be crucial in the quiescent state, and hence will likely shift the end of the lower branch.

As we discuss in more detail below, the new simulation-based vertical structure equations (most importantly the different $\alpha_{\rm ml}$) are the reason DIMRI has a different location for the end of the upper branch than DIM and DIMa in Figure 6.8. In fact, if we plot

[9] Although this helps constrain the end of the lower branch, it is numerically challenging to further resolve the critical point ($\Sigma^{-}_{\rm crit}$, $T^{-}_{\rm crit}$), as the simple act of relaxing from the initial conditions could push a simulation too far from ($\Sigma^{-}_{\rm crit}$, $T^{-}_{\rm crit}$) to obtain a thermal equilibrium.

a DIMRI S-curve with $\alpha_{\rm ml} = 1.5$, the end of the upper branch matches that of the DIM and DIMa S-curves. The very large effective mixing length parameter $\alpha_{\rm ml} = 6$ used in DIMRI results in more efficient convective transport, which flattens the temperature profile, increasing $T_{\rm eff}$ for a fixed midplane temperature $T_{\rm c}$. Because the opacity is largely determined by $T_{\rm c}$, it is $T_{\rm c}$ which determines where the end of the upper branch occurs. For radiative cooling the effective and central temperatures are related through

$$T_{\rm c} = \left(\frac{3\tau_{\rm tot}}{8}\right)^{1/4} T_{\rm eff}, \tag{6.32}$$

where $\tau_{\rm tot}$ is the total (vertical) disk opacity (see e.g. Dubus et al., 1999; Kotko et al., 2012). For a fully ionized disk the Rosseland opacity is $\kappa \sim \Sigma H^{-1} {T_{\rm c}}^{-7/2} {\rm cm}^2/{\rm g}$ from which follows the well known (Shakura & Sunyaev, 1973) relation $T_{\rm eff} \propto \Sigma^{5/14}$. Recombination breaks this relation and changes its slope while convection enhances cooling. The result is that the upper branch ends at higher effective temperature, and hence higher surface density.

6.4 Outburst Light Curves

6.4.1 The outburst cycle

During the low luminosity "quiescent" phase of a dwarf nova cycle, the effective temperature in the whole disk is lower than $T^{-}_{\rm eff,crit}$ (the disk is cold). The mass accretion rate is not constant across the cold disk so the disk accumulates matter, increasing its temperature and surface density (each disk annulus moves up the lower branch of its

local S-curve). Finally, at some radius, R_0, the accumulation time becomes shorter than the viscous time, and the ionization of gas becomes so significant that the local cooling mechanisms become inefficient and thermal equilibrium is lost. The annulus at R_0 undergoes rapid heating and makes the transition to the hot state (upper branch of its local S-curve). A narrow fully-ionized region of high viscosity has just formed at R_0, and is surrounded by cold matter. This induces a steep radial temperature gradient and the formation of the heating front, indicating the beginning of an outburst. Additionally, a spike in the Σ profile arises as a consequence of different viscous efficiencies in the hot and cold parts of the disk: the low viscosity outside the hot annulus provides insufficient outwards angular momentum transport to prevent further accumulation of mass at R_0. These steep Σ and $T_{\rm eff}$ gradients in the heating front cause matter and heat to diffuse to the adjacent annuli, forcing their transition to the hot state. The hot region in the disk widens as the heating front propagates through the disk causing the luminosity to rise. The elevated mass accretion rate in the hot region reduces the surface density behind the heating front and enhances the mass inflow to the inner disk region[10].

Once the heating front reaches the outer disk edge, the disk is fully ionized and reaches its maximum brightness (the outburst maximum). In the DIM, the minimum critical surface density $\Sigma^+_{\rm crit}$ at the end of the upper branch of the local S-curve is approximately proportional to radius R (Hameury et al., 1998), causing $\Sigma^+_{\rm crit}$ to be highest at $R_{\rm out}$. Consequently Σ manages to only rise slightly above this critical value near $R_{\rm out}$ as the

[10]We describe here an *inside-out* outburst. For high mass-transfer rates, outbursts can be of *outside-in* type, i.e. the heating front propagates inwards from the disk outer regions (see e.g. Lasota, 2001).

heating front passes and it falls below the critical value almost immediately after the front dissipates. At the radius where this happens the cooling is strongly enhanced by the change of opacities when $T_{\rm eff} < T^{+}_{\rm eff,crit}$ and Σ and $T_{\rm eff}$ gradients lead to the formation of the cooling front. The inward propagation of the cooling front through the disk leads to the observed outburst decay.

The cooling front develops at the outer disk edge almost at the same time as the heating front disappears, allowing no time for the mass accumulated in the outer parts of the disk to arrive at the inner disk radius before the cooling front sets in, even though the mass accretion rate everywhere in the hot disk has increased beyond the mass transfer rate from the secondary. The surface density profile at the outburst maximum is not yet proportional to $R^{-3/4}$ as expected in a hot stable disk. Therefore, even after the development of the cooling front, the mass accretion rate near the inner disk edge still increases until the mass excess from the outer disk region has traveled through the whole disk and has been accreted onto the white dwarf (see Figure 6.13 and for more details Kotko & Lasota 2012). Only after this will the hot region ahead of the cooling front reach the hot stable state where the constant mass accretion rate is of order $\dot{M}_{\rm tr}$, the mass transfer rate from the secondary.

6.4.2 Reflares

Due to the high $\dot{M}_{\rm tr}$ and low $\alpha_{\rm c}$, the disk may accumulate a lot of mass during the quiescent phase and rise to an outburst. If the viscosity in the hot disk is not efficient

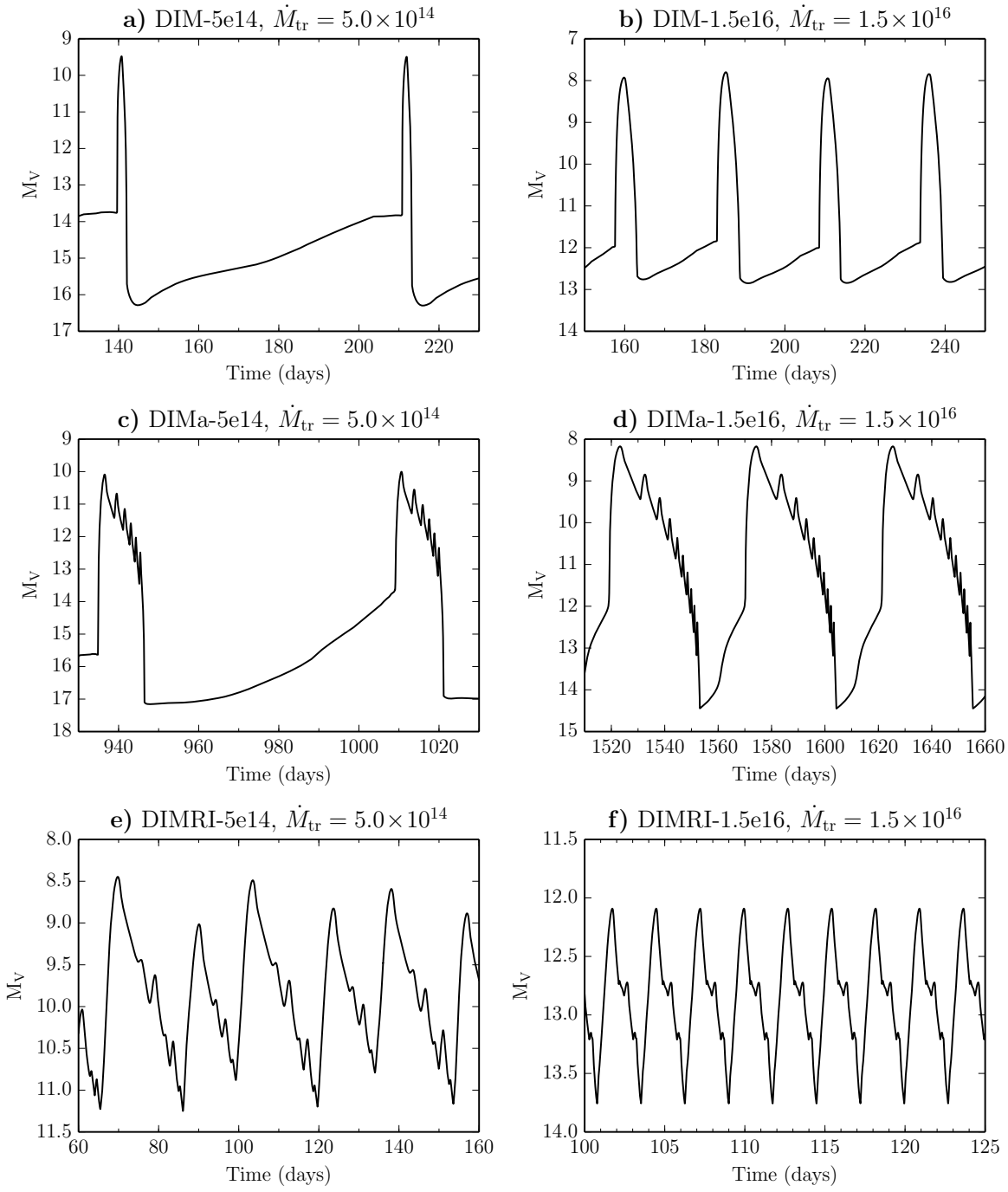

Figure 6.9 Visual magnitude lightcurves for six of the models listed in Table 6.1. The sawtooth-like features are reflares. The units for the listed mass transfer rates are g/s.

Table 6.1. Lightcurve Parameters

Model	$\dot{M}_{\rm tr}$ [g/s]	$A_{\rm outb}$	$T_{\rm outb}$	$T_{\rm quiesc}$	Figure
DIM-5e14	5×10^{14}	5.4	2.3	47.3	6.9a
DIM-1.5e16	1.5×10^{16}	4.6	6.3	11.6	6.9b
DIMa-5e14	5×10^{14}	7	11.6	46.4	6.9c
DIMa-1.5e16	1.5×10^{16}	6.3	50	0	6.9d
DIMRI-5e14	5×10^{14}	1.7	2.8	0	6.9e
DIMRI-1.5e16	1.5×10^{16}	2.6	19.9	0	6.9f
DIMRI-$\alpha_{ML} = 1.5$	5×10^{14}	7.7	17.3	60.1	6.10
DIMRI-6e13	6×10^{13}	3.2	1.9	7	6.11
DIMRItr-1.5e16	1.5×10^{16}	3.4	14.6	4.7	6.12

Note. — The parameters of the outbursts measured in our calculated lightcurves. $A_{\rm outb}$ is the outburst amplitude in magnitudes, $T_{\rm outb}$ is the outburst duration time in days and $T_{\rm quiesc}$ is the quiescence time in days, i.e. the time elapsed between the end of an outburst and the beginning of the next. The last column lists the figure where the lightcurve for a given model can be found.

enough (i.e. when $\alpha_{\rm h}$ is relatively low) to redistribute the mass excess accumulated during the previous outburst phases to the inner region (where it can be accreted), or if the critical points $(\Sigma^-_{\rm crit}, T^-_{\rm crit})$ and $(\Sigma^+_{\rm crit}, T^+_{\rm crit})$ are too close (i.e. $Q\Sigma_{\rm crit}$ is too small), the fronts propagating in the disk (both cooling and heating) may be stopped before arriving at either of the two disk edges. This gives rise to the appearance of reflares in the outburst lightcurves. As we discuss below, all our MRI-based models exhibit this phenomenon, and we therefore begin with a brief description of the cause: it is the confluence of the small $\alpha_{\rm h}$ high on the upper branch as well as the small $Q\Sigma_{\rm crit}$ that is responsible for these reflares.

As a cooling front propagates inward, the high viscosity of the hot matter inside the cooling front contrasted with the low viscosity outside the cooling front causes an outward diffusion of matter across the front. This in turn causes a deficit in surface density within the front itself, followed by an enhanced surface density in the cold region behind (outside) the front. Hence, as the cooling front moves inward in radius, at some point the post-front Σ may become high enough to cross the critical value $\Sigma^-_{\rm crit}$ at the end of the lower branch of the local S-curve. It is here where it is clearest that the low $\alpha_{\rm h}$ and the lack of sufficient separation between $\Sigma^-_{\rm crit}$ and $\Sigma^+_{\rm crit}$ (i.e. too small $Q\Sigma_{\rm crit}$) conspire against the smooth propagation of a cooling front by creating a mass excess outside the front and setting a low critical threshold respectively.

In this situation a new heating front arises and starts to move outwards. The matter heated by this newly formed front flows at a high rate into the zone of the cooling front,

increasing its temperature and surface density. This inflow of hot gas eventually destroys the cooling front and only a heating front is left. As a result, the inward propagating cooling front behaves as if it is reflected into an outward propagating heating front before it arrives at the inner edge. A similar mechanism can cause reflection of the heating front propagating toward the outer disk radius. If the post-front Σ remains close to $\Sigma^{+}_{\rm crit}$ the elevated accretion rate in the hot region behind the front may cause Σ to fall below the critical value and a cooling front will start to form. The reduced transport of the angular momentum through the emerging cold zone finally stops the propagation of the heating front and a newly formed cooling front will move inward. These reflections produce a reflare pattern in the outburst lightcurves (see sawtooth-like features in Figure 6.9), which are not observed in standard dwarf novae. As reviewed in section 4.3 of Lasota (2001), reflares are a common feature of the DIM, and one must work to get rid of them by choosing appropriate values of $\alpha_{\rm h}$ and $\alpha_{\rm c}$ in order to agree with the smooth observed light curves. As we will see shortly, reflares are also a generic feature of all our MRI-based lightcurves. However, it is important to reemphasize that the reflares (and the details of outbursts) are dependent on where the lower branch ends; a detail we do not claim to model accurately.

6.4.3 Results

The outburst properties depend on disk viscosity and the parameters characterizing a binary. For the new DIMRI to be considered as a possible replacement for the standard

DIM, it should reproduce the basic features of dwarf novae lightcurves such as outburst amplitude, outburst duration and quiescence duration.

To better understand how the new α-prescription and the new disk vertical structures introduced into the classical DIM influence outburst light curves, we calculated these light curves using three models: DIMRI, DIM with α as a function of $T_{\rm eff}$ (DIMa) and classic DIM with $\alpha_{\rm c} = 0.03$ and $\alpha_{\rm h} = 0.12$. All models were calculated for the same set of parameters: a primary mass $M_1 = 0.6\,{\rm M}_\odot$, the disk inner radius $R_{\rm in} = 8.67 \times 10^8$ cm, and the circularization radius $R_{\rm circ} = 2.85 \times 10^{10}$ cm. In addition we run the calculation for two different values of the mass transfer rate: $\dot{M}_{\rm tr} = 1.5 \times 10^{16}$ g/s and $\dot{M}_{\rm tr} = 5 \times 10^{14}$ g/s for each model (see Table 6.1). In all models the outer disk radius is variable due to the fact that we take into account the tidal force acting between the secondary star and the disk. For the models in this paper, the average outer disk radius is $\langle R_{\rm out} \rangle = 4.6 \times 10^{10}$ cm.

Analyzing the differences between the lightcurves (see Figures 6.9-6.12) gives insight into the physical implications of our modifications to the DIM. One subtle difference between the classic DIM lightcurves and the MRI based lightcurves is that the MRI based ones are not strictly periodic. We do not understand why the new α prescription causes this. One possibility is that the disk needs much more time to relax with this prescription. Conversely, the most striking difference between the DIM and the two other model light curves is that the outburst decay in DIM is smooth while in DIMRI and DIMa the outburst decay has small amplitude brightness variations characteristic of

reflares (compare Figure 6.9c-f with Figure 6.9a,b). The reason that reflares do not appear in the DIM but are present in the two other models is connected to our α-prescription, but is also tied to our uncertainties on the lower branch, specifically the location of the critical point ($\Sigma^{-}_{\rm crit}$, $T^{-}_{\rm crit}$). In the DIM, $Q\Sigma_{\rm crit}$ is larger than the other models and α maintains its high value ($\alpha_{\rm h} = 0.12 \gg \alpha_{\rm c}$) in the whole hot part of the disk until the cooling front passage. In the models where α is a function of effective temperature, the higher viscosity is present in a much more narrow region, i.e. in which the central temperature is higher than $T^{-}_{\rm crit}$ but lower than 5×10^4K. Therefore, the mass in the inner disk region is accreted at a lower rate than in the DIM due to the lowered viscosity in the high temperature regime, leading to an excess of mass behind (outside) cooling fronts. It is the combination this effect coupled with the small $Q\Sigma_{\rm crit}$ which is directly responsible for the reflares seen in DIMa and DIMRI. Furthermore, $Q\Sigma_{\rm crit}$ as determined by MRI simulations is actually larger than that found in DIMRI, which suggests that DIMRI is more susceptible to reflares than what the simulation data imply.

Figure 6.13 shows how the higher surface mass density in the inner disk and smaller $Q\Sigma_{\rm crit}$ in DIMa leads to reflections of the inward propagating cooling front and reflares. The first epoch shown (the red curves labeled 1) corresponds to the time when the outward propagating heating front has just arrived in the outer disk, which is why there is a spike in surface density and bump in midplane temperature at $R \sim 1.3 \times 10^{10}$ cm. By this time an inward propagating cooling front has already been launched, and is located at $\simeq 7.6 \times 10^9$ cm where the surface density has reached the critical surface density $\Sigma^{+}_{\rm crit}$

on the upper branch of the local S-curve. As the front propagates inward from 1 (red) to 2 (green) to 3 (blue), the gradients in viscosity cause outward mass diffusion, thereby producing a rarefaction in surface density down to $\Sigma^{+}_{\rm crit}$ within the cooling front, followed by an enhanced surface density behind (outside) the front. Because the inner disk in the outburst state has such a high surface density due to the *low* values of α high up on the upper branch relative to the DIM, the post-front excess in surface mass density is also high, and eventually, at epoch 4 (magenta) at $R = 4.6 \times 10^9$ cm, reaches the critical surface density $\Sigma^{-}_{\rm crit}$ at the end of the lower branch of the local S-curve (highlighting the role of small $Q\Sigma_{\rm crit}$). This triggers a heating front which then propagates outward, as evident in epoch 5 (black) at $R = 5.3 \times 10^9$ cm.

Hence, directly as a consequence of the small $\Sigma^{-}_{\rm crit}$ (or alternatively small $Q\Sigma_{\rm crit}$) combined with the low α's and resulting higher surface densities in the inner disk in outburst, the cooling front that would normally cause a transition back to quiescence propagates instead with difficulty, through a sequence of reflections seen as reflares in the light curve. In contrast, in the DIM with suitably chosen $\alpha_{\rm h}$ and $\alpha_{\rm c}$, there is a larger $\Sigma^{-}_{\rm crit}$ making it harder to trigger a reflare. Additionally, the mass diffusion and accretion during the outburst is much higher and the inner disk is able to process sufficient mass to lower the inner surface density and avoid the appearance of the reflares during the outburst decay. The contested propagation of the cooling front in DIMa causes the outburst decay phase to last longer compared to DIM (for example compare Figure 6.9a with Figure 6.9c). During this time more mass is being accreted onto the white dwarf in

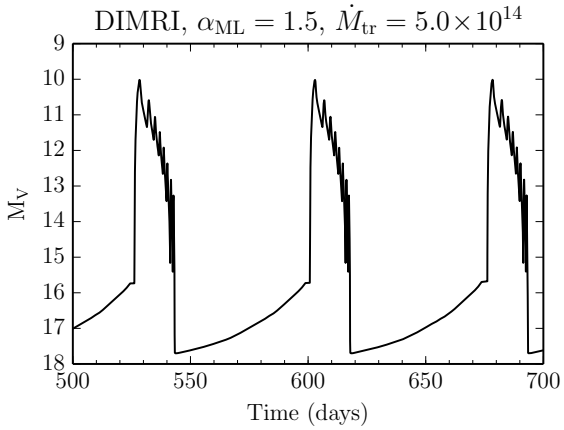

Figure 6.10 Light curves calculated from DIMRI but for $\alpha_{\rm ml} = 1.5$; $\dot{M}_{\rm tr} = 5.0\times10^{14}\,{\rm g\,s^{-1}}$. Compare with Fig. 6.9e.

the DIMa, leaving the disk less massive and less luminous than in the DIM at the end of outburst. This results in a higher amplitude outburst for the DIMa, which highlights the effect reflares have on outbursts.

The difference in light curves between DIMRI and DIMa is due to the different $\alpha_{\rm ml}$ values and different dissipation profiles. The mixing length parameter $\alpha_{\rm ml}$ is the most important difference, as can be seen by comparing Figure 6.9e with Figure 6.10, which presents the same DIMRI calculation but with $\alpha_{\rm ml}$ restored to its traditional value of 1.5. Convection sets in close to the point where the cold branch of the S-curve ends which leaves this point sensitive to $\alpha_{\rm ml}$. This effect is even stronger on the critical point where the hot branch starts, as this is where convection is the strongest. Higher values of $\alpha_{\rm ml}$ shift both critical points at which the S-curve bends closer together, leading to a smaller $Q\Sigma_{\rm crit}$. This alters the global behavior of the disk and the outburst properties: the decay from the outburst in a disk with $\alpha_{\rm ml} = 6$ starts at higher Σ and higher $T_{\rm eff}$, and less

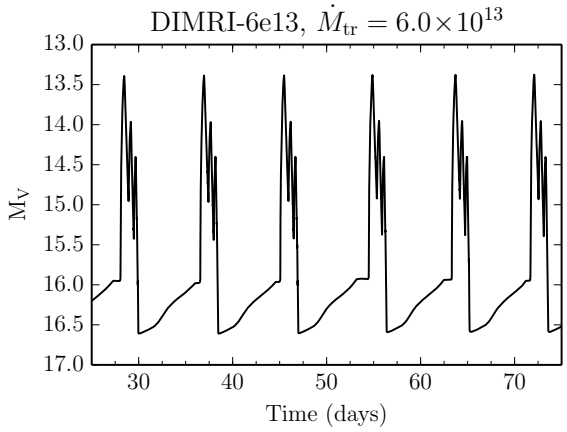

Figure 6.11 Light curves calculated from DIMRI with $\dot{M}_{\rm tr} = 6.0 \times 10^{13}\,{\rm g\,s^{-1}}$.

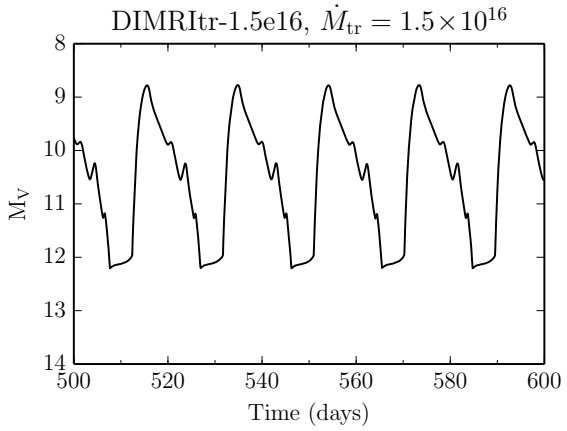

Figure 6.12 Light curves calculated from DIMRI with inner disk radius truncated by the magnetic field with magnetic moment $\mu = 8 \times 10^{30}$G cm^3 for $\alpha_{\rm ml} = 6.0$; $\dot{M}_{\rm tr} = 1.5 \times 10^{16}\,{\rm g\,s^{-1}}$. As can be seen by comparing this to Fig. 6.9f, the truncation of the inner disk results in the appearance of quiescence and more regular outbursts.

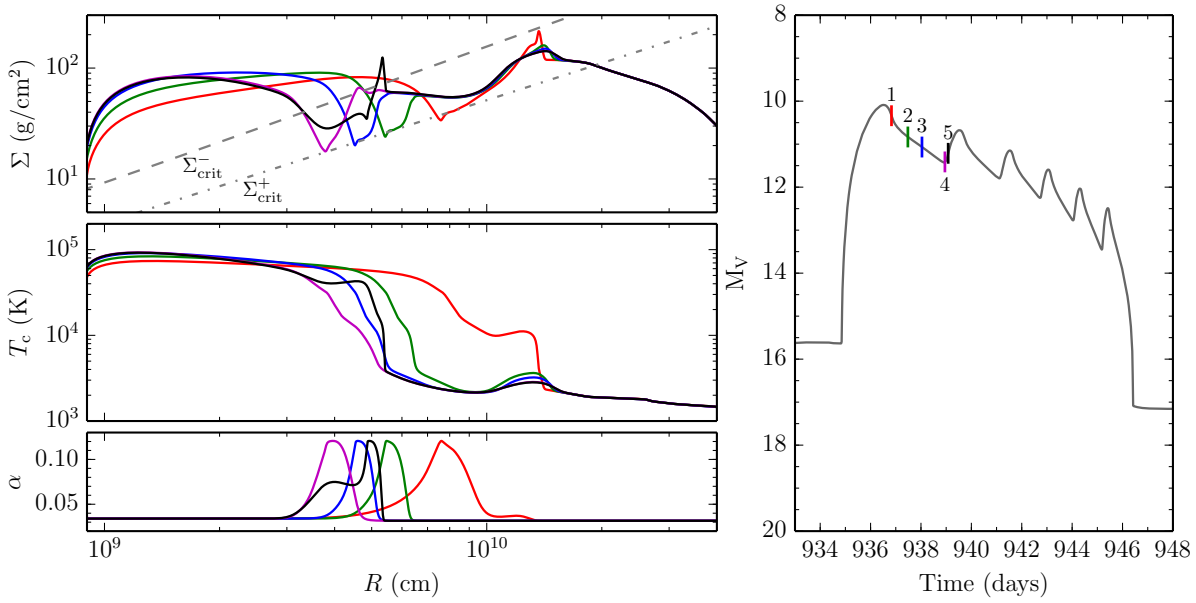

Figure 6.13 Left panels: Radial profiles of surface density (top), midplane temperature (middle), and α-parameter (bottom) during the initial decay from outburst for the DIMa calculation with $\dot{M} = 5 \times 10^{14}$ g s^{-1}. Right panel: Zoom of the first outburst in the lightcurve Figure 6.9(c). Different successive times 1-5 are shown by different colors as indicated, with 1 (red) being the first and 5 (black) being the last. It is important to note that α is small for $R < 3 \times 10^9$ cm for all epochs shown despite the fact that the disk is in outburst, because we are high on the upper branch here. This results in the elevated surface mass density that can be seen in the inner disk. As the cooling front (the dip/rarefaction in Σ located at $R \approx 7.6 \times 10^9$ cm in epoch 1) propagates inwards through the disk, mass is redistributed from ahead of the front where Σ is high to the post-front region. Eventually, the post-rarefaction surface density crosses the critical surface density $\Sigma^-_{\rm crit}$ at the end of the lower branch of the local S-curve. This occurs approximately at epoch 4 (magenta), which is when the inward propagating cooling front is reflected into the heating front seen at $R \approx 5.3 \times 10^9$ cm in epoch 5 (black). This figure clearly shows that either further separating $\Sigma^-_{\rm crit}$ and $\Sigma^+_{\rm crit}$ (i.e. increasing $Q\Sigma_{\rm crit}$) or reducing the excess mass in the inner disk by increasing α high on the upper branch could help alleviate reflares.

mass is accreted and accumulated in the disk during the outburst cycle. Therefore, more efficient convection produces outbursts that are more frequent and of lower amplitude, and even lack quiescent phases. While it is important to note that this lack of quiescence may be related to uncertainties in the end of the lower branch, there are other ways out. In the discussion below, we examine a few options to restore or modify quiescence.

The comparison of DIMRI with $\alpha_{\rm ml} = 1.5$ and DIMa (Figure 6.10 and Figure 6.9c) highlights the importance of changing the dissipation profile, as this is the only difference between these two models. The main difference is that the outbursts in DIMRI with $\alpha_{\rm ml} = 1.5$ are wider and the quiescence is longer than in the DIMa light curve.

Changing the mixing length parameter is not the only way to increase the outburst amplitude and restore quiescent phases to the DIMRI models. Increasing the mass transfer rate, while all other parameters are fixed, makes the disk hotter and denser. This means that the surface density everywhere in the quiescent disk is closer to the critical value and the disk luminosity is higher. The result is more frequent lower amplitude outbursts for higher mass transfer rate regardless of model, as illustrated by comparing the two mass transfer rates shown in Figure 6.9 for each of our three models. Hence merely reducing the mass transfer rate in the DIMRI model can increase the outburst amplitude and restore quiescent phases. If one sets $\dot{M}_{\rm tr}$ as low as $\dot{M}_{\rm tr} = 6 \times 10^{13}$ g/s in the DIMRI (with $\alpha_{\rm ml} = 6$) the elapsed time between two consecutive outbursts starts to be longer and also the outburst amplitude rises (see Table 6.1 and Figure 6.11). Note that for such a low $\dot{M}_{\rm tr}$, the disks in DIM and DIMa become cold and stable.

There is yet another alternative way to restore quiescence in the DIMRI light curves. Observed X-ray fluxes in quiescent dwarf novae are far too large compared to what models predict. A solution to this problem is a truncation of the inner disk. Numerical calculations by Hameury et al. (2000) and Schreiber et al. (2003) confirm that truncating the inner disk has substantial influence on the dwarf novae lightcurves and may solve the discrepancy between observations and theory. This truncation may be caused by the magnetic field of the primary white dwarf. A white dwarf magnetic field in the range $10^4 - 10^7$G (which translates to a magnetic moment $\mu \approx 1 - 10^3 \times 10^{30}$ G cm^3) is sufficient for the magnetic pressure close to the white dwarf to exceed the gas and ram pressures of the infalling matter during the quiescent phase of the dwarf nova cycle. The inner disk radius is therefore pushed away from the white dwarf to a radius R_M (e.g. Frank et al. 2002):

$$R_{\rm in} = R_{\rm M} = 9.8 \times 10^8 \dot{M}_{\rm tr15}^{-2/7} M_1^{-1/7} \mu_{30}^{4/7} {\rm cm} \tag{6.33}$$

where μ_{30} is the magnetic moment in units of 10^{30} G cm^3, M_1 is the mass of the primary in solar masses and $\dot{M}_{15}$ is the mass accretion rate in units of 10^{15} g/s. During outburst the situation changes, as the higher mass accretion rate sharply increases the ram pressure of matter which then dominates the magnetic pressure, and the inner edge of the disk approaches the surface of the white dwarf. Taking into account the variation in inner disk radius according to Eq.(6.33) restores the quiescent phase in the simulated DIMRI light curves (compare Figures 6.9f and 6.12).

6.5 Discussion

There are four main aspects of observed dwarf nova light curves which need to be reproduced in order to have a successful theoretical model: quiescence duration, outburst amplitude, outburst duration, and shape. For the most part our MRI based models DIMa (which differ from the DIM models only by incorporating the MRI simulation based $\alpha\left(T_{\rm eff}\right)$) and DIMRI can reproduce these attributes, with the notable exception of reflares. These reflares are the result of two contributing factors. Namely, the small ratio of the surface densities at the ends of the lower and upper branches, $Q\Sigma_{\rm crit}$, and the low value of α found high up on the upper branch. This low α causes an excess of surface mass density Σ in the inner disk. Consequently, as a cooling front propagates inward through the disk it accumulates substantial mass in the post-front region, and due to the small $Q\Sigma_{\rm crit}$, this post-front excess in Σ easily surpasses the critical value, $\Sigma_{\rm crit}^{-}$, and initiates a reflare. The reflares created by this series of events tend to prolong the decay from outburst. We have found two mechanisms which help to hasten this elongated decay from outburst: reducing the mass transfer rate and truncation of the inner disk by a white dwarf magnetic field (Figures 6.11-6.12). However, these tweaks are merely attempts to treat the symptoms caused by the greater underlying issues mentioned above[11].

It is important to remember that $Q\Sigma_{\rm crit}$ is determined by the physics of both the upper and lower branches, and the lower branch physics is very uncertain. The simulations were produced with the ideal MHD and flux limited diffusion approximations. While these

[11]Notice, however, that disk truncation is independently required by dwarf nova observations(see e.g., Lasota, 2001).

are reasonable on the upper branch, the lower branch is a different story. Optical depths along the lower branch are low ($\tau \lesssim 5$) bringing into question our usage of the flux limited diffusion approximation. Moreover, non-ideal effects, particularly resistivity and Hall effects (Bai, 2014; Lesur et al., 2014, Appendix 7.3) are important on the lower branch where the ionization fraction is low. This strongly motivates the need to pursue non-ideal MHD simulations of the lower branch, and as in protostellar disks (Igea & Glassgold, 1999), it may be necessary to account for irradiation by ionizing x-rays from the boundary layer between the white dwarf and the accretion disk, because any source of ionization has the potential to significantly modify non-ideal MHD effects. MRI turbulence may only exist in the irradiated surface layers, possibly leaving a magnetically driven laminar flow in the resistive "dead zone" interior (Turner & Sano, 2008). Small amounts of hydrodynamic angular momentum transport associated with thermal convection (Lesur & Ogilvie, 2010) may also exist. However, it may turn out that none of these local mechanisms is sufficient to explain the quiescent state, and that something involving more global physics is required. For example, recent isothermal and adiabatic global simulations by Ju et al. (2016) suggest that spiral waves excited by the tidal field of the donor star may contribute significantly to the angular momentum transport in the quiescent state, and this physics cannot be captured by a local stress-pressure relation. All this speculation, again highlights the uncertainty in $Q\Sigma_{\rm crit}$, and the need for the inclusion of non-ideal effects on the lower branch.

Even with this uncertainty, however, we have found that enhancement of α only near

the end of the upper branch, where thermal convection happens, is capable of producing outbursts. This outcome is non-trivial and suggests that convection plays a major role in the outbursts of dwarf novae, and while important, convection may not be the end of the story. The low values of α high up on the upper branch as found by Hirose et al. (2014), are a contributing factor in the appearance of reflares. As mentioned early on in this paper, MRI simulations with net vertical magnetic flux have larger α values (Hawley et al., 1995; Sano et al., 2004; Pessah et al., 2007). While we have considered a way of increasing α with zero net vertical magnetic flux by the effects of hydrodynamic convection on MRI turbulence, there is no reason to view these explanations as mutually exclusive. Accordingly, simulations examining how net vertical magnetic flux modifies convection and the associated enhancement of α found in Hirose et al. (2014) would be useful and may help alleviate reflares.

It is also important to note that we have not successfully incorporated all aspects of the physics observed in the simulations in our attempts to model outburst light curves here. The MRI-based physics that we have succeeded in incorporating into the DIM has not produced S-curves that completely agree with the simulation data (cf. Figure 6.8). Both the upper and lower branches of the MRI simulation S-curve are extended slightly further in Σ compared to DIMRI. This implies that DIMRI should have a larger $Q\Sigma_{\rm crit}$ which in turn would increase the amplitude and the quiescence duration and may reduce or even alleviate the reflares.

Moreover, it is clear that the MRI simulations exhibit some time dependent behavior

(e.g. intermittent convection) that the DIM simply is incapable of handling. During the convective epochs the Shakura & Sunyaev (1973) α parameter is enhanced and also $\alpha_{\rm ml} \sim 1.5$. To re-emphasize this, α is significantly higher and $\alpha_{\rm ml}$ significantly lower during the intermittent convective epochs than their respective time averaged quantities. This has a significant impact on the evolution of an annulus as it transitions from quiescence to outburst[12]. Thermally unstable MRI simulations that are heating towards the hot branch are fully convective, with no intermittency. Therefore, when an annulus first makes it to the hot branch it will be fully convective and "see" an instantaneous S-curve which is characterized by the α and $\alpha_{\rm ml}$ seen during convective epochs. This annulus will then evolve and after a few thermal times become better characterized by the time averaged values for α and $\alpha_{\rm ml}$ and the associated "long-term" S-curve. Global MRI simulations of the propagation of heating and cooling fronts would obviously be of great interest, but are not yet viable for the dwarf nova problem.

We finally note that the quiescent state is also a problem for the DIM models (i.e. DIM, DIMa, DIMRI) presented here and historically in the standard DIM; see e.g. Lasota (2001). Our lower branch DIM models with $T_{\rm eff} < 3000$ K have low optical depths[13] ($\tau \lesssim 5$) which leads to inaccuracies, most notably $\sim 10 - 50\%$ of mass lying outside of the vertical boundary condition. However, until non-ideal effects are included in the lower branch simulations, it is futile to try and bring the simulation data and DIM models into

[12] We note that our shearing box simulations are local not only in the radial direction, but also in the azimuthal direction. Therefore, the time dependent behavior may be less manifest in observations where azimuthal variations are averaged.

[13] This does not occur in the classical DIM, because without the MRI-based constraints we have imposed in this paper $\alpha_{\rm c}$ and $\alpha_{\rm h}$ can be tuned to avoid this problem.

better agreement here. This impacts the details of outburst lightcurves, most notably the occurrence of reflares. While these reflares are not observed in the outbursts of standard dwarf novae, we nevertheless recover outburst time scales and amplitudes comparable to those observed, implying that the simulation-based models of the upper branch are in good agreement with observations.

6.6 Chapter Summary

We have incorporated the convection-induced enhancement of α close to the hydrogen ionization temperature that was discovered in MRI simulations by Hirose et al. (2014) into the DIM. This, for the first time, places the early inference by Mineshige & Osaki (1983); Smak (1984); Meyer & Meyer-Hofmeister (1984) that α had to be larger in outburst in dwarf novae on a strong and clear theoretical foundation based on MRI turbulence. We have also shown how to incorporate aspects of the time-averaged vertical structure (dissipation profiles, intermittent convective heat transport) into the DIM. With suitable parameter choices and/or truncation of the inner disk by a white dwarf magnetic field, the resulting lightcurves are able to produce outburst and quiescent durations, as well as outburst amplitudes, that are consistent with observations of dwarf novae. Further work to actually fit particular dwarf nova systems with this model might be worthwhile.

A generic feature of our MRI-based α-prescription is the appearance of reflares. These reflares are caused by the confluence of low α's high up on the upper branch and the small ratio of critical surface mass densities $Q\Sigma_{\rm crit}$. Our biggest uncertainty in this work

is the physics of the lower branch and consequently $Q\Sigma_{\rm crit}$. This uncertainty primarily stems from the exclusion of important non-ideal MHD effects associated with the largely electrically neutral plasma on the lower branch. This gives us a clear motivation and direction for future work to address these inaccuracies in new simulations and to obtain a more realistic understanding of the lower branch and its end.

Additionally, while we have tried to incorporate MRI-based physics into the DIM, this has only been done for annuli in thermal equilibrium. We still do not understand how MRI physics might affect the propagation of heating and cooling fronts, and it is these that are responsible for reflares. MRI simulations in a more global geometry that can track the propagation of such fronts would of course be very illuminating, though such simulations appear to be challenging with current resources.

Finally, it is important to remember that reflares are also a common problem even in the standard DIM, where one is free to choose values of $\alpha_{\rm h}$ and $\alpha_{\rm c}$ to try and get rid of them (e.g. Lasota 2001). This freedom is of course an illusion, as the stresses are actually determined by the underlying physics of turbulence in the disk. The fact that applications of our MRI simulation results to the DIM give rise to reflares helps sharpen this problem by relating it more to the fundamental physics responsible for stresses in the disk.

Chapter 7

Future Directions

While the discovery of the convective enhancement of α helps bring the DIM and MRI simulations into agreement, it may not be enough to explain DNe outbursts (see Chapter 6). It is plausible that the MRI and other local mechanisms are not able to explain the quiescent state, requiring more global physics. Recently, Ju et al. (2016) produced adiabatic and isothermal global simulations which suggest that tidally excited spiral waves can significantly contribute to the angular momentum transport during DN quiescence. Additionally, observational evidence for two-armed spiral structures has been identified (Baptista et al., 2005). These types of features cannot be captured by a local stress-pressure relation, like the α prescription, and thus require global disk simulations.

7.1 Helium Disks and AM Canum Venaticorum

AM Canum Venaticorum type stars (AM CVns) are very similar to DNe, but they are much tighter binary systems with orbital periods $\lesssim 65$ min. Similar to DNe the primary is a white dwarf, but in Am CVns the secondary is a helium rich, hydrogen poor star such as a helium white dwarf (Nelemans, 2005). This makes the accretion disks of Am CVns free of hydrogen. Despite these differences, Am CVns display several outburst features which have analogs in DNe (Kotko et al., 2012)[1]. The existence of these systems allows us to probe the importance of chemical composition in accretion disks by comparing and contrasting AM CVns with DNe.

The easiest way to compare DNe and AM CVns is to run shearing box simulations of the latter and compare the results to those discussed in this work. In fact we are currently doing so, and the preliminary data shows a similar convective enhancement of α and convective quenching of magnetic field reversals. While there are some notable differences between the AM CVn and DN simulations we refrain from discussing further results until more data has been computed[2].

In addition to testing effects of chemical composition, AM CVns are interesting in their own right. For instance when space-based gravitational wave detectors (such as the proposed eLISA mission) become operational, AM CVns will be the predominant low-frequency noise for these detectors. A few of these systems will produce discrete signals

[1] Although, a significant fraction of their outbursts do not resemble those considered in standard DN.

[2] Currently being done using the Extreme Science and Engineering Discovery Environment (XSEDE), which is supported by National Science Foundation grant number ACI-1548562 (Towns et al., 2014).

which extend above this noise (Postnov & Yungelson, 2014). It is therefore likely that AM CVns will become increasingly more scrutinized (both observationally and theoretically) over the coming years. The work proposed here will add to this knowledge and help the community further understand these systems.

Furthermore, AM CVns are the perfect candidate for the first global simulations of accretion disks including proper thermodynamics. This is due to the small dynamic range in these disk systems. The compactness of these systems also enhances tidally induced spiral waves, and probing the interaction of MRI physics with these waves will be feasible in global simulations.

7.2 Global Simulations

There are numerous persistent mysteries in accretion disk physics, many of which are linked to global phenomena such as spiral waves and outbursts. Several of these can be analyzed within the context of white dwarf accretion disks. To gain traction in this field, 3D global radiation-MHD simulations will be run using the `Athena++` code. `Athena++` is the optimal choice for these simulations due to its static mesh refinement, which provides high resolution only where it is needed, as well as having a variety of grid geometries including spherical-polar coordinates. It is also worth noting that `Athena++` is part of a long lineage within computational astrophysics, as it is the successor of `Athena` (Stone et al., 2008) which is itself the successor of `Zeus` (Stone & Norman, 1992a,b; Turner & Stone, 2001). However to properly utilize `Athena++` some additional physics must be

included.

For simulations of accreting white dwarfs there are three important additional pieces of physics: non-ideal equation of state (EOS), non-ideal MHD effects, and radiation transport. While each of these three pieces have individually been used in accretion disk simulations (e.g. Hirose et al., 2014; Lesur et al., 2014; Jiang et al., 2016) there has yet to be a simulation which utilizes all three. Additionally there have been significant advancements in radiation transport (Jiang et al., 2014) since the introduction of FLD, which was the radiative transfer method used in our `Zeus` simulations (see Section 3.2). The hydrogen and helium ionization instabilities are the reason all of this physics is needed and are also the cause of DN and AM CVn outbursts. The outbursts are ultimately what makes these systems so interesting in the first place.

To make these simulations a reality we are developing a non-ideal EOS module for `Athena++`. This physics is necessary in understanding ionization instabilities and will enable our global simulations to probe what makes the light curves of AM CVns more complicated than those of DNe. Features which are considered peculiar in DNe, such as superoutbursts and their associated superhumps, are typical in AM CVns (Kotko et al., 2012). By simulating these systems with tidal fields we may be able to provide important insight into the possible existence of tidal-thermal instabilities (Osaki, 1996) in AM CVns, which has fallen out of favor for DNe (Smak, 2009a,b).

7.3 Non-ideal MHD

In quiescence, DN accretion disks are colder than the hydrogen ionization threshold, making them mostly neutral. Even though our `Zeus` simulations assume ideal MHD they can be utilized to estimate the importance of non-ideal MHD effects. Here we examine non-ideal MHD effects due to thermal ionization only (i.e. neglecting irradiation) and their possible importance in DN quiescence. By non-ideal MHD effects, we are referring to Ohmic dissipation (i.e. resistivity), the Hall term, and ambipolar diffusion. The full induction equation including these terms can be written as (Lesur et al., 2014)[3]

$$\frac{\partial \mathbf{B}}{\partial t} - \nabla \times (\mathbf{v} \times \mathbf{B}) = -\frac{\nabla}{\mu_0} \times \left[\eta_{\mathrm{O}} \mathbf{J} + \eta_{\mathrm{H}} \mathbf{J} \times \mathbf{e_b} - \eta_{\mathrm{A}} (\mathbf{J} \times \mathbf{e_b}) \times \mathbf{e_b}\right], \tag{7.1}$$

where $\mathbf{J} = \mu_0 \nabla \times \mathbf{B}$ and $\mathbf{e_b} = \mathbf{B}/|\mathbf{B}|$. The terms on the right hand side are respectively the Ohmic resistive term (O), the Hall term (H), and the ambipolar diffusion term (A), where the η coefficients are the respective diffusivity coefficients. The Hall term is caused by a velocity difference between electrons (e) and heavy cations (i), while Ohmic dissipation and ambipolar diffusion are caused by collisions between neutrals (n) and electrons or cations respectively. It is worthwhile briefly discussing the relevant quantities involving these collisions. The momentum rate coefficients for ion-neutral and electron-neutral collisions are $< \sigma v >_{\mathrm{ni}} = 1.9 \times 10^{-9}$ cm^3 s^{-1} (Draine, 2011) and $< \sigma v >_{\mathrm{ne}} = 8.3 \times 10^{-10} T^{1/2}$ cm^3 s^{-1} (Draine et al., 1983a), respectively. The ion-neutral

[3] Here we explicitly use μ_0, causing our presentation to differer by factors of μ_0 compared to that of Lesur et al. (2014).

drag coefficient is therefore

$$\gamma = \frac{<\sigma v>_{\rm ni}}{m_{\rm n}+m_{\rm i}} = 2.7\times10^{13}\left(\frac{m_{\rm n}+m_{\rm i}}{41.37\,m_{\rm u}}\right)^{-1}{\rm cm^3\,s^{-1}\,g^{-1}}, \tag{7.2}$$

where we have taken $m_{\rm n} = 2.37\,m_{\rm u}$ (the mean molecular weight for our abundances, taking all the hydrogen to be molecular), and $m_i = 39\,m_{\rm u}$ (K^+, appropriate for thermal ionization; Balbus & Terquem, 2001)[4]. The diffusivity coefficients for Ohmic, Hall, and ambipolar diffusion are as follows (in the absence of dust; Balbus & Terquem, 2001; Wardle, 2007; Lesur et al., 2014):

$$\eta_{\rm O} = \frac{c^2 m_{\rm e}}{\mu_0 e^2}\frac{n_{\rm n}}{n_{\rm e}}\left\langle\sigma v\right\rangle_{\rm ne} \tag{7.3}$$

$$\eta_{\rm H} = \frac{Bc}{\sqrt{4\pi\mu_0}en_{\rm e}} = \sqrt{\frac{\rho}{4\pi}}\frac{v_{\rm A}c}{n_{\rm e}e} \tag{7.4}$$

$$\eta_{\rm A} = \frac{B^2}{\mu_0\gamma_{\rm i}\rho\rho_{\rm i}} = \frac{v_{\rm A}^2}{\gamma_{\rm i}\rho_{\rm i}}, \tag{7.5}$$

where $v_{\rm A} = B/\sqrt{\mu_0\rho}$ is the Alfvén speed.

[4] Note that Blaes & Balbus (1994a) adopted $m_{\rm i} = 30m_{\rm u}$, appropriate for the interstellar medium; while Sano et al. (2000) adopted $m_i = 24\,m_{\rm u}$ (Mg^+) appropriate for ionization in accretion disks due to irradiation.

By introducing the isothermal sound speed $c_{\rm s} = \sqrt{kT/\mu m_{\rm u}}$ we can examine the ratios

$$\frac{\eta_{\rm H}}{\eta_{\rm O}} = \sqrt{4\pi}\frac{v_{\rm A}}{c_{\rm s}}\sqrt{\frac{n_{\rm tot}}{n_{\rm n}}}\frac{\sqrt{kT}}{\langle\sigma v\rangle_{\rm ne}}\frac{e}{cm_{\rm e}}n_{\rm n}^{-1/2} \tag{7.6}$$

$$= 1.14\frac{v_{\rm A}}{c_{\rm s}}\sqrt{\frac{n_{\rm tot}}{n_{\rm n}}}\left(\frac{m_{\rm u}n_{\rm n}}{10^{-6}\ {\rm g\ cm^{-3}}}\right)^{-1/2}$$

$$\frac{\eta_{\rm A}}{\eta_{\rm H}} = \sqrt{4\pi}\frac{n_{\rm e}}{n_{\rm i}}\frac{v_{\rm A}}{c_{\rm s}}\frac{e}{\gamma_{\rm i}cm_{\rm i}\sqrt{\rho}}\sqrt{\frac{kT}{\mu m_{\rm u}}} \tag{7.7}$$

$$= 6.61\times10^{-3}\frac{n_{\rm e}}{n_{\rm i}}\frac{v_{\rm A}}{c_{\rm s}}f_{\rm M}\left(\rho_{-6}\right)^{-1/2}\left(\frac{T}{3000\ {\rm K}}\right)^{1/2}$$

$$f_{\rm M} \equiv \left(\frac{m_{\rm i}}{39m_{\rm u}}\right)^{-1}\left(\frac{m_{\rm n}+m_{\rm i}}{41.37\,m_{\rm u}}\right)\left(\frac{\mu}{2.37}\right)^{-1/2}, \tag{7.8}$$

where $\rho_{-6} = \rho/10^{-6}$ g cm^{-3}, and $f_{\rm M} = 1$ for the abundances and masses we assume here. From this we immediately conclude that the Hall term will likely be important whenever the Ohmic dissipation is important, as we are typically talking about densities and temperatures in this range. However, ambipolar diffusion is negligible compared to both of the other two non-ideal effects.

To determine how important the Ohmic and Hall terms are, it is useful to examine the following dimensionless Elsasser numbers which can be computed from simulation profiles:

$$\mathrm{Re_m} \equiv \frac{v_{\rm A}^2}{\Omega\eta_{\rm O}} \tag{7.9}$$

$$\mathrm{Ha} \equiv \frac{v_{\rm A}^2}{\Omega\eta_{\rm H}} \tag{7.10}$$

For the hottest lower branch simulation (ws0438) we have computed the horizontally

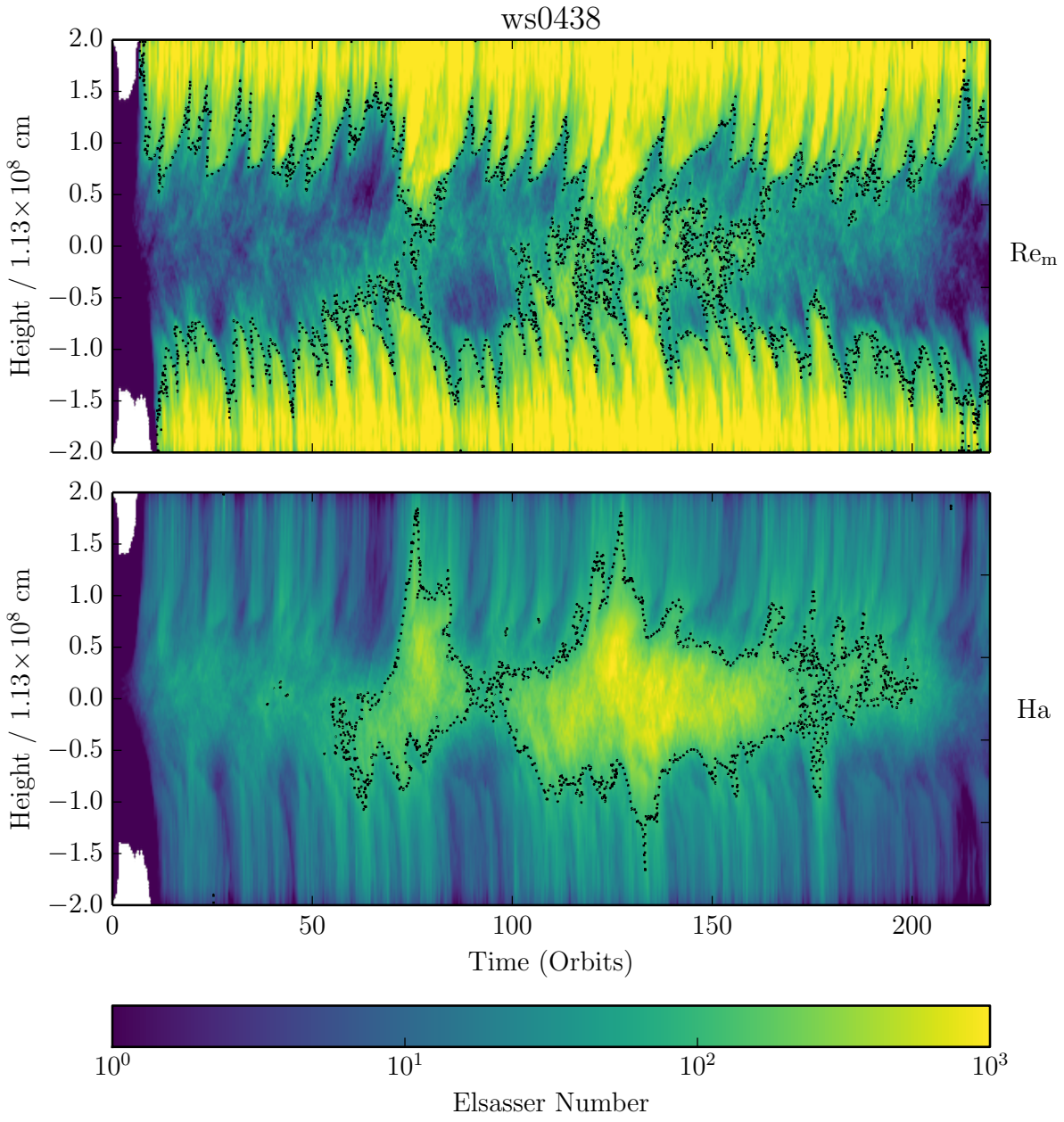

Figure 7.1 Horizontally averaged Elsasser numbers for the hottest lower branch simulation (ws0438). Lower Elsasser number corresponds to non-ideal MHD effects being more important. $\mathrm{Re_m}$ (Eq. 7.9, top panel) corresponds to Ohmic dissipation and Ha (Eq. 7.10, bottom panel) corresponds to the Hall term. Previous works (e.g. Hawley et al., 1996; Lesur & Longaretti, 2007) suggest that Ohmic dissipation is important for $\mathrm{Re_m} \lesssim 100$; we have therefore plotted a dotted black contour at $\mathrm{Re_m}$, Ha $= 100$. This indicates that non-ideal MHD effects are likely important for the majority of this simulation.

averaged Elsasser numbers (see Figure 7.1). Previous works (e.g. Hawley et al., 1996; Lesur & Longaretti, 2007) show that Ohmic dissipation is important when $\mathrm{Re_m}$ is less than a few hundred and much of ws0438 has Elsasser numbers below 100 (the dotted black contour of Figure 7.1). The other lower branch simulations are colder than ws0438 and are therefore more susceptible to non-ideal effects, implying that non-ideal MHD effects are important in dwarf nova quiescence. Future work should therefore include Ohmic dissipation and the Hall term in our simulations, but the ambipolar diffusion term is probably not necessary.

Chapter 8

Conclusions

Hydrodynamic convection is a natural consequence of the atomic physics associated with ionization instabilities in accretion disks. The transition from neutral to ionized hydrogen sets the fundamental temperatures in the S-curve of DNe. This transition also causes convection through a rise in opacity and decline in Γ_1. This only happens near the ionization temperature, explaining why our simulations only find convection at the low temperature end of the outburst phase. As demonstrated in Chapter 4 this hydrodynamic convection enhances α by seeding the MRI with vertical magnetic fields, bringing α closer to values inferred from observations.

We also found that this convection has profound effects on the magnetic dynamo found in accretion disk simulations (see Chapter 5). The typical reversals of azimuthal magnetic field occurring every ~ 10 orbits (i.e. the butterfly diagram) is completely disrupted by the presence of hydrodynamic convection. By examining the relation between B_y and

specific entropy, we were able to confirm that convection suppresses field reversals by mixing highly magnetized fluid parcels from high altitude down into the midplane. The polarity of this mixed magnetic field opposes that created by any field reversals in the midplane, annihilating them before they can propagate outwards.

In Chapter 6 we took the results of our simulations and used them to enhance the DIM. This included taking into account the variation of α with temperature and the relation between pressure and dissipation as measured from our simulations. With these enhancements we were able to produce lightcurves with roughly the right outburst amplitude, duration and recurrence time, with a few caveats (see Section 6.5). This suggests that we have finally brought simulation based α values into agreement with those inferred from DN observations, finally explaining the enhancement of α in outburst.

Bibliography

Abbott, B. P., et al. 2016a, Phys. Rev. Lett., 116, 241103

—. 2016b, Phys. Rev. Lett., 116, 061102

—. 2017, Phys. Rev. Lett., 118, 221101

Anders, E., & Grevesse, N. 1989, Geochim. Cosmochim. Acta, 53, 197

Bahcall, J. N., Dar, A., & Piran, T. 1987, Nature, 326, 135

Bai, X.-N. 2014, ApJ, 791, 137

Bai, X.-N., & Stone, J. M. 2013, ApJ, 767, 30

Balbus, S. A., & Hawley, J. F. 1991, ApJ, 376, 214

—. 1998, Reviews of Modern Physics, 70, 1

Balbus, S. A., & Terquem, C. 2001, ApJ, 552, 235

Baptista, R., Morales-Rueda, L., Harlaftis, E. T., Marsh, T. R., & Steeghs, D. 2005, A&A, 444, 201

Beckwith, K., Armitage, P. J., & Simon, J. B. 2011, MNRAS, 416, 361

Bellerive, A. 2004, International Journal of Modern Physics A, 19, 1167

Blackman, E. G., & Tan, J. C. 2004, Ap&SS, 292, 395

Blaes, O., Hirose, S., & Krolik, J. H. 2007, ApJ, 664, 1057

Blaes, O., Krolik, J. H., Hirose, S., & Shabaltas, N. 2011, ApJ, 733, 110

Blaes, O. M., & Balbus, S. A. 1994a, ApJ, 421, 163

—. 1994b, ApJ, 421, 163

Bodo, G., Cattaneo, F., Mignone, A., & Rossi, P. 2012, ApJ, 761, 116

—. 2013, ApJ, 771, L23

—. 2015, ApJ, 799, 20

Brandenburg, A., Nordlund, A., Stein, R. F., & Torkelsson, U. 1995, ApJ, 446, 741

Brandenburg, A., & Schmitt, D. 1998, A&A, 338, L55

Cannizzo, J. K., & Mattei, J. A. 1992, ApJ, 401, 642

Chandrasekhar, S. 1960, Proceedings of the National Academy of Science, 46, 253

Coleman, M. S. B., Kotko, I., Blaes, O., Lasota, J.-P., & Hirose, S. 2016, MNRAS, 462, 3710

Coleman, M. S. B., Yerger, E., Blaes, O., Salvesen, G., & Hirose, S. 2017, MNRAS, 467, 2625

Davis, S. W., Stone, J. M., & Pessah, M. E. 2010, ApJ, 713, 52

Draine, B. T. 2011, Physics of the Interstellar and Intergalactic Medium (Princeton University Press)

Draine, B. T., Roberge, W. G., & Dalgarno, A. 1983a, ApJ, 264, 485

—. 1983b, ApJ, 264, 485

Dubus, G., Hameury, J.-M., & Lasota, J.-P. 2001, A&A, 373, 251

Dubus, G., Lasota, J.-P., Hameury, J.-M., & Charles, P. 1999, MNRAS, 303, 139

Ferguson, J. W., Alexander, D. R., Allard, F., Barman, T., Bodnarik, J. G., Hauschildt, P. H., Heffner-Wong, A., & Tamanai, A. 2005, ApJ, 623, 585

Flaherty, K. M., Hughes, A. M., Rosenfeld, K. A., Andrews, S. M., Chiang, E., Simon, J. B., Kerzner, S., & Wilner, D. J. 2015, ApJ, 813, 99

Flock, M., Dzyurkevich, N., Klahr, H., Turner, N., & Henning, T. 2012, ApJ, 744, 144

Frank, J., King, A., & Raine, D. J. 2002, Accretion Power in Astrophysics: Third Edition (Cambridge University Press)

Fromang, S., Latter, H., Lesur, G., & Ogilvie, G. I. 2013, A&A, 552, A71

Fromang, S., Papaloizou, J., Lesur, G., & Heinemann, T. 2007, A&A, 476, 1123

Galeev, A. A., Rosner, R., & Vaiana, G. S. 1979, ApJ, 229, 318

Gammie, C. F., & Menou, K. 1998, ApJ, 492, L75

Gressel, O. 2010, MNRAS, 405, 41

—. 2013, ApJ, 770, 100

Gressel, O., & Pessah, M. E. 2015, ApJ, 810, 59

Guan, X., & Gammie, C. F. 2011, ApJ, 728, 130

Hameury, J., Lasota, J., & Warner, B. 2000, A&A, 353, 244

Hameury, J.-M. 2002, in Astronomical Society of the Pacific Conference Series, Vol. 261, The Physics of Cataclysmic Variables and Related Objects, ed. B. T. Gänsicke, K. Beuermann, & K. Reinsch, 377

Hameury, J.-M., Lasota, J.-P., Knigge, C., & Körding, E. G. 2017, A&A, 600, A95

Hameury, J.-M., Menou, K., Dubus, G., Lasota, J.-P., & Hure, J.-M. 1998, MNRAS, 298, 1048

Harrison, T. E., McNamara, B. J., Szkody, P., McArthur, B. E., Benedict, G. F., Klemola, A. R., & Gilliland, R. L. 1999, ApJ, 515, L93

Hawley, J. F., & Balbus, S. A. 1991, ApJ, 376, 223

Hawley, J. F., Gammie, C. F., & Balbus, S. A. 1995, ApJ, 440, 742

—. 1996, ApJ, 464, 690

Hawley, J. F., Guan, X., & Krolik, J. H. 2011, ApJ, 738, 84

Hazen, M. 1997, Journal of the American Association of Variable Star Observers (JAAVSO), 26, 59

Hirose, S. 2015, MNRAS, 448, 3105

Hirose, S., Blaes, O., Krolik, J. H., Coleman, M. S. B., & Sano, T. 2014, ApJ, 787, 1

Hirose, S., Krolik, J. H., & Blaes, O. 2009, ApJ, 691, 16

Hirose, S., Krolik, J. H., & Stone, J. M. 2006, ApJ, 640, 901

Igea, J., & Glassgold, A. E. 1999, ApJ, 518, 848

Jiang, Y.-F., Davis, S. W., & Stone, J. M. 2016, ApJ, 827, 10

Jiang, Y.-F., Stone, J. M., & Davis, S. W. 2013, ApJ, 778, 65

—. 2014, ApJ, 784, 169

Ju, W., Stone, J. M., & Zhu, Z. 2016, ApJ, 823, 81

Kafka, S. 2016, Observations from the AAVSO International Database, `https://www.aavso.org`, accessed: 2017-05-11

King, A. R., & Kolb, U. 1995, ApJ, 439, 330

King, A. R., Pringle, J. E., & Livio, M. 2007, MNRAS, 376, 1740

King, A. R., & Ritter, H. 1998, MNRAS, 293, L42

Kotko, I., & Lasota, J.-P. 2012, A&A, 545, A115

Kotko, I., Lasota, J.-P., Dubus, G., & Hameury, J.-M. 2012, A&A, 544, A13

Krolik, J. H., Hirose, S., & Blaes, O. 2007, ApJ, 664, 1045

Kunz, M. W., & Lesur, G. 2013, MNRAS, 434, 2295

Lasota, J.-P. 2001, NewAR, 45, 449

Lasota, J.-P., Dubus, G., & Kruk, K. 2008, A&A, 486, 523

Latter, H. N., & Papaloizou, J. C. B. 2012, MNRAS, 426, 1107

Lesur, G., Ferreira, J., & Ogilvie, G. I. 2013, A&A, 550, A61

Lesur, G., Kunz, M. W., & Fromang, S. 2014, A&A, 566, A56

Lesur, G., & Longaretti, P.-Y. 2007, MNRAS, 378, 1471

Lesur, G., & Ogilvie, G. I. 2010, MNRAS, 404, L64

Malygin, M., Kuiper, R., Klahr, H., Henning, T., & Dullemond, C. P. 2013, in Protostars and Planets VI Posters

Menou, K. 2000, Science, 288, 2022

Meyer, F., & Meyer-Hofmeister, E. 1984, A&A, 132, 143

Miller, K. A., & Stone, J. M. 2000, ApJ, 534, 398

Miller-Jones, J. C. A., Sivakoff, G. R., Knigge, C., Körding, E. G., Templeton, M., & Waagen, E. O. 2013, Science, 340, 950

Mineshige, S., & Osaki, Y. 1983, PASJ, 35, 377

Mineshige, S., & Wheeler, J. C. 1989, ApJ, 343, 241

Nelan, E. P., & Bond, H. E. 2013, ApJ, 773, L26

Nelemans, G. 2005, in Astronomical Society of the Pacific Conference Series, Vol. 330, The Astrophysics of Cataclysmic Variables and Related Objects, ed. J.-M. Hameury & J.-P. Lasota, 27

Okuzumi, S., & Hirose, S. 2011, ApJ, 742, 65

O'Neill, S. M., Reynolds, C. S., Miller, M. C., & Sorathia, K. A. 2011, ApJ, 736, 107

Osaki, Y. 1996, PASP, 108, 39

Paczyński, B. 1969, Acta Astron., 19, 1

Parker, E. N. 1955, ApJ, 122, 293

Pessah, M. E., Chan, C.-k., & Psaltis, D. 2007, ApJ, 668, L51

Pickering, E. C. 1896, Harvard College Observatory Circular, 12, 1

Pojmański, G. 1986, Acta Astron., 36, 69

Postnov, K. A., & Yungelson, L. R. 2014, Living Reviews in Relativity, 17

Potter, W. J., & Balbus, S. A. 2014, MNRAS, 441, 681

Rogachevskii, I., & Kleeorin, N. 2007, Phys. Rev. E, 75, 046305

Ruediger, G., & Kichatinov, L. L. 1993, A&A, 269, 581

Russell, T. D., et al. 2016, MNRAS, 460, 3720

Salvesen, G., Armitage, P. J., Simon, J. B., & Begelman, M. C. 2016a, MNRAS, 460, 3488

Salvesen, G., Simon, J. B., Armitage, P. J., & Begelman, M. C. 2016b, MNRAS, 457, 857

Sano, T., Inutsuka, S.-i., Turner, N. J., & Stone, J. M. 2004, ApJ, 605, 321

Sano, T., Miyama, S. M., Umebayashi, T., & Nakano, T. 2000, ApJ, 543, 486

Sano, T., & Stone, J. M. 2002, ApJ, 570, 314

—. 2003, ApJ, 586, 1297

Schreiber, M. R., & Gänsicke, B. T. 2002, A&A, 382, 124

Schreiber, M. R., Hameury, J.-M., & Lasota, J.-P. 2003, A&A, 410, 239

Schreiber, M. R., & Lasota, J.-P. 2007, A&A, 473, 897

Seaton, M. J. 2005, MNRAS, 362, L1

Semenov, D., Henning, T., Helling, C., Ilgner, M., & Sedlmayr, E. 2003, A&A, 410, 611

Shakura, N. I., & Sunyaev, R. A. 1973, A&A, 24, 337

—. 1976, MNRAS, 175, 613

Shi, J., Krolik, J. H., & Hirose, S. 2010, ApJ, 708, 1716

Shi, J.-M., Stone, J. M., & Huang, C. X. 2016, MNRAS, 456, 2273

Simon, J. B., Beckwith, K., & Armitage, P. J. 2012, MNRAS, 422, 2685

Simon, J. B., Hughes, A. M., Flaherty, K. M., Bai, X.-N., & Armitage, P. J. 2015, ApJ, 808, 180

Smak, J. 1984, Acta Astron., 34, 161

—. 1999, Acta Astron., 49, 391

—. 2009a, Acta Astron., 59, 89

—. 2009b, Acta Astron., 59, 121

Sorathia, K. A., Reynolds, C. S., & Armitage, P. J. 2010, ApJ, 712, 1241

Sorathia, K. A., Reynolds, C. S., Stone, J. M., & Beckwith, K. 2012, ApJ, 749, 189

Squire, J., & Bhattacharjee, A. 2015, Physical Review Letters, 115, 175003

Stone, J. M., Gardiner, T. A., Teuben, P., Hawley, J. F., & Simon, J. B. 2008, ApJS, 178, 137

Stone, J. M., & Norman, M. L. 1992a, ApJS, 80, 753

—. 1992b, ApJS, 80, 791

Suzuki, T. K., & Inutsuka, S.-i. 2009, ApJ, 691, L49

Suzuki, T. K., Muto, T., & Inutsuka, S.-i. 2010, ApJ, 718, 1289

Tomida, K., Tomisaka, K., Matsumoto, T., Hori, Y., Okuzumi, S., Machida, M. N., & Saigo, K. 2013, ApJ, 763, 6

Towns, J., et al. 2014, Computing in Science and Engineering, 16, 62

Turner, N. J. 2004, ApJ, 605, L45

Turner, N. J., & Sano, T. 2008, ApJ, 679, L131

Turner, N. J., & Stone, J. M. 2001, ApJS, 135, 95

Turner, N. J., Stone, J. M., Krolik, J. H., & Sano, T. 2003a, ApJ, 593, 992

—. 2003b, ApJ, 593, 992

van Paradijs, J. 1996, ApJ, 464, L139

Velikhov, E. P. 1959, Journal of Experimental and Theoretical Physics, 36, 995

Wardle, M. 2007, Ap&SS, 311, 35

Warner, B. 1995, Cambridge Astrophysics Series, 28

—. 2004, PASP, 116, 115

Warner, B., & Woudt, P. A. 2002, MNRAS, 335, 84

Woudt, P. A., & Warner, B. 2002, MNRAS, 333, 411

Appendix A

Equation of State

A.1 Introduction

Quite a few elements contribute significantly to the ionization and electron number density, so we include all the abundant elements: H, He, C, N, O, Ne, Na, Mg, Al, Si, P, S, Cl, Ar, K, Ca, Cr, Mn, Fe, and Ni. This is likely more than sufficient, but the code is reasonably fast, and given that we are just generating look-up tables, we may as well do it reasonably properly.

We consider three ionization states of atomic hydrogen: H^-, HI, and HII. The hydrogen anion may be an important sink of free electrons at low temperatures, thereby increasing the resistivity. On the other hand, it can also contribute to the conductivity if its number density is sufficiently large (greater than of order the square root of the ratio of the proton mass to the electron mass) compared to the free electron number density. Additionally, we consider two ionization states of molecular hydrogen: H_2, H_2^+.

It's not clear how important H_2^+ is; energetically its presence is negligible, however it may contribute a non-negligible amount of free electrons in certain regimes.

We also consider three ionization states of helium: HeI, HeII, and HeIII. The last is almost certainly irrelevant for DNe, but is certainly important for AM CVn. We include it even for DNe, as it is energetically the most important ionization transition at high temperatures and improves the agreement with the OPAL tables. For all the other species (i.e. all the "metals"), we consider just the neutral and singly ionized states.

A.2 Accounting

We define ν_i as the fixed fractional number abundance of element i,

$$\nu_i \equiv \frac{n_i}{n_{\rm nuc}} = \frac{10^{A_i-12}}{\sum_i 10^{A_i-12}}, \tag{A.1}$$

where $n_{\rm nuc}$ is the total number density of nuclei (H_2 counts as two nuclei), whether ionized or not, and A_i is the usual logarithmic number abundance of element i relative to hydrogen being set at $A_{\rm H} = 12$. While our code is capable of arbitrary abundances, it is currently hard coded to the solar composition from Anders & Grevesse (1989). The quantity $\mu_n = \sum_i \nu_i m_i$ is the fixed mean nuclear mass. Note that $n_{\rm nuc} = \rho/\mu_n$. The quantity $x_{i,r} \equiv n_{i,r}/n_i$ is the fractional $r^{\rm th}$ ionization of element i, i.e. the numerical fraction of all the nuclei of element i that are in the $r^{\rm th}$ ionization state. Additionally, we define $\nu_e = n_e/n_{\rm nuc}$ and $x_{e,r} = \delta_{r,-1}$, where δ is the Kronecker delta.

A.3 Partition functions

To determine all the $x_{i,r}$ we must first understand their relative partition functions. $Z_{i,r}$ is the partition function per volume for the r^{th} ionized state of species i (henceforth partition function will be used to mean partition function per volume). We also break partition functions into "internal" and "external" parts:

$$Z_{i,r} = Z_{i,r}^{\text{int}} \times Z_{i,r}^{\text{ext}}, \tag{A.2}$$

with these two parts subdivided as follows

$$Z_{i,r}^{\text{int}} = Z_{i,r}^{\text{bound}} \times Z_{i,r}^{\text{nuc}} \times Z_{i,r}^{\text{elec}}, \tag{A.3}$$

$$Z_{i,r}^{\text{ext}} = Z_{i,r}^{\text{tr}} \times Z_{i,r}^{\text{exct}}. \tag{A.4}$$

These parts are: internal bound states $Z_{i,r}^{\text{bound}}$, nuclear spin $Z_{i,r}^{\text{nuc}}$, electron spin and angular momentum $Z_{i,r}^{\text{elec}}$, translation $Z_{i,r}^{\text{tr}}$, and excitation $Z_{i,r}^{\text{exct}}$.

We now list the partition functions for all the species. The partition functions not explicitly described are unity. The translational partition function has the same form for all species

$$Z_{i,r}^{\text{tr}} = \left(\frac{2\pi m_i kT}{h^2}\right)^{3/2}, \tag{A.5}$$

and is the only "partition function" which is actually a partition function per volume. Note that we neglect differences in mass due to ionization level (i.e. $m_{i,r} = m_i$ for all r).

Molecular hydrogen ($r = 0, 1$ for H_2, H_2^+ respectively):

$$Z_{i,r}^{\text{bound}} = Z_{i,r}^{\text{rot}} \times Z_{i,r}^{\text{vib}} \tag{A.6}$$

$$Z_{\text{H}_2,r}^{\text{rot}} = Z_{\text{H}_2,r}^{\text{even}} + 3Z_{\text{H}_2,r}^{\text{odd}} \tag{A.7}$$

$$Z_{\text{H}_2,r}^{\text{even}} = \sum_{j=0,2,4,\ldots} (2j+1) \exp\left[-\frac{j(j+1)\theta_{\text{rot},r}}{2T}\right] \tag{A.8}$$

$$Z_{\text{H}_2,r}^{\text{odd}} = \sum_{j=1,3,5,\ldots} (2j+1) \exp\left[-\frac{j(j+1)\theta_{\text{rot},r}}{2T}\right], \tag{A.9}$$

$$Z_{\text{H}_2,r}^{\text{vib}} = \left[1 - \exp\left(-2\theta_{\text{vib},r}/T\right)\right]^{-1}, \tag{A.10}$$

$$Z_{\text{H}_2,0}^{\text{elec}} = 1, \tag{A.11}$$

$$Z_{\text{H}_2,1}^{\text{elec}} = 2, \tag{A.12}$$

$$Z_{\text{H}_2,1}^{\text{exct}} = \exp\left(-\frac{\chi_{\text{H}_2}}{kT}\right), \tag{A.13}$$

where $\theta_{\text{rot},0} = 170.64$ K, $\theta_{\text{vib},0} = 3169.5$ K, $\theta_{\text{rot},1} = 86.9$ K, $\theta_{\text{vib},1} = 1669.7$ K, and $\chi_{\text{H}_2} = 15.42593$ eV. We approximate the infinite sums by neglecting terms with $j > 200$. An important exclusion in this list is $Z_{\text{H}_2,r}^{\text{nuc}}$, as the even and odd rotational states already account for the protons being in spin-singlet and spin-triplet states, respectively. Also note that we utilize a rotational partition function for molecular hydrogen that lets the ratio of orthohydrogen to parahydrogen be determined by thermal equilibrium. A popular alternative is to set this ratio to 3:1, in which case

$$Z_{\text{H}_2,r}^{\text{rot}} = \left(Z_{\text{H}_2,r}^{\text{even}}\right)^{1/4} \left[3Z_{\text{H}_2,r}^{\text{odd}} \exp\left(\theta_{\text{vib},r}/T\right)\right]^{3/4}. \tag{A.14}$$

Atomic hydrogen ($r = -1, 0, 1$ for H^-, H, H^+ respectively):

$$Z_{\mathrm{H},0}^{\mathrm{bound}} = \sum_{n=1}^{n_{\mathrm{bound}}} n^2 \exp\left(-\frac{E_n}{kT}\right), \tag{A.15}$$

$$Z_{\mathrm{H},r}^{\mathrm{nuc}} = 2 \cdot \frac{1}{2} + 1 = 2, \tag{A.16}$$

$$Z_{\mathrm{H},0}^{\mathrm{elec}} = 2, \tag{A.17}$$

$$Z_{\mathrm{H},-1}^{\mathrm{exct}} = \exp\left(-\frac{\chi_{\mathrm{dis}} - 2\chi_{\mathrm{H},-1}}{2kT}\right), \tag{A.18}$$

$$Z_{\mathrm{H},0}^{\mathrm{exct}} = \exp\left(-\frac{\chi_{\mathrm{dis}}}{2kT}\right), \tag{A.19}$$

$$Z_{\mathrm{H},1}^{\mathrm{exct}} = \exp\left(-\frac{\chi_{\mathrm{dis}} + 2\chi_{\mathrm{H},0}}{2kT}\right), \tag{A.20}$$

where $E_n = \chi_{\mathrm{H},0}\,(1 - n^{-2})$, $\chi_{\mathrm{dis}} = 4.47718$ eV, $\chi_{\mathrm{H},-1} = 0.754195$ eV, and $\chi_{\mathrm{H},0} = 13.5984$ eV. In our code n_{bound} is approximated by $n_{\mathrm{bound}} = 10$. However, the value of n_{bound} seems to have little affect on the outcome of the code. Technically, the partition functions for every species should include all bound levels, but we did this only for hydrogen species. All other $Z_{i,r}^{\mathrm{bound}}$ are neglected (i.e. approximated as unity). Additionally, we find that H^- contributes a negative potential energy as it is more bound than HI.

Helium ($r = 0, 1, 2$ for He, He^+, He^{++} respectively):

$$Z_{\mathrm{He},1}^{\mathrm{exct}} = \exp\left(-\frac{\chi_{\mathrm{He},0}}{kT}\right), \tag{A.21}$$

$$Z_{\mathrm{He},1}^{\mathrm{elec}} = 2, \tag{A.22}$$

$$Z_{\mathrm{He},2}^{\mathrm{exct}} = \exp\left(-\frac{\chi_{\mathrm{He},0} + \chi_{\mathrm{He},1}}{kT}\right), \tag{A.23}$$

Metals (only ionization states $r = 0, 1$ are considered):

$$Z_{i,1}^{\text{exct}} = \exp\left(-\frac{\chi_{\text{i},0}}{kT}\right), \tag{A.24}$$

	C	N	O	Ne	Na	Mg	Al	Si	P	S	Cl	Ar	K	Ca	Cr	Mn	Fe	Ni
$Z_{i,r}^{\text{nuc}}$	1	2	1	1	4	1	6	1	2	1	4	1	4	1	1	6	1	1
$Z_{i,0}^{\text{elec}}$	9	4	9	1	2	1	6	9	4	9	6	1	2	1	7	6	25	21
$Z_{i,1}^{\text{elec}}$	6	9	4	6	1	2	1	6	9	4	9	6	1	2	6	7	30	10
$\chi_{i,0}$ (eV)	11.26	14.53	13.62	21.56	5.14	7.65	5.99	8.15	10.49	10.36	12.97	15.76	4.34	6.11	6.77	7.43	7.90	7.64

Here $Z_{i,r}^{\text{nuc}}$ is listed for the most abundant isotope of each species. However, the value of $Z_{i,r}^{\text{nuc}}$ is unimportant for metals (and helium) because $Z_{i,r}^{\text{nuc}}/Z_{i,r+1}^{\text{nuc}} = 1$ for all i, r, even if other isotopes are considered.

Electron:

$$Z_e = 2Z_e^{\text{tr}} \tag{A.25}$$

A.4 Saha Equation

We assume local thermal equilibrium (LTE) and thus utilize the Saha Equation to determine the values of $x_{i,r}$ as functions of T and n_e. By utilizing the definitions in Section A.2 we can write the Saha Equations for all ionization reactions as

$$x_{i,r} = x_{i,r+1}\frac{n_e Z_{i,r}}{Z_e Z_{i,r+1}} \tag{A.26}$$

Note that all of the partition functions are implicitly functions of T.

For each non-hydrogen species i with N_i ionization energies one can write $N_i - 1$ distinct Saha equations and

$$\sum_r x_{i,r} = 1, \tag{A.27}$$

which forms a closed set of equations, allowing us to solve for all $x_{i,r}$ which are listed here.

Helium:

$$x_{\mathrm{He},0} = \frac{n_e^2 Z_{\mathrm{He},0}}{n_e^2 Z_{\mathrm{He},0} + n_e Z_e Z_{\mathrm{He},1} + Z_e^2 Z_{\mathrm{He},2}} \tag{A.28}$$

$$x_{\mathrm{He},1} = \frac{n_e Z_e Z_{\mathrm{He},1}}{n_e^2 Z_{\mathrm{He},0} + n_e Z_e Z_{\mathrm{He},1} + Z_e^2 Z_{\mathrm{He},2}} \tag{A.29}$$

$$x_{\mathrm{He},2} = \frac{Z_e^2 Z_{\mathrm{He},2}}{n_e^2 Z_{\mathrm{He},0} + n_e Z_e Z_{\mathrm{He},1} + Z_e^2 Z_{\mathrm{He},2}} \tag{A.30}$$

Metals:

$$x_{i,0} = \left(1 + \frac{Z_e Z_{i,1}}{n_e Z_{i,0}}\right)^{-1} \tag{A.31}$$

$$x_{i,1} = \left(1 + \frac{n_e Z_{i,0}}{Z_e Z_{i,1}}\right)^{-1} \tag{A.32}$$

Hydrogen is the only species in which we must also include a molecular dissociation reaction. To determine the ionization fractions of hydrogen it is necessary to solve the following system of equations

$$1 = x_{\mathrm{H},-1} + x_{\mathrm{H},0} + x_{\mathrm{H},1} + 2x_{\mathrm{H}_2,0} + 2x_{\mathrm{H}_2,1}, \tag{A.33}$$

$$x_{\mathrm{H},-1} = x_{\mathrm{H},0} \frac{n_e Z_{\mathrm{H},-1}}{Z_e Z_{\mathrm{H},0}} \tag{A.34}$$

$$x_{\mathrm{H},0} = x_{\mathrm{H},1} \frac{n_e Z_{\mathrm{H},0}}{Z_e Z_{\mathrm{H},1}} \tag{A.35}$$

$$x_{\mathrm{H}_2,0} = \nu_{\mathrm{H}} x_{\mathrm{H},0}^2 \frac{n_{\mathrm{nuc}} Z_{\mathrm{H}_2,0}}{Z_{\mathrm{H},0}^2} \tag{A.36}$$

$$x_{\mathrm{H}_2,0} = x_{\mathrm{H}_2,1} \frac{n_e Z_{\mathrm{H}_2,0}}{Z_e Z_{\mathrm{H}_2,1}}. \tag{A.37}$$

Here Equation A.33 is number conservation of hydrogen and Equation A.36 is the Saha equation for the dissociation of H_2 into H.

A.5 Basic Thermodynamic Expressions

A.5.1 Pressure

Gas pressure is derived from the ideal gas law

$$P = nkT = \frac{\rho}{\mu}kT = n_{\rm nuc}kT\sum_{i,r}\nu_i x_{i,r} \tag{A.38}$$

where n is the number density of all particles

$$n = n_{\rm nuc}\sum_{i,r}\nu_i x_{i,r} = n_{\rm nuc}\left(1 - \nu_{\rm H}\sum_{r=0}^{1} x_{\rm H_2,r}\right) + n_e, \tag{A.39}$$

and μ is the mean molecular weight. Additionally, the gas pressure can be thought of as the sum of partial pressures:

$$P = \sum_{i,r} P_{i,r} = \sum_{i,r} n_{i,r}kT = \sum_{i,r} n_{\rm nuc}\nu_i x_{i,r}kT. \tag{A.40}$$

A.5.2 Internal Energy Density

The internal energy density (energy per volume) is given by

$$e = \sum_{i,r} e_{i,r} = \sum_{i,r} P_{i,r}\frac{\partial \ln Z_{i,r}}{\partial \ln T} = n_{\rm nuc}kT\sum_{i,r}\nu_i x_{i,r}\frac{\partial \ln Z_{i,r}}{\partial \ln T}. \tag{A.41}$$

For an ideal gas $\partial \ln Z_{i,r}/\partial \ln T$ is one half times the number of degrees of freedom.

One can add an arbitrary zero point energy to each $e_{i,r}$; we have effectively chosen the zero point of potential energy for each element to be that of the ground state of

the neutral atom, except for the case of hydrogen, in which the ground state of H_2 is used. This choice means that at both low and high temperatures, the internal energy density will be dominated by translational kinetic energy and that zero internal energy corresponds to a temperature of absolute zero.

A.5.3 Specific Entropy

The specific entropy for each species and ionization level is (Tomida et al., 2013)

$$s_{i,r} = \frac{k n_{i,r}}{\rho}\left(1 + \frac{\partial \ln Z_{i,r}}{\partial \ln T} - \frac{\mu_{i,r}}{kT}\right), \tag{A.42}$$

where the chemical potential $\mu_{i,r}$ is calculable as follows

$$\mu_{i,r} = kT \ln\left(\frac{n_{i,r}}{z_{i,r}}\right) = kT \ln\left(\frac{n_{\rm nuc}\nu_i x_{i,r}}{z_{i,r}}\right). \tag{A.43}$$

The total specific entropy is the sum of all the constituents

$$s = \sum_{i,r} s_{i,r}. \tag{A.44}$$

A.6 Charge Conservation

So far everything has been (either explicitly or implicitly) written in terms of three thermodynamic variables: density ($\rho = \mu_{\rm nuc} n_{\rm nuc}$), temperature ($T$), and electron abundance ($\nu_e = n_e/n_{\rm nuc}$). However, if we assert that our plasma must be neutral on macroscopic scales then we have an additional constraint:

$$\nu_q \equiv \sum_{i,r} r\nu_i x_{i,r} = \sum_{i\neq e,r} r\nu_i x_{i,r} - \nu_e = 0. \tag{A.45}$$

This constraint of charge conservation removes one degree of freedom. In other words if ρ and T are specified than ν_e is no longer a free parameter due to Eqn. A.45.

A.7 Choice of Independent Variables

As written so far, it would seem that this EOS must be a function of ρ and T, however that is not the case. Any arbitrary fluid parameters f and g can be used as independent variables so long as they cannot be expressed as functions solely of one another. In practice this is done by first specifying some values f_0 and g_0 and solving the following equations for ρ, T, ν_e[1]:

$$f(\rho, T, \nu_e) = f_0 \tag{A.46}$$

$$g(\rho, T, \nu_e) = g_0 \tag{A.47}$$

$$\nu_q(\rho, T, \nu_e) = 0, \tag{A.48}$$

where ν_q is given by Eqn. A.45. Except for the simplest cases, solving these equations can be tedious, even if one chooses $f = \rho$ and $g = T$. Thus, for most applications it is useful to generate a look up table ahead of time and interpolate on said table as needed.

[1]Using $\ln(\nu_e)$ as opposed to ν_e as an intrinsic variable often results in more numerically stable code.

A.8 Additional Thermodynamic Quantities

A.8.1 Miscellaneous Derivatives

For an arbitrary fluid parameter f the following derivatives are (relatively) easy to compute

$$\left(\frac{\partial f}{\partial \rho}\right)_T, \text{ and } \left(\frac{\partial f}{\partial T}\right)_\rho. \tag{A.49}$$

It is therefore useful to express derivatives in terms of the above expressions. Two examples for arbitrary fluid parameters f and g are given below:

$$\left(\frac{\partial f}{\partial \rho}\right)_g = \left(\frac{\partial f}{\partial \rho}\right)_T - \left(\frac{\partial f}{\partial T}\right)_\rho \left(\frac{\partial g}{\partial \rho}\right)_T \left(\frac{\partial T}{\partial g}\right)_\rho, \tag{A.50}$$

$$\left(\frac{\partial f}{\partial T}\right)_g = \left(\frac{\partial f}{\partial T}\right)_\rho - \left(\frac{\partial f}{\partial \rho}\right)_T \left(\frac{\partial g}{\partial T}\right)_\rho \left(\frac{\partial \rho}{\partial g}\right)_T. \tag{A.51}$$

A.8.2 Derivatives of ν_e

Many thermodynamic quantities depend on the abundance of free electrons $\nu_e \equiv n_e/n_{\text{nuc}}$, which is determined by charge conservation (see Eqn. A.45), and the number fractions $x_{i,r}$ in this equation implicitly depend on ν_e, making extracting derivatives of ν_e difficult. The differential of each $x_{i,r}$ can be expressed as follows:

$$\begin{aligned} \mathrm{d}\, x_{i,r} = \mathrm{d}\, T \left[\left(\frac{\partial x_{i,r}}{\partial T}\right)_{\rho,\nu_e} + \left(\frac{\partial x_{i,r}}{\partial \nu_e}\right)_{\rho,T} \left(\frac{\partial \nu_e}{\partial T}\right)_\rho\right] + \\ \mathrm{d}\, \rho \left[\left(\frac{\partial x_{i,r}}{\partial \rho}\right)_{T,\nu_e} + \left(\frac{\partial x_{i,r}}{\partial \nu_e}\right)_{\rho,T} \left(\frac{\partial \nu_e}{\partial \rho}\right)_T\right]. \end{aligned} \tag{A.52}$$

With this we can extract derivatives of ν_e from derivatives of ν_q. For example:

$$\left(\frac{\partial \nu_q}{\partial T}\right)_\rho = \sum_{i\neq e,r} r\nu_i \left(\frac{\partial x_{i,r}}{\partial T}\right)_\rho - \left(\frac{\partial \nu_e}{\partial T}\right)_\rho$$
$$= \sum_{i\neq e,r} r\nu_i \left(\frac{\partial x_{i,r}}{\partial T}\right)_{\rho,\nu_e} + \left(\frac{\partial \nu_e}{\partial T}\right)_\rho \left[-1 + \sum_{i\neq e,r} r\nu_i \left(\frac{\partial x_{i,r}}{\partial \nu_e}\right)_{\rho,T}\right] = 0, \quad \text{(A.53)}$$

resulting in

$$\left(\frac{\partial \nu_e}{\partial T}\right)_\rho = \sum_{i\neq e,r} r\nu_i \left(\frac{\partial x_{i,r}}{\partial T}\right)_{\rho,\nu_e} \left[-1 + \sum_{i\neq e,r} r\nu_i \left(\frac{\partial x_{i,r}}{\partial \nu_e}\right)_{\rho,T}\right]^{-1}. \quad \text{(A.54)}$$

Similarly $(\partial \nu_q/\partial \rho)_T = 0$ yields

$$\left(\frac{\partial \nu_e}{\partial \rho}\right)_T = \sum_{i\neq e,r} r\nu_i \left(\frac{\partial x_{i,r}}{\partial \rho}\right)_{T,\nu_e} \left[-1 + \sum_{i\neq e,r} r\nu_i \left(\frac{\partial x_{i,r}}{\partial \nu_e}\right)_{\rho,T}\right]^{-1}. \quad \text{(A.55)}$$

A.8.3 Adiabatic Sound Speed

First it is insightful to examine the first law of thermodynamics

$$\mathrm{d}\,\epsilon = -P\ \mathrm{d}\left(\frac{1}{\rho}\right) + T\ \mathrm{d}\,s = \frac{P}{\rho^2}\,\mathrm{d}\,\rho + T\,\mathrm{d}\,s, \quad \text{(A.56)}$$

where $\epsilon = e/\rho$ is the specific internal energy, and s is the specific entropy. By differentiating this with respect to P at constant s we get:

$$\left(\frac{\partial \epsilon}{\partial P}\right)_s = \frac{P}{\rho^2}\left(\frac{\partial \rho}{\partial P}\right)_s = \frac{P}{a^2\rho^2}, \quad \text{(A.57)}$$

where a is the adiabatic sound speed. Expanding the left side of this equation gives

$$\left(\frac{\partial \epsilon}{\partial P}\right)_s = \left(\frac{\partial \epsilon}{\partial P}\right)_\rho + \left(\frac{\partial \epsilon}{\partial \rho}\right)_P \left(\frac{\partial \rho}{\partial P}\right)_s = \left(\frac{\partial \epsilon}{\partial P}\right)_\rho + \left(\frac{\partial \epsilon}{\partial \rho}\right)_P a^{-2} = \frac{P}{a^2\rho^2}. \quad \text{(A.58)}$$

Solving for a^2 gives

$$a^2 = \left(\frac{\partial P}{\partial \epsilon}\right)_\rho \left[\frac{P}{\rho^2} - \left(\frac{\partial \epsilon}{\partial \rho}\right)_P\right]. \tag{A.59}$$

$\left(\frac{\partial \epsilon}{\partial \rho}\right)_P$ has the form of Eqn. A.50, with $f = \epsilon$, $g = P$, and

$$\left(\frac{\partial P}{\partial \epsilon}\right)_\rho = -\left(\frac{\partial P}{\partial \rho}\right)_\epsilon \Big/ \left(\frac{\partial \epsilon}{\partial \rho}\right)_P, \tag{A.60}$$

where $\left(\frac{\partial P}{\partial \rho}\right)_\epsilon$ also has the form of Eqn. A.50, with $f = P$, and $g = \epsilon$. Thus Eqn. A.59 reduces to

$$a^2 = \left(\frac{\partial P}{\partial \rho}\right)_T + \left[\frac{P}{\rho^2} - \left(\frac{\partial \epsilon}{\partial \rho}\right)_T\right] \left(\frac{\partial P}{\partial T}\right)_\rho \Big/ \left(\frac{\partial \epsilon}{\partial T}\right)_\rho \tag{A.61}$$

$$= \left(\frac{\partial P}{\partial \rho}\right)_T + \left[\frac{P+e}{\rho} - \left(\frac{\partial e}{\partial \rho}\right)_T\right] \left(\frac{\partial P}{\partial T}\right)_\rho \Big/ \left(\frac{\partial e}{\partial T}\right)_\rho \tag{A.62}$$

A.8.4 Adiabatic Indices

An ideal gas can be described by a single adiabatic index γ. However, for a general gas three separate adiabatic indicies are needed which all take the same value when the gas is ideal. The first is:

$$\Gamma_1 = \left(\frac{\partial \ln P}{\partial \ln \rho}\right)_s = \frac{\rho}{P}\left(\frac{\partial P}{\partial \rho}\right)_s = \frac{\rho}{P}a^2$$

$$\Gamma_3 - 1 = \left(\frac{\partial \ln T}{\partial \ln \rho}\right)_s = \frac{\rho}{T}\left(\frac{\partial \epsilon}{\partial \rho}\right)_s \left(\frac{\partial T}{\partial \epsilon}\right)_\rho + \frac{\rho}{T}\left(\frac{\partial T}{\partial \rho}\right)_\epsilon$$
$$= \frac{P}{T}\left(\frac{\partial T}{\partial e}\right)_\rho - \frac{\rho}{T}\left(\frac{\partial e}{\partial \rho}\right)_T \Bigg/ \left(\frac{\partial e}{\partial T}\right)_\rho \tag{A.63}$$

$$\nabla_{\rm ad} \equiv \frac{\Gamma_2 - 1}{\Gamma_2} = \left(\frac{\partial \ln T}{\partial \ln P}\right)_s = \frac{\Gamma_3 - 1}{\Gamma_1} \tag{A.64}$$

A.9 Resistivity

The conductivity of a charged species (electrons and ions) i can be determined by equating the frictional/collisional forces with the forces exerted by the external electric field.

$$F_{{\rm fric},i} = \sum_{{\rm neutrals},n} \mu_{i,n} n_n n_i \left\langle \sigma_{\rm scat} v \right\rangle_{n,i} (v_i - v_n) \tag{A.65}$$

$$F_{{\rm elec},i} = n_i q_i E \tag{A.66}$$

where $\mu_{i,n} = \dfrac{m_n m_i}{m_n + m_i}$ is the reduced mass of the charged species i and the neutral n, $\sigma_{\rm scat}$ is the scattering cross section, and q_i is the charge of species i. Additionally, the current density of species i in the fluid rest frame is

$$J_i = n_i q_i v_i = \sigma_i q_i E. \tag{A.67}$$

Making the approximation that $v_n = v_{\rm fluid} = 0$ for all n we get

$$\sigma_i = n_i \frac{v_i}{E} = \frac{n_i q_i^2}{\sum_n \mu_{i,n} n_n \left\langle \sigma_{\rm scat} v \right\rangle_{i,n}} \tag{A.68}$$

Resistivity is then

$$\eta = \frac{c^2}{4\pi \sum_i \sigma_i}. \tag{A.69}$$

Here are the $\langle \sigma_{\rm scat} v \rangle_{n,i}$ used

$$\langle \sigma_{\rm scat} v \rangle_{{\rm e}^-,n} = 8.3 \times 10^{-10} T^{1/2} \text{ cm}^3 \text{ s}^{-1} \qquad \text{(Blaes \& Balbus, 1994b)} \tag{A.70}$$

$$\langle \sigma_{\rm scat} v \rangle_{i \neq {\rm e}^-,n} = 1.9 \times 10^{-9} \text{ cm}^3 \text{ s}^{-1} \qquad \text{(Draine et al., 1983b)} \tag{A.71}$$

As of now only contribution from the charged species e^-, H^-, H_2^+ (electrons dominate as long as $n_{\rm H^-}/n_{e^-} \ll m_p/m_e\sqrt{5.3/T} = \sqrt{2.1 \times 10^7/T}$) and only collisions with the neutrals H, H_2, and He are considered. This method gets virtually the same numerical results as Blaes & Balbus (1994b), which signifies that electrons are the main current carrier.

Appendix B

Abbreviations Used

AAVSO:	American Association of Variable Star Observers
AGN:	active galactic nucleus/nuclei
ALMA:	Atacama Large Millimeter/submillimeter Array
AM CVn(s):	AM Canum Venaticorum type star(s)
CV(s):	cataclysmic variable(s)
DIM:	disk instability model
DN(e):	dwarf nova(e)
DNO(s):	dwarf nova oscillation(s)
EOS:	equation of state
HST:	Hubble Space Telescope
LTE:	local thermal equilibrium
MHD:	magnetohydrodynamics
MRI:	magnetorotational instability
QPO(s):	quasi-periodic oscillation(s)
XSEDE:	Extreme Science and Engineering Discovery Environment